Plasmon-Exciton Coupling Dynamics in Metal-ZnO Nanostructures

BY

Benjamin J. Lawrie

Dissertation

Submitted to the Faculty of the

Graduate School of Vanderbilt University

in partial fulfillment of the requirements

for the degree of

DOCTOR OF PHILOSOPHY

in

Interdisciplinary Materials Science

August, 2011

Nashville, TN

Approved:

Professor Richard F. Haglund Jr.

Professor Richard Mu

Professor David E. Cliffel

Professor Kalman Varga

Professor M. Shane Hutson

To my wife Jenifer, and my son Isaac.

Acknowledgements

This dissertation would not have happened without the support of my Master of Science advisor, Professor Richard Mu, who allowed me the freedom to find the right project while asking the right questions and providing the necessary guidance to provide a smooth transition into my Ph.D. research under the guidance of Professor Richard Haglund. Beginning during my MS work at Fisk, and continuing throughout my time at Vanderbilt, Professor Haglund's support and questions pushed me towards a deeper understanding of my research. I thank both professors for teaching me the experimental, analytical, and presentation skills I have acquired over the past five years.

I am also very grateful to Professors Cliffel, Hutson, and Varga for serving on my Ph.D. Committee and for their guidance and expertise throughout my time here. Their questioning during each Committee meeting was vital to the development of my research.

In addition, I owe significant thanks to the members of Professor Mu and Professor Haglund's groups for their guidance and expertise. In particular, the instruction and training offered by Professors Roberto Aga, Akira Ueda, and Zhenga Pan was essential during my time at Fisk, and Professor Sergey Avanesyan provided many helpful discussions and advice regarding our optical experiments at Vanderbilt. I thank my group members, particularly Andrej Halabica, Jed Ziegler, Joyeeta Nag, Charlie Adams, and Krishen Appavoo for helpful discussions and assistance with the many experimental and computational techniques used throughout my research.

Ying Xu and Drew Steigerwald provided significant assistance with the Titan regenerative amplifier and system alignment during my first pump-probe experiments. More significantly, my ultrafast experiments would have gone nowhere without John Kozub. Without his patience and instruction in the maintenance and alignment of the Titan and TOPAS optical parametric amplifier, my ultrafast experiments would not have gotten off the ground.

Chapter 5 relies on the quantum wells I fabricated as part of my internship at the University of Florida. The instruction in laser molecular-beam epitaxy and epitaxial film growth offered by Kyeong-Won Kim and his advisor Professor David Norton was a vital

part of my graduate education. The time they spent training me in the use of the pulsed laser deposition chamber and the time during which I was allowed to use their facilities are greatly appreciated.

Significant portions of my research were conducted in the Vanderbilt Institute for Nanoscale Science and Engineering facilities, and as a result I owe significant thanks to all of the VINSE staff, particularly Prof. Anthony Hmelo, Dr. Bo Choi, Dr. Ben Schmidt, and Dr. Bob Geil. The technical expertise and research advice they offered was helpful throughout my time at Vanderbilt.

Finally, I never would have made it this far without the support of my family. Whenever I have come home from a bad day in the lab, Jen has been there to cheer me up, or to commiserate. On the days when I needed to stay late in the lab, she has happily taken care of Isaac. Isaac has been an amazing distraction: he is constantly getting into trouble, but his happiness is infectious, and he is always able to distract me from whatever problems I may be facing in the lab.

This dissertation is a result of work funded by an NSF IGERT grant (NSF-DMR-0333302), by an NSF-CREST grant: (HRD-0420516), and by the US Department of Energy, Office of Science Grant (DE-FG02-01ER45916). A significant portion of the work was performed in the Vanderbilt Institute of Nanoscale Science and Engineering, using facilities renovated under NSF ARI-R2 DMR-0963361.

Table of Contents

List of Figures

List of Tables

Preface

At surfaces, interactions between metal nanostructures and light can generate collective excitations in the form of localized surface plasmons (LSPs) or propagating surface plasmon polaritons (SPPs) that interact with quantum systems such as excitons and donor-acceptor pair (DAP) complexes in an adjacent semiconductor. The interactions of plasmons with excitons and other light-emitting complexes can enhance or reduce quantum efficiency, facilitate electromagnetically induced transparency, and elicit Fano-like resonance response, transient optical magnetism and disorder-induced light localization. Indeed, plasmonic elements are now being used to dramatically enhance photon absorption in fourth generation thin film solar cells,[1, 2] and semiconductor-metal heterostructures are being used to generate surface plasmon amplification by stimulated emission of radiation (SPASERs).[3, 4] Understanding this class of photon interactions with interfaces and thin films is thus significant for both the science and technology of the interactions of light with condensed phases.

Zinc oxide films or quantum wells and plasmonic elements, comprising rough metal films and nano-cylinder arrays of Ag, Al or Au, constitute an especially interesting model system for studying plasmon-exciton interactions. ZnO has a wide bandgap, a large exciton binding energy, and optical transitions that extend from the near infrared to the UV and thus overlap surface plasmon resonance energies in Ag, Al and Au. Hence, heterostructures incorporating ZnO films or quantum wells and plasmonic elements constitute a unique workbench for probing and manipulating the interactions of surface plasmons and surface-plasmon polaritons with quantum states.

This dissertation focuses on the energetics, dynamics and control of the coupling between band-edge excitons and luminescent defect complexes in ZnO thin films and quantum wells, on the one hand, and localized or propagating plasmons in metallic films and nanostructures on the other. These general considerations and the experimental methods used to prepare and analyze the model heterostructures are described in Chapters 1 and 2.

Chapter 3 discusses photoluminescence spectroscopy on multilayer structures of ZnO, MgO, and Ag or Au with varying thicknesses of MgO as a template for analyzing interactions as a function of plasmon-emitter separation. In particular, the coupling of Ag and Au SPPs to excitons via Purcell-like interactions, and the dipole-dipole scattering of Ag and Au LSPs with ZnO DAPs is discussed. Further, the effect of SPP coupling into Si substrates is presented through comparison of heterostructures on Si and Al_2O_3.

Chapter 4 provides additional context for these interactions through examination of the Purcell enhancement calculated from bi-exponential fits to the transient reflection spectra of the Ag-MgO-ZnO heterostructures. Simultaneous transmission and reflection pump-probe spectroscopies on samples annealed under varying conditions demonstrate a long-lived Zn interstitial state that demonstrates a narrow photoluminescence emission in the presence of Ag SPPs.

Finally, Chapter 5 presents the results of extinction and photoluminescence experiments based on aluminum nanodisc arrays fabricated on $ZnO/Zn_{0.85}Mg_{0.15}O$ single quantum wells. The emergence of a Fano resonance in the Al nanodisc extinction spectra indicates the *coherent* LSP-exciton coupling characteristic of the strong-coupling regime.

While there are a significant number of papers that discuss plasmon-exciton coupling in semiconductor-metal heterostructures, and a growing number of papers that examine plasmon-exciton coupling in ZnO-metal heterostructures, the variable MgO spacer layers introduced in Chapter 3 allowed for a full analysis of the coupling energetics and dynamics as a function of exciton-plasmon separation. Because of this approach, we were able to clearly characterize the coupling energetics and dynamics of the various interactions seen in metal-ZnO heterostructures that had previously been unclearly classified or unreported in the literature: enhancement related to charge transfer processes, Purcell enhancement, and dipole-dipole scattering. Aside from the 'green PL,' ZnO defect-states have been largely ignored in the literature, and studies of the defect-state dynamics are also sorely lacking. The distinction between the differential transmission and reflection pump-probe spectra discussed in Chapter 4 provided a convenient technique for analyzing near-surface defect-states while also recording the dramatic control of the defect-state dynamics by Ag surface plasmon polaritons. Finally, the transition into the strong coupling regime allowed by the nanodesigned heterostructures discussed in Chapter 5 presents the first observation of strong coupling in ZnO-metal heterostructures. Because of the myriad nonlinear optical applications offered by strongly coupled systems, including electromagnetically induced transparency and hybridized plasmon-exciton states, the demonstration of strong coupling in the near-UV is of significant interest for practical applications in technology as well as for basic science.

CHAPTER 1: INTRODUCTION

This chapter introduces the interactions between photoluminescent centers in zinc oxide (ZnO) and plasmons supported on metal nanostructures and nanostructured films. The optical properties of ZnO films and quantum wells are presented, as is an introduction to local surface plasmons (LSPs) and surface plasmon polaritons (SPPs). The literature on plasmon-exciton coupling energetics and dynamics are also reviewed for both the weak-coupling and strong-coupling regimes. #

1.1 Bulk and thin film optical properties of ZnO

The wide bandgap of 3.37 eV and large exciton binding energy of 60 meV of ZnO have attracted enormous interest for potential applications in electronic and UV opto-electronic devices,[5, 6] including nanolasers[7, 8] due in large part to the relatively low binding energy of 25 meV seen in typical UV semiconductors like GaN. As with all wide-bandgap n-type semiconductors, it is difficult to achieve stable p-type semiconductivity[9], but initial reports of p-type ZnO have generated a flurry of interest in ZnO optoelectronic properties and applications.[6, 10] With a significantly higher threshold for radiation damage than common semiconductors like GaAs, GaN, and Si, ZnO is also an exciting material for space applications.[11] ZnO crystallizes in a hexagonal wurtzite structure with lattice constants of a = 3.25 Å and c = 5.21 Å, though it has been shown to grow in a metastable zincblende and rocksalt structures under high growth pressures. At pressures of 9 - 15 GPa, wurtzite ZnO undergoes a structural phase transition to rocksalt ZnO, and it reverts to the single-phase wurtzite structure at 1.9 GPa.[12]

Despite being tetrahedrally coordinated, wurtzite ZnO is not a completely sp^3 hybridized material; it is characterized by roughly 50% ionic bonding and 50% sp^3 covalent bonding. The conduction band has a spherical symmetry associated with s-like states, and the valence band is composed of p-like states that split into three bands as a result of spin-orbit and crystal field coupling. The resulting three excitons are typically labeled A (with a transition at 3.37eV), B (with a transition at 3.38eV), and C (with a transition at 3.425eV) at 4K. For excitations with $\mathbf{E} \perp \mathbf{c}$ and $\mathbf{k} \perp \mathbf{c}$, all three excitons are allowed but A and B dominate C. For excitations with $\mathbf{E} \parallel \mathbf{c}$ and $\mathbf{k} \perp \mathbf{c}$, C is strongly allowed, while A is forbidden and B is weakly present. In the case of $\mathbf{E} \perp \mathbf{c}$ and $\mathbf{k} \parallel \mathbf{c}$ all three excitons exist in similar amplitudes.[5]

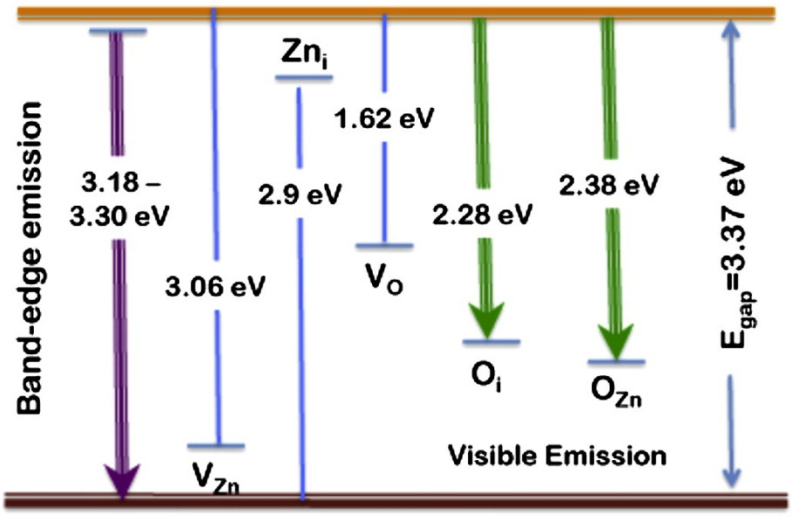

Figure 1: Illustration of impurity states in ZnO thin film photoluminescence (adapted from [13]).

The room temperature UV PL of ZnO thin films is generally reported to lie between 3.18 and 3.31 eV.[5, 6, 13] The red-shifted emission is a result of excitons bound to shallow unintentional impurities and donor-like defects or to donor-acceptor pair (DAP)

recombination of shallow donor and shallow acceptor sites, but at this time, the origin of these sites is not well understood.[5, 14] The well known green-band PL centered between 2.3 and 2.5 eV generally dominates the visible DAP emission, but there is still some controversy about the origin of the green PL. Full-potential linear muffin-tin orbital method calculations, in concert with annealing studies, suggest that the green PL is the superposition of peaks due to the recombination of deep holes located on zinc anti-site defects and oxygen interstitials with near conduction-band electrons.[13] However, compelling arguments based on electron paramagnetic resonance (g=1.96) have been presented by Van Heusden *et al.* suggesting that the visible emission is due to the recombination of electrons in singly occupied oxygen vacancies with valence band-edge holes.[15] Alternatively, Bylander *et al.* have posited that the visible emission is due to a transition from interstitial Zn to a Zn vacancy.[16] For the purposes of this work, the impurity energetics presented by Lin *et al.*—presented in graphical format in Figure 1—are used to describe the deep defect sites in ZnO.[13] The Zn interstitial at 2.9 eV and the O and Zn vacancies at 1.62 eV and 3.06 eV respectively described in Figure 1 are not seen in ZnO under normal preparation conditions, and have not been described extensively in the literature.

1.1.1 ZnO recombination dynamics

There is still relatively little literature studying exciton[17, 18] and DAP[19] dynamics in ZnO thin films, though the dynamics of single crystal ZnO are better understood.[20, 21] Despite the recent interest on the energetics of metal-ZnO heterostructures, there have been no reports studying the dynamics of these systems. ZnO exciton dynamics can be understood through the application of time-resolved photoluminescence (TRPL) and

pump-probe spectroscopy. Both are non-destructive techniques which prove phenomenally useful in the pursuit of understanding of recombination dynamics, though traditional TRPL techniques are limited by electronic gate timing, and no literature describing ZnO dynamics with optically gated TRPL techniques currently exists.

TRPL measurements on bulk single crystal samples — either as grown, or annealed in forming gas — demonstrate a bi-exponential decay consisting of an irresolvable thermal decay followed by decay constants of 0.17nm and 0.86 ns, and 0.36nm and 2.47ns respectively.[21] The fast decay constant is ascribed to non-radiative recombination, while the slow decay is attributed to the free-exciton radiative life-time. The increase in radiative lifetime after annealing is matched by an increase in the peak PL intensity by a factor four.

Epitaxial and polycrystalline ZnO thin films demonstrate shorter lifetimes because of the higher defect densities compared with bulk ZnO. ZnO epitaxial films grown by laser molecular beam epitaxy (laser MBE) on $ScAlMgO_4$ demonstrated a single exponential decay with a decay time which increased from 46 ps to 110 ps as the growth temperature increased from 570 to 800° C. Presumably, the single exponential decay suggests that the recombination dynamics are dominated by non-radiative processes, though the fit must account for both radiative and non-radiative effects. However, a homoepitaxial film with fewer point defects than any other film examined demonstrated the shortest decay time of 36 ps, suggesting no correlation between PL decay time and point defect density, but rather that the recombination dynamics are governed by Zn vacancy complexes.[20]

Degenerate band-edge pump-probe spectroscopy performed on polycrystalline ZnO thin films for pump energies greater than the free-exciton emission peak resulted in a double-exponential decay which can be understood in terms of thermalization followed by recombination. Thermalization occurred within less than 2 ps, at which point a quasi-equilibrium exciton state was formed, which decayed with a lifetime ranging from several picoseconds to several tens of picoseconds, depending on temperature. Below 90 K, the exciton relaxation exhibited a decay time of 75-85 ps, compared with lifetimes of less than 10 ps above 90 K. This can be explained by exciton trapping at neutral donor sites at low temperatures, in contrast with free-exciton recombination at higher temperatures.[17] The idea of a picosecond thermalization process followed by a exciton recombination process tens of picoseconds in duration is corroborated by other authors.[18, 19] There is extremely limited literature examining the impurity recombination dynamics, but a two-color pump-probe experiment — with probe wavelength of between 575 nm and 825 nm — has demonstrated an impurity state lifetime of roughly 400 ps. [19] Unfortunately, there is *no* literature at all that categorizes the lifetimes of the different visible impurity states, and it is not clear from Bauer's paper which impurity states were present in their film.

1.2 [Zn,Mg]O Quantum Wells

ZnO quantum wells (QWs) are generally fabricated either as [Zn,Mg]O heterostructures[22-27] or as [Zn,Cd]O heterostructures[28-32]. The electronic and crystalline structure of ternary semiconductors like $Zn_{1-x}A_xO$(where A=Mg or Cd) can be described by Vegard's law, which states that while a linear relationship exists between the lattice constant and the concentrations of the constituent elements, the bandgap varies

nonlinearly.[33, 34] To first approximation, the bandgap of $Zn_{1-x}A_xO$ (where A=Mg or Cd) can be described by $E_g(x) = (1-x) * E_{ZnO} + x * E_{AO} - b * x * (1-x)$, where b is the optical bowing parameter that indicates the extent of nonlinearity. The nonlinearity generally originates from three sources: 1) the volume deformation due to the changed lattice constants, 2) the electronegativity difference of the substitutional atoms, and 3) the structural relaxation of the anion-cation bond lengths and angles to accommodate the different atom sizes.[35]

Alloying ZnO with Cd results in a reduced bandgap, so that ZnO/ $Zn_{1-x}Cd_xO$ quantum wells utilize ZnO as the barrier layer and $Zn_{1-x}Cd_xO$ as the well. The interest in this dissertation lies with [Zn,Mg]O QWs, where $Zn_{1-x}Mg_xO$ has a wider bandgap than ZnO and serves as the barrier layer.

While the large MgO bandgap of 7.8 eV suggests that $Zn_{1-x}Mg_xO$ should be a convenient barrier material, there remain several issues. First, while ZnO has a wurtzite structure with lattice constants a = 3.25 Å and c = 5.21 Å, MgO has a cubic structure with a = 4.24 Å. Second, according to the ZnO/MgO phase diagram, the thermodynamic solid solubility of MgO in ZnO is only 4%.[5] Experimental results studying the growth of $Zn_{1-x}Mg_xO$ thin films have demonstrated that cubic MgO grains self-segregate in the wurtzite $Zn_{1-x}Mg_xO$ structure for $x>0.33$, thus limiting the barrier bandgap to 3.9 eV.[36] Measurements of the bandgap as a function of x demonstrate a linear relationship which indicates, at least in the regime $x<0.33$, the bowing parameter *b* vanishes.

The excitonic emission of [Zn, Mg]O quantum wells is controlled by both quantum confinement and the quantum confined stark effect (QCSE). Quantum

confinement results in the excitonic emission blue-shifting by as much as 300 meV from the bulk ZnO emission in wells with widths less than twice the exciton Bohr radius and with barriers of Mg content less than 20%.[25, 37] Quantum wells in which quantum confinement is the dominant effect demonstrate an increased exciton binding energy, and a correspondingly increased radiative efficiency.[38]

The electric fields within [Zn,Mg]O quantum wells have been shown to vary from 0.3 to 0.9 MV/cm with increasing Mg content as a result of both the piezoelectric field caused by the ZnO-$Zn_{1-x}Mg_xO$ lattice mismatch and the spontaneous polarization caused by crystal inversion asymmetry. The QCSE caused by these fields results in a red-shift of the excitonic emission by as much as 400 meV from that observed in bulk ZnO, but the strong field also causes the separation of the electron and hole wave functions, leading to a reduction in the exciton binding energy, optical gain, and radiative efficiency.[39, 40] The piezoelectric and spontaneous polarizations are in opposite directions in [Zn,Mg]O quantum wells — $P_{PE} = -34x$ mC/m^2 and $P_{SP} = 66x$ mC/m^2 — which results in negligibly small electric fields in wells with $x<0.2$ and well width less than 5 nm.[39, 41] Neither [Ga,Al]N nor [Ga,In]N quantum wells demonstrate this equilibrium, and as a result, appropriately designed [Zn,Mg]O quantum wells have been shown to have much larger gain than [Ga,Al]N or [Ga,In]N quantum wells.[39, 41]

1.2.1 ZnO QW dynamics

Time-resolved photoluminescence (TRPL) measurements on [Zn,Mg]O quantum wells have shown quantum confined lifetimes as short as 360 ps in wells with x=0.1,[42]

and as long as several ms in wells with x=0.22.[43] In principle, it should be possible to design ZnO quantum wells with lifetimes of less than 10 ps. The excitonic emission from $Zn_{0.9}Mg_{0.1}O$ has been shown to have a lifetime of roughly 470 ps at 77 K.[42] Figure 2 demonstrates the relationship between peak energy, quantum well exciton lifetime, and well width for wells with x=0.22.[25] The high Mg content in the barriers results in an internal electric field of 0.8MV/cm, yielding strong QCSE phenomena.

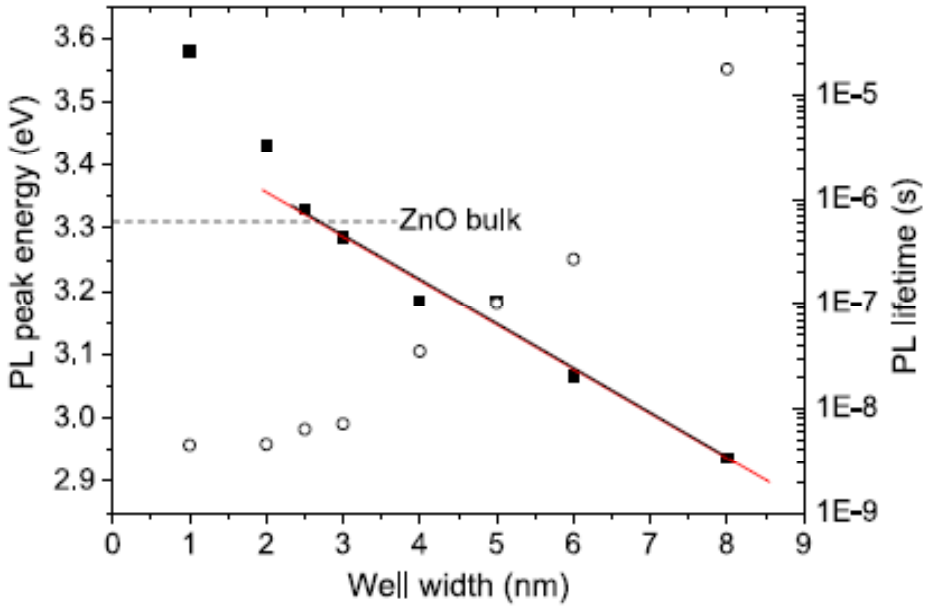

Figure 2: *Peak energy from exciton emission (closed squares) and exciton lifetime (open squares) as a function of well width for [Zn,Mg]O multiple quantum wells with x=0.22.[25] The red line confirms the linear relationship between well width and peak energy for QWs governed by the quantum confined Stark effect.*

Spectrally resolved two-color (3.35 eV and 3.45 eV) four-wave mixing measurements performed on a 3 nm $ZnO/Zn_{0.7}Mg_{0.3}O$ QW with a high fluence 10 mJ/cm^2 excitation have demonstrated two-photon coherence with a 100 fs decoherence time, which strongly suggests the formation of bi-excitons.[44] Bi-exciton transitions have been shown to allow for lower threshold lasing in II-VI QWs,[45] providing motivation for continued research into bi-exciton transitions in [Zn, Mg]O QWs for UV laser applications.

1.3 Plasmons

This section presents a brief introduction to SPPs and LSPs. The derivations are based on the presentation in Maier's *Plasmonics: Fundamentals and Applications*.[46] Plasmons are the fundamental excitation of the electron sea in bulk and nanostructured metals. The plasmon resonance can be understood from a simple application of the equations of motion to a free electron. The equation of motion for a free electron in an external field $\boldsymbol{E}$ is $m\ddot{\boldsymbol{x}} + m\gamma\dot{\boldsymbol{x}} = -e\boldsymbol{E}$, where the collision frequency γ is related to the resistivity of the metal, and is a result of electron-electron, electron-phonon, and electron-defect collisions. If $\boldsymbol{E}$ is assumed to have harmonic time dependence, the position of the electron can be described by $\boldsymbol{x}(t) = \frac{e\boldsymbol{E}(t)}{m(\omega^2 + i\gamma\gamma\omega}$, and given the macroscopic polarization $\boldsymbol{P} = -n * e * \boldsymbol{x}$ and the definition of the electric displacement for linear, isotropic media: $\boldsymbol{D} = \varepsilon_0 \boldsymbol{E} + \boldsymbol{P} = \varepsilon_0 \varepsilon \boldsymbol{E}$, it is straightforward to write:

$$\varepsilon(\omega) = 1 - \frac{\omega_p^2}{\omega^2 + i\gamma\omega}, \tag{1.1}$$

where ω_p is the bulk plasmon frequency:

$$\omega_p = \sqrt{ne^2 / m\varepsilon_0}. \tag{1.2}$$

1.3.1 Surface plasmon polaritons

SPPs are coupled plasmon-photon modes that produce electromagnetic waves propagating along the interface between metal and dielectric films, evanescently confined normal to the interface. Treating the SPP as the one-dimensional problem seen in Figure 3 with waves propagating along the x-axis, and defining the interface between the metal and dielectric films as z=0, the Helmholtz equation for the fields can be written as:

$$\frac{d^2\mathbf{E}(z)}{dz^2}+\left(\left(\frac{\omega}{c}\right)^2\varepsilon-k_x^2\right)\mathbf{E}=0;\quad \frac{d^2\mathbf{H}(z)}{dz^2}+\left(\left(\frac{\omega}{c}\right)^2\varepsilon-k_x^2\right)\mathbf{H}=0 \quad . \tag{1.3}$$

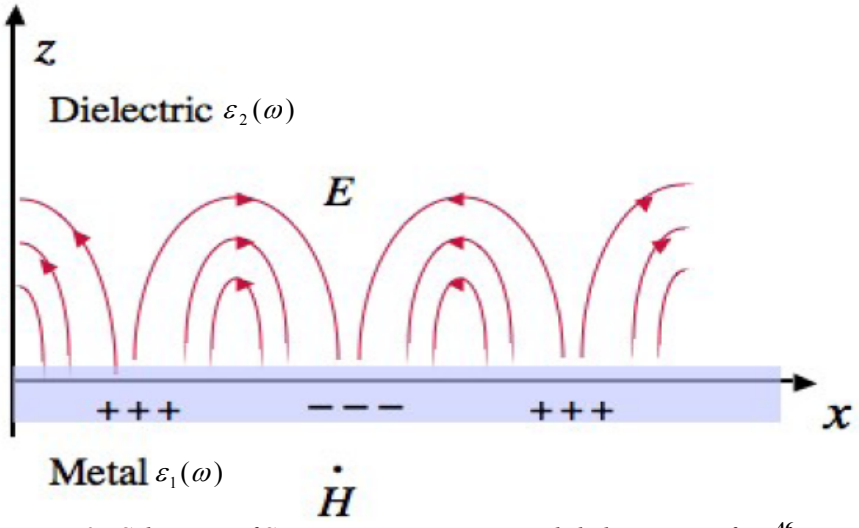

Figure 3: Schematic of SPP propagation in a metal-dielectric interface.[46]

Assuming harmonic time dependence, propagation along the *x*-axis, and homogeneity along the *y*-axis, Maxwell's curl equations reduce to TM modes described by:

$$E_x=\frac{-i}{\omega\varepsilon\varepsilon_0}\frac{dH_y}{dz};\quad E_z=\frac{-k_x}{\omega\varepsilon\varepsilon_0}H_y \quad , \tag{1.4a,b}$$

and TE modes described by:

$$H_x=\frac{i}{\omega\mu_0}\frac{dE_y}{dz};\quad H_z=\frac{k_x}{\omega\mu_0}H_y \quad . \tag{1.5a,b}$$

Solving (1.3) and (1.4) , and requiring the continuity of H_y and $\varepsilon_i E_z$ yields:

$$\frac{k_2}{k_1}=-\frac{\varepsilon_2}{\varepsilon_1};\ k_1^2=k_x^2-\varepsilon_1\left(\frac{\omega}{c}\right)^2;\quad k_2^2=k_x^2-\varepsilon_2\left(\frac{\omega}{c}\right)^2 \quad , \tag{1.6a,b,c}$$

where k_i is the wave-vector component normal to the dielectric-metal interface whose inverse defines the evanescent decay length. Solving (1.6) yields the SPP dispersion relationships:

$$k_x = \frac{\omega}{c}\sqrt{\frac{\varepsilon_1\varepsilon_2}{\varepsilon_1+\varepsilon_2}};\ k_1 = \frac{\omega}{c}\sqrt{\frac{\varepsilon_1^2}{\varepsilon_1+\varepsilon_2}};\ k_2 = \frac{\omega}{c}\sqrt{\frac{\varepsilon_2^2}{\varepsilon_1+\varepsilon_2}}\ . \qquad (1.7a,b,c)$$

Repeating this process for the TE modes yields the condition $(k_1+k_2)=0$. In order for the SPP to be confined to the surface, $\mathrm{Re}[k_1]$ and $\mathrm{Re}[k_2]$ must both be positive, so it is clear that TE polarized surface modes do not exist. In addition, (1.6a) forces the condition that $\mathrm{Re}[\varepsilon_1]<0$ if ε_2 is greater than zero — so that SPPs may only exist at the boundary between a metal and an insulator. Finally, substituting the free-electron dielectric function, (1.1) into the SPP dispersion relationship (1.7a) in the zero loss limit yields

$$\omega_{spp} \xrightarrow[k_x\to\infty]{} \frac{\omega_p}{\sqrt{1+\varepsilon_2}}\ . \qquad (1.8)$$

Figure 4 displays the SPP dispersion relationship for Ag and Au at ZnO and MgO interfaces.[47, 48] The SPP density of states is proportional to $k(dk/d\omega)$, so the SPP resonance occurs near the horizontal asymptote of the dispersion relationship—or roughly 2.9 eV at Ag-ZnO interfaces, 3.2 eV at Ag-MgO interfaces, and 2.4 eV-2.5 eV at Au-ZnO and Au-MgO interfaces.

Evaluating the decay constants given in (1.6) at the Ag-ZnO and Au-ZnO SPP resonance energies found in Figure 5, gives the evanescent decay lengths 23.4 nm for Au-ZnO, 39.0 nm for Au-MgO, 21.3 nm for Ag-ZnO, and 31.7 nm for Ag-MgO.

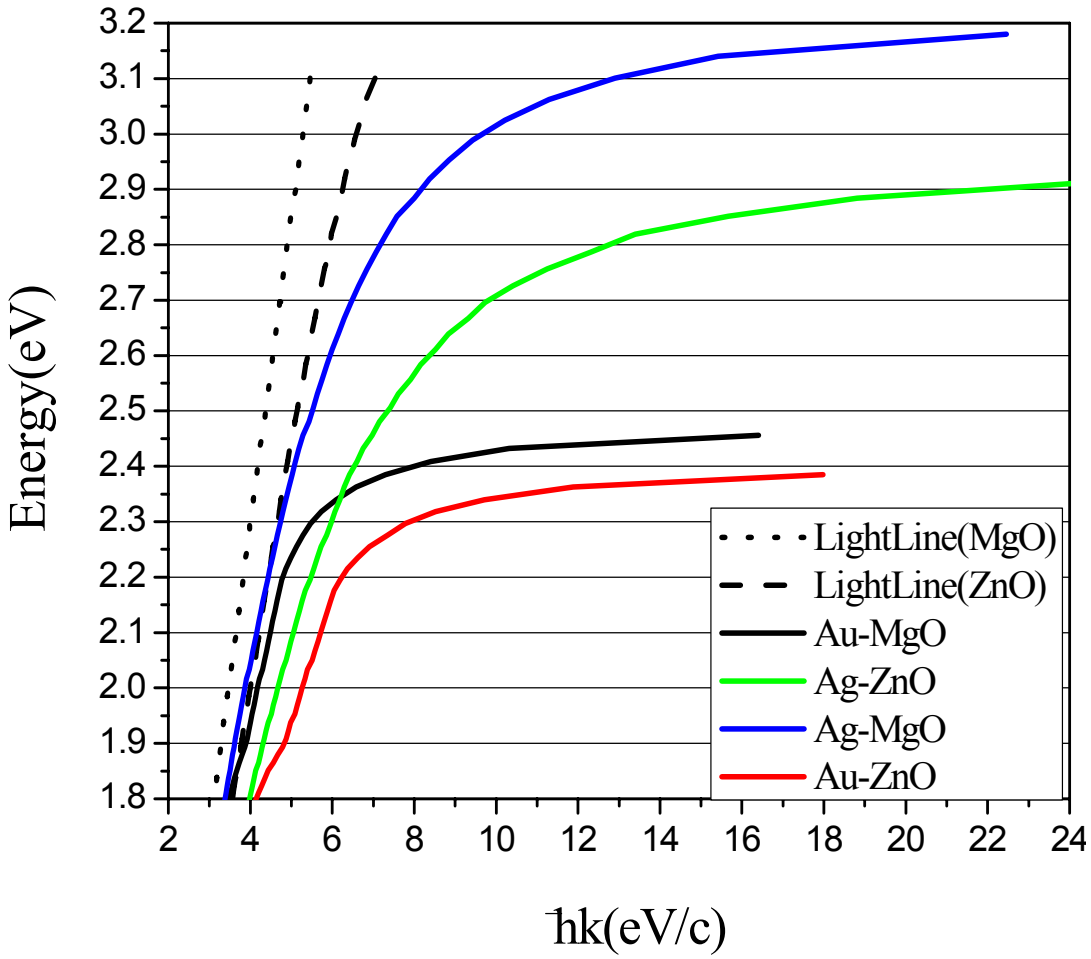

Figure 4: Dispersion relationship for SPPs in metal dielectric bilayers.

It is important to note that equation (1.7a) and Figure 4 demonstrate that the magnitude of the SPP wavevector k_x is larger than the photon wavevector ω / c for all ω. Unlike bulk plasmons or LSPs, it is impossible for light to couple directly to SPPs on a smooth metal-dielectric interface. One common method used to excite SPPs is prism coupling, illustrated in Figure 4. In these geometries, the beam is reflected at the interface between a high dielectric constant insulator and the metal, resulting in a reduced in-plane momentum $k_x = k\sqrt{\varepsilon}\sin\theta$ that allows an SPP to be excited at the interface between the lower index dielectric and the metal film. This technique was introduced

independently for metal films deposited directly onto prisms, and metal films near prisms by Kretschmann[49] and Otto[50] respectively. SPPs excited in this manner are leaky waves, which is to say that just as photons could excite the SPPs, the SPPs can radiate back into the prism.

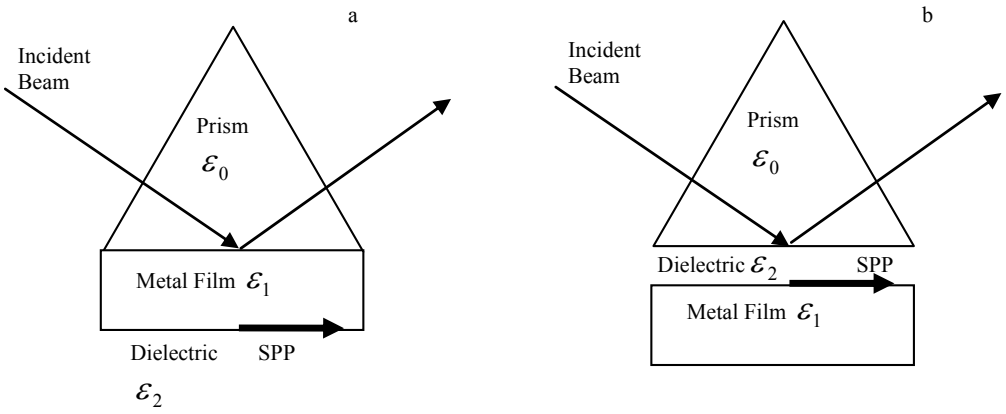

Figure 5: Kretschmann (a) and Otto (b) geometries for coupling photons into SPPs.

An alternate technique for exciting SPPs utilizes diffraction gratings or rough metal films. Metal films patterned with a periodic grating can provide the momentum mismatch necessary for light to excite SPPs:

$$k_{SPP} = k_x \pm nk_{grating} = \frac{\omega}{c}\sin\theta_0 \pm \frac{2\pi n}{a} \tag{1.9}$$

Light can only couple into metal gratings at defined angles of incidence given by (1.9), but because rough metal films can be described as the superposition of metal gratings, SPPs can be excited at any incidence angle by light. As with prism grating geometries, these geometries are inherently leaky.

1.3.2 Localized surface plasmons

LSPs are non-propagating excitations of the electrons in metallic sub-wavelength nanostructures coupled to an electromagnetic field, but unlike SPPs, LSPs can be excited

directly by light. The LSP can be understood in terms of the displacement of the electron cloud relative to the positively charged lattice, which results in a coulombic restoring force that causes resonances in the surface charge density oscillations. While the LSP resonance of an arbitrary geometry cannot be described analytically it is clear that the resonance energy and magnitude depend on the nanoparticle geometry as well as the dielectric functions of the metal and the surrounding medium. The quasi-static approximation allows for an approximate calculation of the LSP resonance by neglecting all retardation effects — which results in the assumption that all electrons in the nanoparticle respond to an external field simultaneously – and applying the Laplace equation. In the limit of a small spherical nanoparticle with radius $a << \lambda$, where λ is the excitation wavelength within the host dielectric of permittivity ε_m, the free electrons within the nanoparticle (permittivity ε) move in phase after plane-wave excitation, demonstrating a resonance at a specific wavelength which can be approximated a short distance r outside the nanoparticle (within the regime a<<r<<λ) as a dipole field given by:

$$\mathbf{E}_{out} = \mathbf{E}_0 + \frac{3\mathbf{n}(\mathbf{n}\cdot\mathbf{p}) - \mathbf{p}}{4\pi\varepsilon_0\varepsilon_m r^3}, \tag{1.10}$$

where the dipole moment **p** is defined as

$$\mathbf{p} = 4\pi\varepsilon_0\varepsilon_m a^3 \frac{\varepsilon - \varepsilon_m}{\varepsilon + 2\varepsilon_m}\mathbf{E}_0. \tag{1.11}$$

Introducing the polarizability α, defined through $\mathbf{p} = \varepsilon_0\varepsilon_m\alpha\mathbf{E}_0$, gives

$$\alpha = 4\pi a^3 \frac{\varepsilon - \varepsilon_m}{\varepsilon + 2\varepsilon_m}, \tag{1.12}$$

at which point, the scattering and absorption cross sections can be defined as

$$C_{abs} = \frac{2\pi}{\lambda}\mathrm{Im}[\alpha], \tag{1.13}$$

and

$$C_{sca} = \frac{1}{6\pi}\left(\frac{2\pi}{\lambda}\right)^4 |\alpha|^2. \tag{1.14}$$

The scattering efficiency can be defined as $Q_{sca} = C_{sca}/(C_{csa} + C_{abs})$.

Equations 1.11 and 1.12 illustrate the LSP resonance (known as the Fröhlich condition) at $\varepsilon = -2\varepsilon_m$ in the dipole approximation. Noble metals such as Au, Ag, and Cu have a negative permittivity in the visible spectrum, allowing for a visible LSP resonance. Substituting the resonance condition into the free-electron dielectric function, (1.1) in the zero loss limit yields

$$\omega_{LSP} = \frac{\omega_p}{\sqrt{1+2\varepsilon_m}}. \tag{1.15}$$

Au and Ag have similar bulk plasmon energies because of their similar electron densities (n=5.9 x 10^{22}/cm^3 and 5.86 x 10^{22}/cm^3 respectively), but the LSP absorption peak for Ag nanoparticles in air with $a << \lambda$ is near 390 nm, compared with 520 nm for Au.[51, 52] This is a result of deviations from free-electron behavior due to relativistic core-electron effects and inter-band and intra-band transitions that are quite different for the two metals.

Particles with size approaching λ demonstrate a significant red-shift in LSP resonance accompanied by substantially broadened absorption peak. Both can be understood through the inclusion of higher order terms in the Mie theory of nanoparticle

scattering. Mie theory is not a theory in the traditional sense; rather it is an approximate solution to Maxwell's equations based on an expansion of the internal and scattered fields into normal modes described by vector harmonics. A full description of the Mie theory solution to Maxwell's equations can be found elsewhere.[53, 54] The first order expansion of the Mie theory solution gives the quasi-static approximation, and larger particles can be described by including second-order terms:

$$\alpha = \frac{1 - \frac{1}{10}(\varepsilon + \varepsilon_m)x^2 + O(x^4)}{\left(\frac{1}{3} + \frac{\varepsilon_m}{\varepsilon - \varepsilon_m}\right) - \frac{1}{30}(\varepsilon + 10\varepsilon_m)x^2 - i\frac{4V\pi^2\varepsilon_m^{3/2}}{3\lambda_0^3} + O(x^4)}V, \qquad (1.16)$$

where $x = \frac{\pi a}{\lambda_0}$ is a size parameter which describes the ratio of the radius to the free space wavelength. The x^2 term in the numerator of 1.14 describes the retardation of the exciting field over the volume of the sphere, resulting in a redshifted resonance. The x^2 term in the denominator also results in a redshifted resonance, due to the retardation of the depolarization field inside the particle. Further, the x^2 term in the denominator increases the polarization magnitude, and therefore decreases the effect of Im[ε] on the absorption, but this increased magnitude is counteracted by the radiation damping represented by the imaginary term in the denominator. Radiation damping is a result of radiative decay of the LSP into photons; this represents the most significant cause of the weakening of the LSP resonance strength with increasing nanoparticle volume. The imaginary term is therefore also responsible for a dramatic increase in the FWHM of the LSP extinction spectrum as the nanoparticle diameter increases.

Because of the relatively small values of Im[ε] seen in Au and Ag, and in order to minimize interband absorption, both metals are popular choices for plasmonic nanostructures in the visible and near-infrared, although Ag oxidation is a minor barrier to some applications. The imaginary component of the permittivity of Al is as much as twenty times greater than that of Ag in the visible and near-IR, but its near-UV LSP resonance makes it a third metal of significant interest in plasmonics.[55] Figure 6 illustrates FDTD simulation results for the LSP extinction spectra of Al, Ag, and Au nanodiscs 60 nm and 100 nm in diameter deposited on $ZnO/Zn_{0.85}Mg_{0.15}O$ quantum wells.

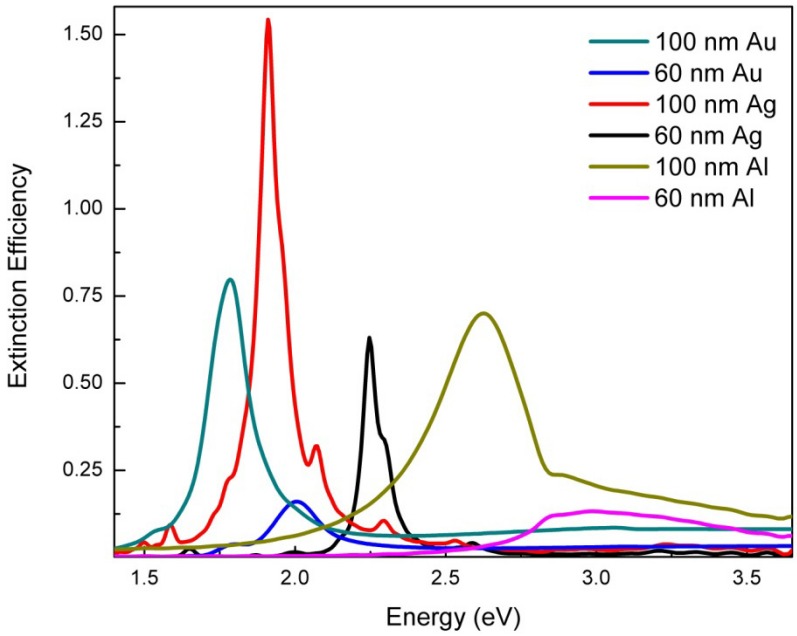

Figure 6: FDTD simulation results for extinction spectra of Au, Ag, and Al nanodiscs 20 nm in thickness and 60-100 nm in diameter deposited on ZnO quantum wells.

Because of the extensive use of rough thin films of Ag and Au in this dissertation, it is worthwhile to comment on LSP resonances supported on dielectric voids in a bulk metal medium. These systems can be understood simply by substituting ε for ε_m in

equation 1.12, resulting in the modified Fröhlich condition: Re[$\varepsilon(\omega)$]=- ε_m /2. In contrast to metal nanoparticles, the induced dipole moment for metal nanovoids is oriented antiparallel to the applied field.[46] Though voids in metal films cannot be treated analytically, they can be treated approximately as voids in bulk metal.

1.4 Plasmon-emitter coupling

The interactions between plasmons and luminescent centers in ZnO heterostructures near resonance with each other can dramatically enhance or reduce the emitter quantum efficiency, facilitate electromagnetically induced transparency, and elicit Fano-like resonance response, transient optical magnetism and disorder-induced light localization. Understanding the energetics and dynamics of the plasmon-exciton interactions is also vital to take advantage of myriad possible applications.

The bulk of the interactions examined in this dissertation focus on the weak-coupling regime, wherein the interactions of the plasmon near-field with dipole excitations in ZnO heterostructures can be described by perturbative techniques. The weak-coupling regime encompasses such well-known effects as enhanced absorption cross-sections, enhanced or damped radiative emission rates, and exciton-plasmon energy transfer. However, it is not trivial to predict the interactions in an arbitrary heterostructure, as current theoretical constructs do not allow for complex metal nanostructure geometries, and usually treat excitons only within the point dipole approximation.[56]

Plasmonic fields that are sufficiently strong and have significant spectral overlap with excitonic emitters can fall within the strong-coupling regime. The strong-coupling regime occurs when exciton-plasmon interactions result in modifications to both exciton

wave functions and plasmon modes, yielding changed resonance energies and linewidths. Theoretical treatments of complex heterostructures are still absent, but most simple systems are modeled as coupled oscillators.

1.4.1 Charge transfer processes

Several groups have reported enhancement of the ZnO band-edge photoluminescence with concurrent damping of the DAP emission in heterostructures of metal nanoparticles in contact with ZnO quantum dots and ZnO nanowires.[57-59] This was first shown with Au nanoparticles sputtered on oxygen deficient ZnO nanowires,[57] and subsequently with Au nanoparticles grown by chemical synthesis on ZnO nanoparticles[58] and nanorods.[59] These groups are in agreement that this is a result of the absorption of ZnO impurity emission by metal nanoparticles, followed by hot electron transfer to the ZnO conduction band, as illustrated schematically in Figure 6.[57]

Contrary to the behavior described above, photocatalysis experiments utilizing ZnO-noble metal colloids have demonstrated the flow of electrons from ZnO to the metal nanoparticles. Despite the position of the Au, Ag, and Cu conduction bands at least 0.5-1.0 V below the ZnO conduction band, sufficient charge accumulates on the noble metal particles to ensure equilibration of the Fermi levels between ZnO quantum dots and metal islands.[60] Indeed, the spectral change in the LSP resonance of metal nanoparticles bonded to ZnO quantum dots cannot be understood simply through the change in dielectric environment: instead it must be described by accounting for electron accumulation during photo-excitation. The enhanced band-edge photoluminescence in these cases is described as a result of reduced bleaching due to loss of the excess electron population.[60, 61] On the other hand, because 1D ZnO nanorods have a work function 0.1-

0.2 eV greater than that of Au, Fermi-level equilibration in nanorod composites will result in the net flow of electrons from Au to ZnO, which reinforces the argument presented in Figure 7.[62]

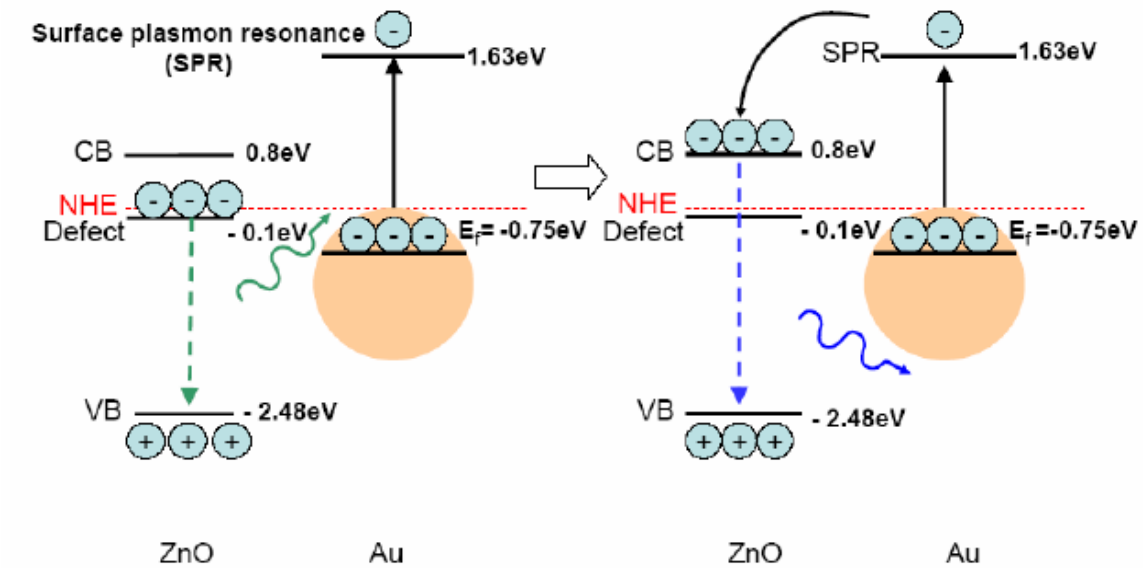

Figure 7: Schematic of the previously suggested mechanism for the enhancement of ZnO band-edge PL with concurrent damping of the DAP emission.[57]

Whether increased electron population in the ZnO conduction band results in bleached emission or enhanced emission is still unclear, but the results of the referenced papers suggest that this effect is highly dependent on geometry.[57-61] Further, because all of the referenced papers relied on heterostructures where the metal was in ohmic contact with the ZnO, it is difficult to separate effects due to hot-electron transfer from those due to near-field electromagnetics. None of the referenced papers considered the possibility of near-field plasmon-exciton coupling.

1.4.2 Purcell enhancement

The concept of using a resonant cavity to enhance the spontaneous emission probability of an emitter was first described in 1946 by Edward Purcell in the context of

radio frequency nuclear magnetic moment transitions coupled to a resonant electrical circuit. For such a system, the spontaneous emission probability is increased, and the relaxation time decreased by a factor:

$$F_p = \frac{3Q\lambda^3}{4\pi^2 V}, \tag{1.17}$$

where V is the volume of the resonator, and Q is its quality factor.[63] The analogy of an atom in a resonant shell or near an infinitely conducting surface was introduced in 1981 by Daniel Kleppner, along with the observation that the modified transition rate could be described by Fermi's golden rule[64]:

$$\Gamma_P = \frac{2\pi}{\hbar}\left\langle \vec{d}\cdot\vec{E}(a)\right\rangle^2 \rho(\omega) \tag{1.18}$$

where d is the excitonic dipole moment, E(a) is the SPP evanescent field at the position of an exciton, and $\rho(\omega)$ is the photon density of states. This reduces to equation 1.13 for systems where the atom-field interaction is unchanged because the mode density in a cavity is proportional to $Q/\omega V$.[64] This treatment demonstrates that, while a resonantly coupled cavity results in a dramatic increase in the transition rate, a mistuned cavity can result in significantly quenched emission—indeed, an ideal mistuned cavity would result in no spontaneous emission at all because no mode is available for the photon.[64] Numerical solutions to Maxwell's equations for a molecule near an infinite metal film suggest three decay channels: radiative emission, SPP excitation, and decay into "lossy surface waves" which consist of intraband electron-hole excitations in the metal Fermi sea.[65]

After Kleppner's paper, a significant number of experimental papers appeared that described the emission of atoms and molecules near Ag surfaces. A typical study is that of Barnes *et al*. examining the modification of spontaneous emission from a Langmuir-Blodgett film of Eu^{3+} ions into Ag surface plasmons, which demonstrated enhancement of the spontaneous emission into either radiative or waveguide modes, depending on the thickness of the dielectric.[66]

The first report of resonant exciton-plasmon coupling in the context of the Purcell-effect was by Yablonovich *et al.* in 1999 in an examination of an InGaN/GaN quantum well with a 8 nm Ag film positioned 12 nm from the well.[67, 68] They emphasized the distinction between exciton-plasmon interactions and molecule-plasmon interactions with the observation that only two decay channels are available to exciton-plasmon systems, because momentum matching to electrons in the Fermi sea requires the large k vector associated with molecular point-dipole radiators. Since excitonic wave functions are spatially broader than molecular wave functions, intraband excitations in the Ag Fermi sea are forbidden because of the momentum mismatch.[67] As a result, semiconductor thin films or quantum wells separated by only a few nanometers from metal films supporting resonant SPPs should admit Purcell factors of 1000 or more without being subject to dissipation arising from the intraband excitations occurring in molecule-metal systems. No Purcell factors of this magnitude have yet been demonstrated; however, Yablonovitch *et al.* demonstrated a 55-fold quenching of the InGaN/GaN quantum-well luminescence, which they attributed to rapid coupling of exciton emission into SPPs.[67] This was followed by a report demonstrating a factor of 92

increase in the recombination rate of InGaN/GaN quantum-well excitons, roughly matching the calculated Purcell factor.[68]

An initial report on multilayers of 50 nm ZnO films with Ag and Au films 10 – 250 nm in thickness demonstrated an enhancement factor of up to 10 of the band-edge photoluminescence in the ZnO-Ag multilayers and attributed the enhancement to the Purcell effect.[69] However, because these results were based on Ag films deposited directly on ZnO, it is difficult to say whether the enhancement was a result of near-field coupling or charge-transfer effects. No enhancement in the ZnO-Au multilayers was observed that could not attributed to increased photon density due to reflection from the Au films. The lack of enhancement in ZnO-Au multilayers is not unexpected due to the large (0.8eV) spectral separation between the ZnO exciton and the Au SPP. That this enhancement is related to the Purcell effect is corroborated by analyzing the enhancement as a function of temperature. The enhancement of 67 nm films of ZnO capped with 50 nm Al films has been shown to vary with temperature roughly proportional to the calculated Purcell factor.[70] Ag capped ZnO films on substrates of silicon, sapphire and quartz have been shown to exhibit significantly different enhancement factors as a result of power lost to substrate waveguide modes, so considerable care must be taken in the sample design.[71]

Because the Purcell factor in semiconductor-metal multilayered structures is a result of competition between spontaneous emission into free space and spontaneous emission outcoupled through SPP modes, the effective Purcell factor can be written in terms of the radiative and non-radiative emission rates, and the SPP coupling rates, designated $\Gamma_0, \Gamma_{nr}, and\ \Gamma_P$ respectively:

$$F_p = \frac{\Gamma_P + \Gamma_o + \Gamma_{nr}}{\Gamma_0 + \Gamma_{nr}} = 1 + \frac{\Gamma_P}{\Gamma_0}\eta \quad , \tag{1.19}$$

where $\eta = \frac{\Gamma_o}{\Gamma_0 + \Gamma_{nr}}$ is the quantum efficiency of the semiconductor outside the presence of plasmonic elements. The classical radiative recombination rate is

$$\Gamma_0 = \frac{4nd^2\omega^3}{3\hbar c^3} \quad , \tag{1.20}$$

where n is the semiconductor refractive index and d is the dipole moment. Γ_P can be calculated from Fermi's golden rule, where the plasmon density of states is obtained from the dispersion relationships calculated in section 1.3.1 by:

$$\rho(\hbar\omega) = \frac{2\pi k\, dk}{(2\pi)^2 d(\hbar\omega)} A = \frac{A}{4\pi}\frac{d(k^2)}{d(\hbar\omega)} \quad , \tag{1.21}$$

and, because the SPP evanescent field varies only in the z-direction, E(a) is normalized to a half-quantum for zero-point fluctuations:

$$E^2(a) = \frac{\hbar\omega/2}{A/8\pi \int_{-\infty}^{\infty} \frac{\partial(\omega\varepsilon)}{\partial\omega}\left|E(z)\right|^2} E_0^2(a) \quad , \tag{1.22}$$

where $E_0(a)$ is the un-normalized SPP field, and A is the in-plane quantization area. In evaluating the integrand of equation 1.18, it should be clear that ε varies with both frequency and vertical position within the heterostructure.[67, 68] Finally, combining equations 1.18-1.22, and accounting for polarization with a factor 1/3, the Purcell enhancement factor for plasmon coupled emission can be written as:

$$F_P = 1 + \frac{2\pi d^2 \omega E_0^2(a)\eta}{3\hbar \int_{-\infty}^{\infty} \frac{\partial(\omega\varepsilon)}{\partial\omega} E_0^2(z)dz} \frac{d(k^2)}{d(\hbar\omega)} \quad . \tag{1.23}$$

Of course, this methodology deals only with SPP-exciton coupling. There has been some work describing the Purcell enhancement of excitonic emission due to LSP dipole fields through the Legendre expansion of the metal nanoparticle near-field which ultimately shows the $1/z^6$ dependence on plasmon-emitter spacing expected from Fermi's golden rule. However, because this dissertation does not deal directly with the Purcell effect for LSP-exciton systems, the full derivation is neglected here.[72]

1.4.3 Absorption enhancement

While the Purcell enhancement methodology developed in 1.4.2 results in reliable estimates for the enhancement factor for electroluminescence, it is significantly more complicated to model photoluminescence enhancement because there are two enhancement mechanisms in play: the Purcell enhancement of the spontaneous emission can be described as before, but the absorption rate can also be dramatically altered in the vicinity of SPPs or LSPs.

Enhancing semiconductor absorption is a topic of huge interest in the literature because of the potential applications in fourth-generation solar cells.[73-77] The concept of using scattered light to increase the optical pathlength within a solar cell has been utilized since 1982, when it was demonstrated theoretically that light incident on a Si solar cell with optimal roughness would travel $2n^2$ further within the solar cell than light incident on a smooth surface, resulting in an effective absorption coefficient $4n^2$ greater than is seen for a smooth surface.[78] Experiments performed more recently using metal thin film and metal nanoparticle modified solar cells have demonstrated that these plasmonic

fourth generation solar cells can in fact exceed the absorption limit defined for rough surfaces.[75]

A basic understanding of the effect of plasmonic elements on semiconductor absorption can be found by analyzing the absorption of a semiconductor thin film coated with metal nanoparticles with sufficiently large spacing to avoid plasmon-plasmon coupling. The intensity of light at a given position z within a thin film for incident intensity I_{in} is given by Beer's law:

$$I(z) = I_{in} e^{-\alpha z}, \tag{1.24}$$

where α is the absorption coefficient of the thin film. Treating the thin film-metal nanoparticle composite requires the inclusion of terms which describe the scattering of light by the metal nanoparticles. Assuming that all of the power is either absorbed in the semiconductor, the metal or the substrate, or reflected or backscattered, and neglecting interference between any scattering sources, the fraction of the light absorbed in the semiconductor is given by:

$$A(\lambda) = \xi Q_{scat}(\lambda) f_{substrate}(\lambda) + (1 - \xi Q_{scat}(\lambda))(1 - R_s(\lambda)), \tag{1.25}$$

where ξ is the metal nanoparticle surface coverage fraction, Q_{scat} is the scattering cross section of the nanoparticle normalized to the physical nanoparticle cross section, $f_{substrate}$ is the fraction of scattered light which is forward scattered into the substrate, and R_s is the reflection from the semiconductor interface in the absence of any nanoparticles.[73] Consequently, the semiconductor absorption can be optimized by maximizing the metal nanoparticle scattering cross-section. For metal nanoparticles with $a << \lambda$, the absorption cross-section dominates the scattering cross-section, but as the particle size

increases, Q_{scat} / Q_{abs} increases as well, until multipolar effects begin to take over for nanoparticle sizes approaching λ. The need for larger particles means that cells which utilize Au and Ag nanoparticles show the greatest enhancement in the near to mid-IR, which is ideal for most solar cell designs because of the relatively weak Si absorption in that portion of the spectrum.[1, 74, 77, 79, 80] Because each nanoparticle geometry will scatter light differently, the proper heterostructure design to maximize semiconductor absorption is a problem of ongoing interest.[73]

Designs involving metal thin films instead of metal nanoparticles have also demonstrated strong enhancement of the semiconductor absorption because of the strong SPP evanescent fields supported at the metal-semiconductor interface. While the evanescent decay length is limited to tens of nanometers within the semiconductor, the enhanced absorption offered due to the evanescent fields allows for solar cells of thickness much less than λ while maintaining the absorption of solar cells microns in thickness—resulting in dramatically reduced costs and reduced material requirements for equivalent solar cells.[75]

1.4.4 Strong-coupling regime

The last several years have seen the onset of literature describing coherent coupling energetics and dynamics in metal-semiconductor nanostructured materials.[81-84] The seminal article found the plasmon-exciton coupling energy for J-aggregate /Au nanoshell composites by tuning the plasmon resonance across the J-aggregate exciton emission energy, while developing a model for the hybrid state(coined the "plexciton") based on Gans theory.[81] A more recent paper developed a theory of hybrid Tamm

plasmon-exciton states in semiconductor microcavities coated with metal islands for possible applications using exciton-polariton integrated circuits.[82]

The theory of strong-coupling was first developed for Rydberg atoms in resonant cavities using the Jaynes Cummings Hamiltonian,[85, 86] and later applied to semiconductor quantum dots (SQDs) in nanocavities.[87] These systems have a distinct advantage over plasmon-exciton systems in their relative theoretical simplicity, and they therefore present an ideal model for strongly coupled systems. While there has been significant interest in the Purcell enhancement seen in the weak-coupling of SQDs to microcavities and nanocavities for the last few decades, it is only recently that researchers have been able to fabricate nanocavities with sufficiently small mode volume V and sufficiently high quality factor Q to enter the strong-coupling regime. For a SQD with dipole moment μ in a nanocavity, the exciton-cavity coupling constant[88] is defined by $\hbar g = \left|\left\langle \boldsymbol{\mu} \cdot \mathbf{E} \right\rangle\right|$, or

$$g = \mu E_{vac} / \hbar \,, \tag{1.26}$$

where E_{vac} is the vacuum field amplitude defined by[87]

$$E_{vac} = \frac{1}{n}\sqrt{\frac{\hbar\omega}{2\varepsilon_0 V}} \,. \tag{1.27}$$

The strong-coupling regime is defined by $g < \gamma, \kappa$, where γ and κ are the homogenous decay rates of the SQD and the cavity respectively. Therefore, it is necessary to obtain a small cavity volume with a large quality factor in order to minimize g and maximize κ. It is worth noting that in the weak-coupling regime ($g > \gamma, \kappa$), the

Purcell factor is given by $F_P = 4g^2/\kappa\gamma$, but as the strong-coupling regime is approached, Purcell enhancement fails, and the enhancement factor increases faster than F_P.[87]

While the complexity of LSP-exciton and SPP-exciton systems prevents a thorough analytical treatment of the coupling energetics, SPP-exciton systems can be understood as analogous to the previously described strongly coupled heterostructures through the mode length L of a SPP:

$$L = \frac{\int_{-\infty}^{\infty} \frac{\partial(\omega\varepsilon)}{\partial\omega}|\mathbf{E}(z)|^2 dz}{\max\left[\frac{\partial(\omega\varepsilon)}{\partial\omega}|\mathbf{E}(z)|^2\right]}, \tag{1.28}$$

where the integral is evaluated normal to the metal-semiconductor interface.[89] However, there is currently no theoretical discussion of LSP mode volume, and approaches like equation 1.28 neglect resistive loss within the metal film.

While there exists at least one paper that discusses modifications to Eq. 1.28 to address resistive losses[89], a conceptually simpler approach based on a coupled oscillator model utilizing the plasmon exciton Hamiltonian:

$$H = \begin{pmatrix} E_{pl} - i\gamma_{pl} & \Delta/2 \\ \Delta/2 & E_{ex} - i\gamma_{ex} \end{pmatrix}, \tag{1.29}$$

where Δ is the plasmon-exciton interaction energy, E_{pl} is the LSP resonance, E_{ex} is the uncoupled exciton energy, and γ_{pl} and γ_{ex} are the linewidths of the LSP and the exciton respectively.[84, 90] This coupled oscillator differs significantly from the Jaynes-Cummings model used to describe Rydberg atom systems and quantum boxes because while

excitons behave as bosons under weak excitation, quantum boxes and Rydberg atom systems are fermionic systems.[88] The eigenenergies of equation 1.29 can be understood as high and low energy branches in the 'plexciton' dispersion relationship. The interaction energy Δ, otherwise known as the Rabi splitting energy, appears in the dispersion relationship as the minimum energy separation between the upper and lower branches.

The absorption spectrum of metal nanoparticles in a strongly coupled plasmon-exciton system will generally exhibit a Fano resonance. The Fano resonance can be understood as the interference between a localized, resonant state with a broad continuum — in this case, the interaction of an exciton with a LSP or an SPP — and presents itself as a sharp, asymmetric dip or peak in the transmission spectrum due to destructive or constructive interference respectively.[91, 92]

CHAPTER 2: EXPERIMENTAL TECHNIQUES

The ZnO thin films and quantum wells studied in this dissertation were grown by both electron beam evaporation and pulsed laser deposition (PLD). The metal nanostructures were fabricated by electron beam lithography (EBL) and subsequent electron beam evaporation, and the extinction spectra of the nanoparticle arrays were measured using a home-built confocal microscope. Photoluminescence (PL) spectroscopy and pump-probe spectroscopy were used to characterize the heterostructure energetics and dynamics. Each technique is described below.

2.1 Pulsed Laser Deposition (PLD)

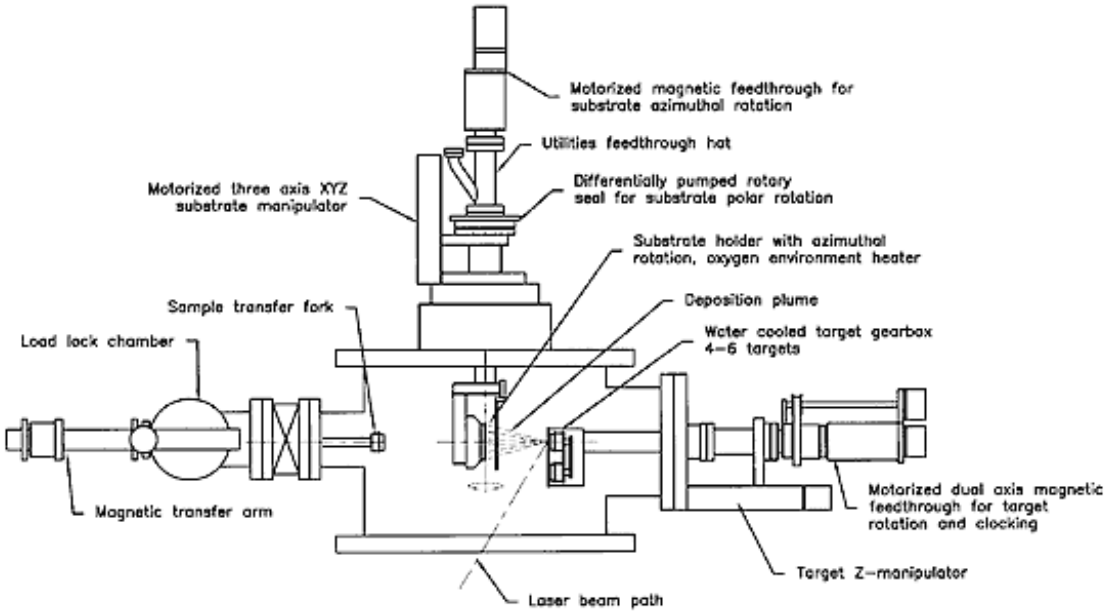

Figure 8: Schematic of Thermionics PLD chamber used for ZnO quantum well deposition.[93]

Despite a variety of reports on the laser ablation of solid targets since the 1960s, PLD is a fairly new deposition technique when compared with sputtering and molecular beam epitaxy (MBE). The name 'pulsed laser deposition' was agreed upon in 1989 at the first MRS symposium on pulsed laser ablation.[94] In metal oxide PLD, energetic nanosecond laser pulses — typically from an excimer laser — ablate the target; the penetration depth of the ultraviolet laser pulses generally leads to stoichiometric ablation. For a planar target, the ablated material is ejected in an elliptical plume normal to the target surface with an angular distribution described by $f(\theta) = (\cos\theta)^n$ where n is between 1 and 30 and is determined by the PLD geometry.[94] PLD has become a frequently used tool for epitaxial and textured growth of thin film oxides because it allows for near-stochiometric deposition and epitaxial deposition at reduced growth temperature compared with MBE. Moreover, PLD offers the flexibility of variable backing-gas pressures.

The ZnO films and quantum wells were grown by PLD as part of my internship in David Norton's laboratory at the University of Florida in the Thermionics ultrahigh-vacuum chamber illustrated schematically in Figure 7.[93] The load-lock chamber is independently pumped by a mechanical pump and turbo-molecular pump with a base pressure of 10^{-6} Torr attainable within roughly 15 minutes. The main chamber is pumped by two turbo pumps, and has a base pressure of roughly $2*10^{-8}$ Torr. Samples mounted on the substrate holder were heated to 700ºC, and all depositions were performed with a backing pressure of 1 mTorr O_2.

The ablation laser used was a Lambda-Physik CompeX 205 KrF 248 nm excimer laser producing 430 mJ pulses at a repetition rate of 1 Hz. The beam power at the target

was measured to be 150-160 mJ, and the spot size was nominally 5 mm^2. In order to maintain uniform stoichiometry and normal ablation trajectories, the beam was continuously rastered across the target, and the target rotated about its central axis throughout every deposition.

The targets were made from high purity Alfa-Aesar Puratronic metal oxide powders (99.9995% ZnO and 99.998% MgO). The $Zn_{0.95}Mg_{0.05}O$ target was fabricated by grinding 11.479 g ZnO and 0.2992 g MgO with an alumina mortar and pestle for 20 minutes. The powder was then compacted into a 1" diameter disc in a stainless steel die with an applied pressure of 5 metric tons for 3 minutes, transferred to a clean alumina crucible, and sintered at 1200ºC for 12 hours. The ZnO target was prepared identically with the ZnO powder.

The percent lattice mismatch for several commonly used substrates is shown in table 1. $ScAlMgO_4$ is a material designed as a lattice matching substrate for epitaxial ZnO growth composed of alternating stacking layers of wurtzite (0001)(Mg, Al)O*x* and rocksalt (111) ScO*y*[95, 96] but it is grown using the Czochralski process, and it has not been commercially available since 2000. Therefore, because of cost considerations and in order to take advantage of the tendency of ZnO to grow in a c-orientation, all structures grown by PLD were grown on (0001) 2-side-polished sapphire substrates.

In order to bond to the holder at high deposition temperatures, the substrates were mounted to the deposition stage using Ted Pella 'Leitsilber 200' silver paint, and left to dry for at least 4 hours prior to mounting the stage in the chamber. Because of adhesion concerns, the substrates were not rotated during deposition.

Substrate	Structure	Orientation	% Mismatch
***c*-plane Al2O3**	Hexagonal	(0001)	19[97]
ScAlMgO4	Hexagonal	(0001)	0.09[95, 96]
GaN	Wurtzite	(0001)	1.9[98]
SiC wurtzite	Wurtzite	(0001)	5[97]
Si	Diamond	(100)	67[99]

Table 1: Lattice mismatch for ZnO substrates

2.2 Electron beam lithography

Electron beam lithography (EBL) is a patterning technique wherein a focused keV electron beam is scanned in a predefined pattern over a substrate coated with either a positive or negative resist. The bonds in positive resists are broken after exposure to the electron beam, resulting in a significantly more soluble resist which is chemically removed by a 'developer' leaving the inverse image of the written pattern. Exposure of negative resists results in cross-linking between polymers which significantly reduces the solubility, so that development removes the un-patterned resist, leaving the image of the written pattern. These patterns are transferred to the substrate by etching or film deposition followed by the 'lift-off' of the remaining resist. EBL is preferable over photolithography for its higher resolution — features of 15-20 nm are commonly achieved — but as a result of the serial nature of EBL patterning, it is a significantly more time-consuming process. The system used for this project is an e_LiNE manufactured by Raith USA Inc, integrated into a Zeiss scanning electron microscope.

For this work, EBL was used to fabricate arrays of Au, Ag, and Al nanodiscs on ITO-coated glass that were subsequently coated with MgO and ZnO, as well as arrays of Al nanodiscs on $ZnO/Zn_{0.85}Mg_{0.15}O$ quantum wells. These samples were cut to roughly 1 cm x 1 cm and cleaned via sonication for 5 minutes in trichloroethylene, acetone,

methanol, and deionized water consecutively. polymethyl methacrylate with molecular weight of 950,000 dissolved in anisole (950PMMA A2) was deposited on the samples by spin coating at 4000 rpm for 45s and subsequently baked on a hot plate at 180ºC for 2 minutes. This process yields a PMMA film roughly 60 nm thick.

Because the sheet resistance of the ZnO QWs (roughly 800kΩ) prevents reliable SEM imaging for magnifications greater than 5 kX, and in order to prevent charging problems during lithography, the PMMA coated QWs were initially coated with 3 nm Au by sputtering for 260 s. After exposure, the Au film was removed from the QW structures by etching in Transene© TFA gold etch for 30-60s. However, the resolution of the patterns on these samples was significantly worse than the resolution of patterns deposited on conducting substrates. Ultimately, it was determined that the Au films could be avoided, and the lithography could be performed directly on the QWs. Some charging problems presented themselves during write-field alignment, but performing the alignment near the sample clip was usually sufficient to avoid excess charging.

Because all plasmonic elements had circular symmetry, dot doses could be used instead of area doses. Instead of breaking up each disc into 2 nm discrete units, the discs were formed by moving the beam to the center of each disc and varying the dwell time in order to control the disc size. Ultimately, dot doses of 2.5-80 fC were used for the nanodiscs, and area doses of 100 $\mu As/cm^2$ were used for markers and labels. A 20kV electron beam was used with a 10 μm aperture and a 100 μm write field.

The exposed PMMA was removed by agitating twice for 30s in a 1:3 solution of methyl isobutyl ketone**:**isopropyl alcohol (MIBK:IPA), then cleaned in IPA and dried with pressurized air. Metal films 20 nm thick were deposited by electron beam

evaporation as detailed in the following section, or by thermal evaporation, and the unexposed PMMA was removed by agitating for roughly 15 minutes in remover PG at 75ºC.

2.3 Electron beam evaporation

Most of the metal films for this project were deposited by electron beam evaporation, as were the MgO and ZnO thin films. Electron beam evaporation is a physical vapor deposition technique wherein an electron beam of 1-30kV is steered onto a target, thereby melting the target and subsequently evaporating the material, which is deposited on the substrates mounted 5 - 20 cm above the target. The electron beam evaporator used for this experiment is a 3-crucible, single filament, Thermionics 100-0030 system with a beam voltage of 4kV, a continuously variable beam current from 0-750mA, and a base vacuum of $3x10^{-6}$ Torr. The deposition rate and deposition thickness were measured using a quartz crystal monitor, (Inficon, 750-211-G1 with XTM/2) and the current was varied in order to maintain deposition rates of 0.01 nm/s. The targets used for each material were high purity Alfa-Aesar Puratronic metal oxide pellets of at least 99.99% purity. Three crucibles could be used without breaking vacuum, allowing for successive depositions without exposure to atmosphere.

Figure 9 demonstrates the characteristic PL spectra for ZnO films deposited with a deposition rate of 0.01 nm/s. These films consistently demonstrated band-edge emission dramatically stronger than any impurity emission, indicating that room temperature e-beam evaporation yields good stoichiometry and film quality.

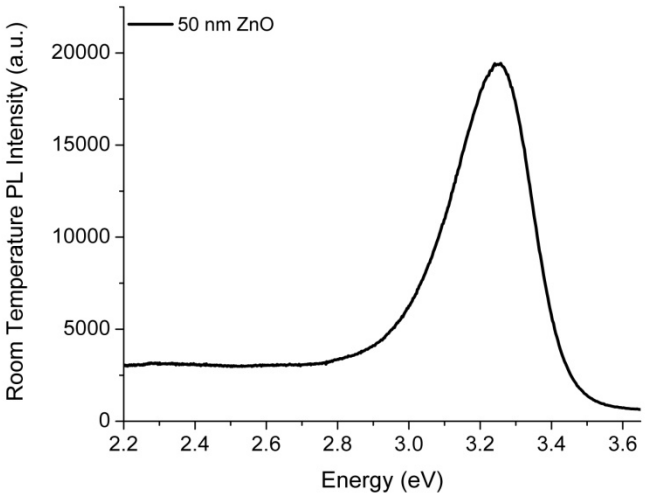

Figure 9: Typical room temperature PL spectrum for e-beam evaporated 50 nm ZnO thin film.

2.4 Thermal evaporation

After multiple attempts to deposit nanodisc arrays by electron beam evaporation resulted in only sparse nanodiscs across the intended 100 μm square array, arrays deposited by thermal evaporation were shown to produce significantly more consistent arrays. Presumably this was a result of smaller grain sizes in the thermally evaporated Al films, but no systematic investigation was performed after it became clear that thermal evaporation was a superior approach.

Thermal evaporation is a physical vapor-deposition technique, though unlike e-beam evaporation, it relies on resistive heating of a tungsten boat in order to evaporate the target pellets. All evaporations were performed using the programmed 20 nm Al deposition on the K.J. Lesker Nano36 thermal evaporator located in Stevenson Center 6509 at a base pressure of 10^{-7} Torr, while using a quartz crystal monitor to determine the film thickness. Aluminum pellets (99.999% purity) from K. J. Lesker were used as the target material.

2.5 Tube furnace annealing

While the QW structures were grown at 700°C in order to optimize the surface roughness and optical quality, the e-beam evaporated ZnO thin films were judged to be of sufficient quality after room temperature evaporation that annealing was unnecessary. However, low-temperature annealing provided a simple approach for the creation of various defect sites in ZnO thin films discussed in chapter 4.

The samples were annealed in a 55 mm OD thick walled glass tube with a Lindberg/Blue single zone furnace which allowed for up to 50 cubic centimeters per minute (ccm) of O_2, N_2, or Ar gas. The samples were loaded after the furnace had reached the set temperature of 400-800°C with a background of 9.8 ccm O_2. The furnace was allowed to cool to room temperature before the samples were removed. In order to avoid atomic diffusion between layers, ZnO films were annealed immediately prior to deposition of MgO and ZnO thin films.

2.6 Photoluminescence

Photoluminescence (PL) spectra taken at Fisk University were acquired using a vertically polarized 325 nm HeCd laser, providing an excitation power density of 600 W/cm^2 at a 45º incidence. The ZnO PL emission was measured from 328 to 666 nm with a 0.5 s exposure on an Oriel monochromator (MS257TM) with a thermoelectrically cooled CCD detector. Other authors using a frequency tripled Nd-YAG laser pump showed that the DAP emission begins to saturate for powers greater than 1500 W/cm^2, indicating — in agreement with our own observations — that saturation of the DAP emission occurs at powers higher than those used in our experiment.[100] Some low-temperature spectra were achieved using a MMR optical temperature control stage which

achieves temperatures as low as 80K by utilizing Joule-Thomson expansion of ultra-dry high-pressure N_2 and a counter-current heat exchanger. In principle, the MMR system allows for low vibration measurements, cool-down times of only 15 minutes, temperature control to within 0.1K, and the possibility of transmission measurements. However, a leak in the porous alumina gas cell resulted in cool down times of more than 3 hours, limiting the number of low-temperature spectra.

PL spectra were acquired at the University of Florida using a vertically polarized 325 nm HeCd laser, providing an excitation power density of 1 W/cm^2 at a 45º incidence. ZnO QW spectra were taken from 330 to 430 nm using a 0.3 m scanning grating monochromator with a Peltier-cooled GaAs photomultiplier. Low temperature measurements were taken at 15K with a CTI Cryodyne cryopump retrofitted with an 8 inch diameter fused silica window.

2.7 Confocal absorbance spectroscopy

The absorbance spectra of the EBL fabricated nanoparticle arrays were measured using a simple homebuilt confocal microscope in the transmission configuration illustrated in Figure 10. A Spectral Products tungsten lamp (ASBN-W-L) provided a 2000 lumen near-blackbody source with a color temperature of 3000 K. The light was coupled into and out of the microscope with solarization resistant, 600 μm core diameter fibers (Avantes FC-UV600-2), and a 50:50 cage-mounted beamsplitter (Thorlabs CM1-BS1) was utilized in conjunction with a CCD camera (Watec 902B) to image the beam profile on the sample. Because arrays 100 μm in size can be quickly fabricated using dot doses, 5x objectives were sufficient to obtain a beam spot size slightly smaller than the array on the sample surface. The focusing objective had a 0.12 numerical aperture, and

the collection objective had a 0.20 numerical aperture. The collected spectra were measured using an Avantes 2048-2-usb2 portable spectrometer with UV-enhanced optics. The absorbance—or optical density—of the nanoparticle arrays was defined as

$$OD = -\log_{10}\left(\frac{I_{tr} - I_d}{I_0 - I_d}\right), \tag{2.1}$$

where I_{tr} is the transmitted intensity, I_d is the background intensity while the lightsource is blocked, and I_0 is the incident intensity. In general, the transmitted intensity through the quantum well was used as I_0, so as to facilitate direct analysis of the LSP absorbance. In order to allow for variable-temperature absorbance spectra between 77K and 335K, an Oxford Instruments OptistatCF cryostat was used in a N_2 fill cryostat configuration.

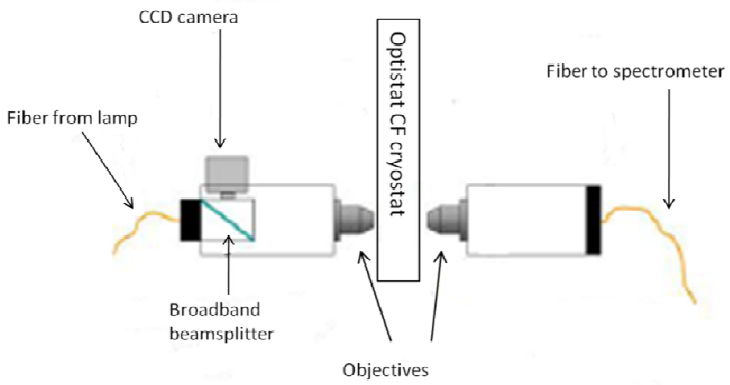

Figure 10: Schematic of the transmission microscope[101]

2.8 Pump-probe spectroscopy

Pump-probe spectroscopy — or transient absorption spectroscopy — is a commonly used technique to measure relaxation processes on femtosecond to nanosecond timescales. A high power-density pump beam excites the sample, and a relatively low power-density probe beam whose path-length is controlled by a delay stage — thereby varying the arrival time of the probe pulse — measures the transmittance or

reflectance of the sample, yielding the relative charge carrier population at the probed energy as a function of time. In principle, the power of the probe beam is sufficiently weak to be non-interacting with the pump beam, but recent reports have demonstrated an unexplained significant enhancement of the supercontinuum generated by an 800 nm pump beam by a weak visible seed beam, suggesting that even probe beams with less than 1% the power of the pump could interact with the pump beam.[102] However, it is likely that this effect does not exist at the comparatively low power densities used for pump-probe spectroscopy.

2.8.1 Ultrafast laser system

The pump-probe spectroscopy performed for this project relied on a LightConversion Traveling-wave Optical Parametric Amplifier of Superfluorescence (TOPAS), which was pumped by a Quantronix Titan regenerative amplifier which in turn was pumped by a Quantronix Darwin Nd:YLF laser, and seeded by a Coherent Mira Ti:sapphire oscillator, as seen in Figure 14.

The Mira is a Kerr-lens modelocked linear Ti:sapphire cavity with a birefringent filter, a dispersion-compensating prism pair, and a beam-aperturing slit used to select mode-locked operation, [103] Pumped by a Coherent Verdi 5W, 532 nm, CW diode pumped solid state laser, the Mira produces roughly 900 mW of 76 MHz pulses at 800 nm with 150 fs pulse durations. The wavelength can be tuned from at least 750 nm to 840 nm, but the regenerative amplifier is optimized for 800 nm.

The Titan amplifier is a regenerative, multipass Ti:sapphire amplifier in which the pulse amplification is maximal at 800 nm. It is designed to amplify the 76 MHz, nanoJoule pulses to 1 kHz pulses with 3.5 mJ per pulse. The Titan employs the chirped

pulse amplification (CPA) technique, so — as seen in Figure 12 — it is composed of a pulse stretcher, followed by the multipass and regenerative amplifiers respectively, and then by the pulse compressor.

CPA was first developed as a laser amplification technique at the University of Rochester in 1985, after first use in the 1960s as a radar amplification technique.[104] It was a necessary step forward in order to avoid the peak intensities of GW/cm^2 that would damage the Ti:sapphire rods. In a CPA system, the femtosecond seed pulse is stretched temporally by several orders of magnitude by using a pair of diffraction gratings prior to being introduced to the gain medium. The stretched pulse has a sufficiently low peak power that it may be introduced to the gain medium without damage, and by compressing the amplified pulse to the original pulse width of 150 fs with a pair of gratings (in the reverse of the pulse stretching procedure), peak powers six orders of magnitude greater than those seen in the Ti:sapphire oscillator can be achieved.

The Titan output provides 1.65 W to each of two TOPAS optical parametric amplifiers and 250 mW to a third box from LightConversion which is identical to the two TOPAS boxes except that it does not contain a BBO crystal—as a result, the third box provides 800 nm pulses with the same delay as the pulses which exit the two TOPAS boxes. Combined, the TOPAS boxes provide tunable output from 185 nm to 20000 nm, as indicated by Figure 11.

Each TOPAS is made up of a superfluorescence generator, three preamplifiers, and a power amplifier - all of which are arranged to utilize a single 5 mm BBO crystal (cut at 28°) as indicated in Figure 13.[105] After generation of the superfluorescence by the first pass through the BBO crystal, the preamplifier passes determine the signal (high

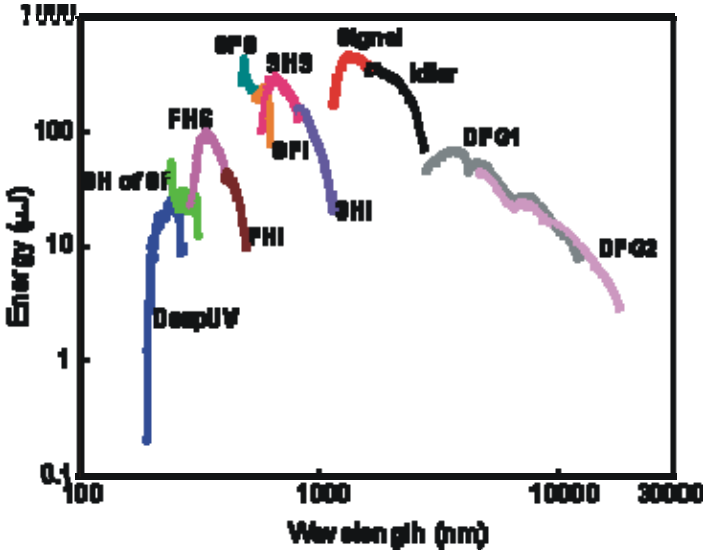

Figure 11: Spectral energy distribution of TOPAS optical parametric amplifier[105]

frequency) and idler (low frequency) outputs via the phase-matching angles of the crystal, prior to the final amplification of the signal or idler by the final pass through the BBO crystal coincident with the power amplifier pulse. Birefringent plates are utilized to separate the signal and idler pulses temporally, allowing the amplifier pulse to amplify selectively either the signal or the idler beam.

Combined, the signal and idler provide a continuously tunable output from 1.0 to 2.6 µm, but second harmonic generation (SHG) must be used to reach the UV-visible spectrum, and difference frequency generation (DFG) must be used to reach the mid-to-deep IR. As a result, two TOPAS boxes are needed; one with a DFG attachment, and one with an SHG attachment. Only the TOPAS with the SHG attachment was needed for this dissertation, and the attachment in question utilized two BBO crystals to provide either the second or the fourth harmonic of the signal and idler, as well as providing the sum frequencies of the signal and idler, and the sum frequencies of the signal and pump, as well as the second harmonic of those combinations. These permutations are detailed in Figure 12.

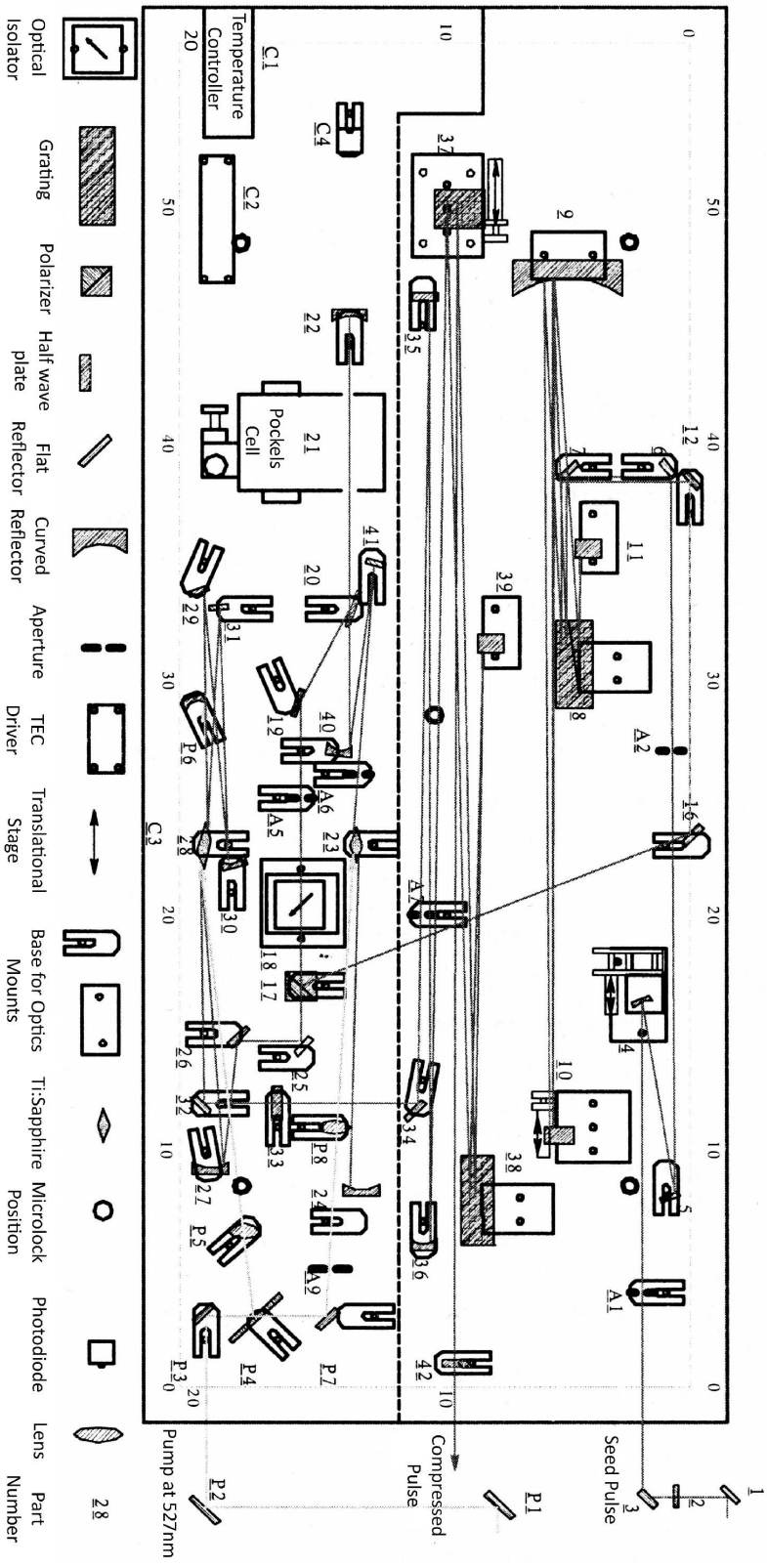

Figure 12: Titan regenerative amplifier schematic[106]

Wavelength selection and optimization of the TOPAS was performed primarily through LabVIEW control and optimization of the input mirrors, but because of alignment problems introduced through thermal drift, an overall alignment of the TOPAS — consisting primarily of optimization of the overlap of each preamplifier pass with the superfluorescence and optimization of the pump overlap with the final preamp pass in the near-field and far-field — was required every one to two weeks.

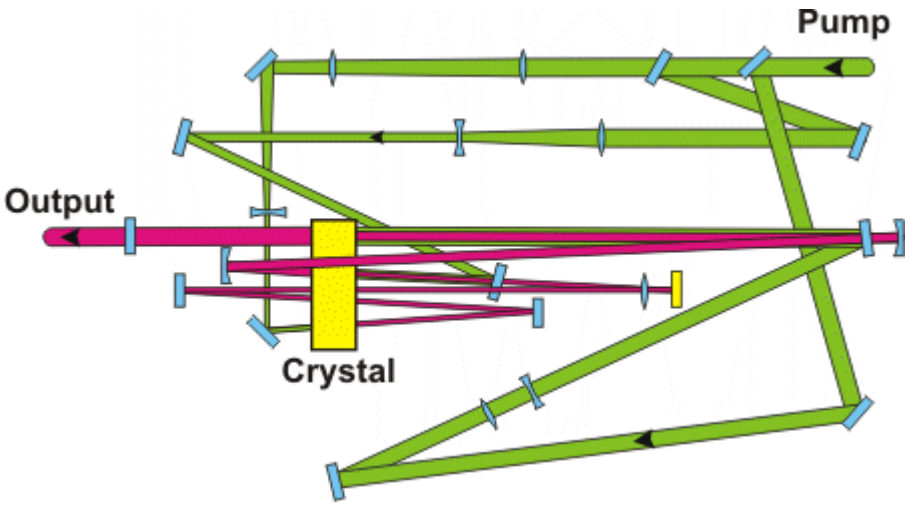

Figure 13: TOPAS schematic[105]

2.8.3 Degenerate pump-probe spectroscopy

A schematic of the setup used for the degenerate 365 nm pump-probe spectroscopy experiment is illustrated by the blue beams in Figure 14. The TOPAS signal was tuned to 1460 nm, resulting in a 365 nm fourth harmonic with 50 μJ per pulse which was used as the pump and probe. Reflective neutral density filters were used to attenuate the pump beam to 1 μJ per pulse, and the probe beam to 40 nJ per pulse at the sample. The pump was determined to be roughly 400 microns in diameter at the sample surface via a razor blade measurement, and the probe beam was roughly 300 microns in

diameter. The probe beam was delayed with a Newport 15 cm linear stage with a bidirectional repeatability of 1.25 μm or 4.17 fs. The step sizes chosen for the degenerate experiments provided 750 fs resolution and 50 fs resolution within 3 ps of the zero-delay. The pump-beam was chopped at 250 Hz, thereby allowing the use of a SRS lock-in-amplifier to increase the signal to noise ratio (not shown in Figure 13). The samples deposited on sapphire allowed for simultaneous measurements of the differential transmission and the differential reflection, necessitating the use of two lock-in amplifiers. The differential signals were normalized against the signal measured while the chopper was placed in the probe beamline. The stage and lock-in amplifier were controlled by LabVIEW.

2.8.4 Broadband pump-probe spectroscopy

Broadband pump-probe spectroscopy is an extension of degenerate pump-probe spectroscopy wherein the probe beam is a supercontinuum rather than the single color used in the degenerate experiment. The probe signal is then read with a spectrometer rather than a photodetector, thereby allowing parallel measurements of the dynamics of multiple modes. This modified probe is illustrated by the output of the delay line in Figure 14. Roughly 100 μJ of the delay line output is focused on a 5 mm thick CaF_2 plate with a 10 cm focal length lens in order to create the UV-visible supercontinuum seen in Figure 15.

The first demonstration of supercontinuum generation by focusing ultrashort laser pulses in transparent media was in borosilicate glass in 1970,[107] and the phenomenon has since been observed in a variety of solids,[108, 109] liquids,[110] and gases.[111] Supercontinuum

generation has generally been described as a result of multi-photon excitation due to self-focusing within the transparent medium. The threshold for continuum generation is well accepted as $E_g/\hbar\omega \geq 2$, and the continuum width increases with $E_g/\hbar\omega$, where E_g is the medium bandgap, and ν is the frequency of the incident radiation. Calcium fluoride (CaF_2) is a commonly used material for supercontinuum generation because of its wide nandgap (10.2 eV), but its damage threshold lies below the threshold for supercontinuum

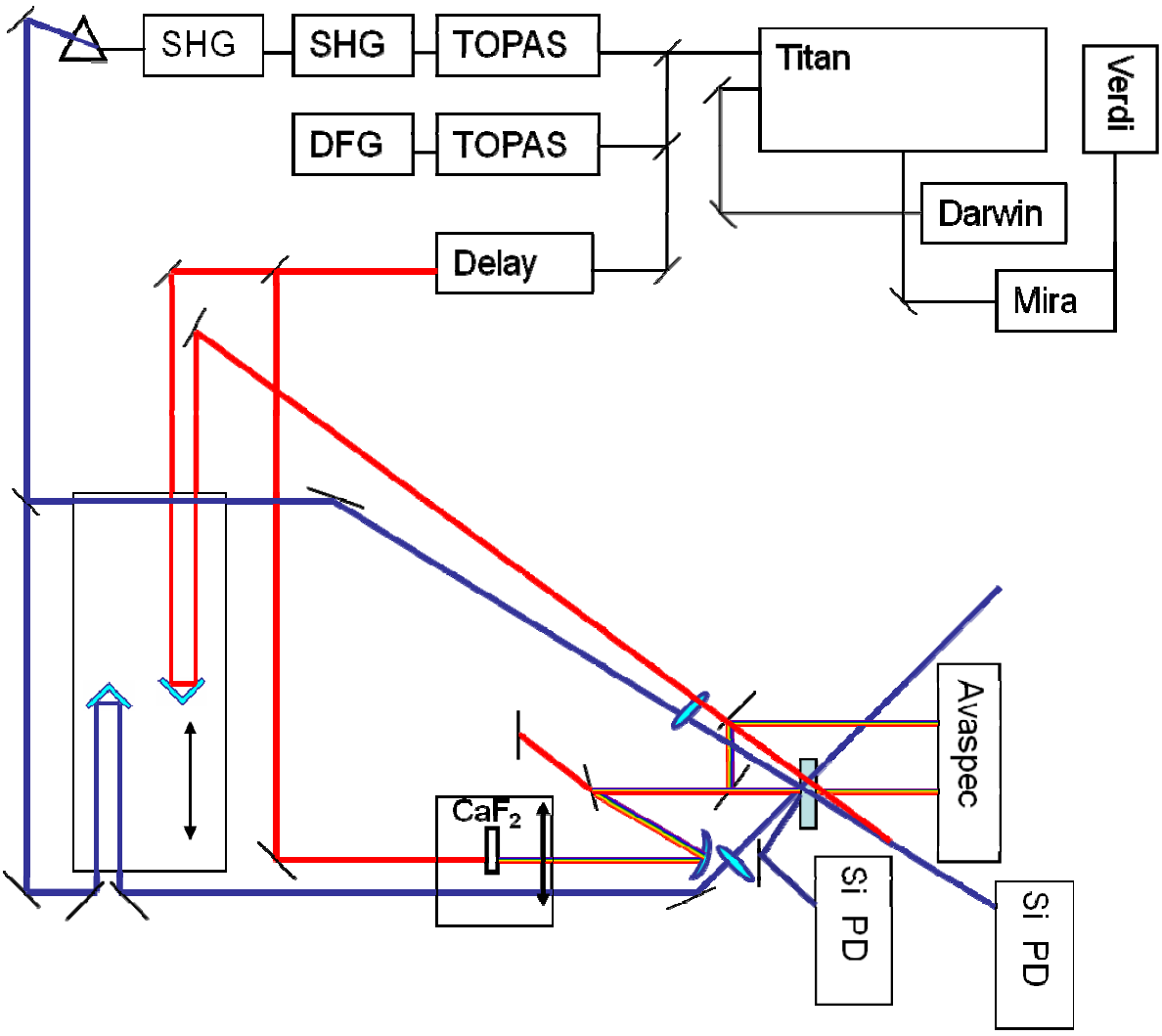

Figure 14: Degenerate pump-probe schematic

generation, so CaF_2 plates must be continuously rotated or translated to avoid damaging the plate.[108] Until recently, most reports had stated that polarization is not conserved in the formation of the supercontinuum in CaF_2, but it is now accepted that the use of a half-wave plate to generate a circularly polarized pump beam, in conjunction with a rotating CaF_2 plate, conserves polarization in the generated supercontinuum with a polarization contrast ratio of at least 10^3 over the entire visible spectrum.[112]

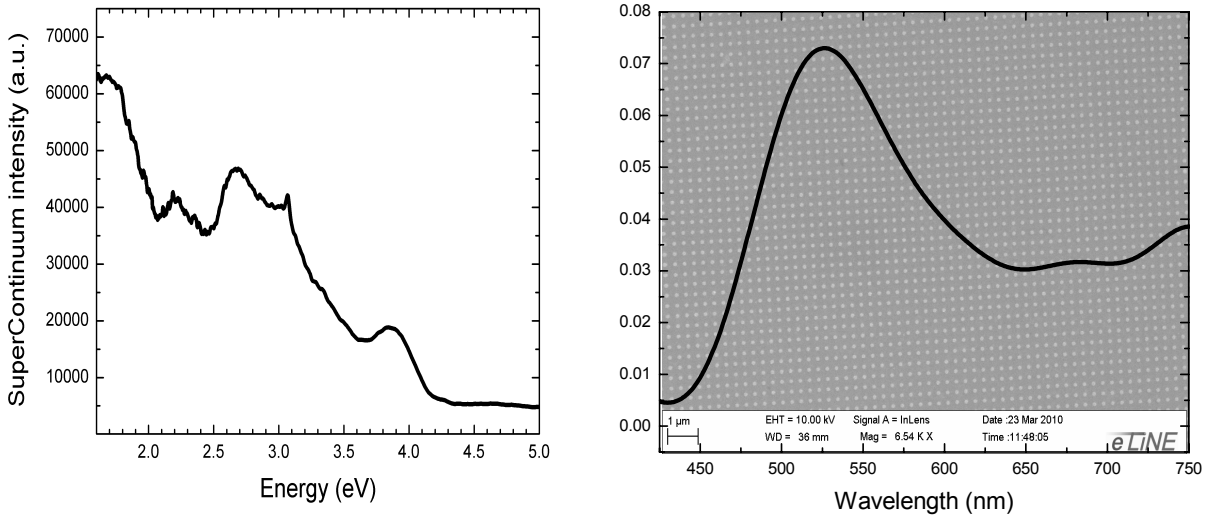

Figure 15: Supercontinuum spectrum generated in 5mm thick CaF_2 plate with 100 µJ, 150 fs, 800 nm seed(left), and absorption spectrum of Au nanoparticle array taken in rebuilt confocal microscope geometry with supercontinuum as a proof of concept.

Unfortunately, while the Titan continues to provide roughly 3.5 W at 800nm, the pulse-to-pulse RMS deviation of 20% at 365 nm (compared with 5% instability under normal conditions) made further experiments which utilize the fourth harmonic or supercontinuum generation impossible. Because the RMS stability of the Titan output power is better than 1.5%, and because the alignment of the TOPAS has been checked many times, it is likely that there is a phase instability in the TITAN output which could

potentially be created by either the Pockels cell or damage to the compression grating. Until the lab acquires the necessary diagnostic tools, it will be very difficult to continue using the TITAN.

CHAPTER 3: ZNO PHOTOLUMINESCENCE ENHANCEMENT BY AG AND AU SPPS AND LSPS

This chapter summarizes the CW photoluminescence results presented in *Optics Express*, *Thin Solid Films*, and *Proceedings of the SPIE* from the Optics and Photonics Conference in 2009, and the results presented in *Physica Status Solidi (c)* in 2011.[113-116] These results center on the ZnO/MgO/metal heterostructures shown in Figure 16, which were designed in order to analyze LSP and SPP interactions with excitons and DAPs in ZnO as the LSP resonance is controlled by the metal composition and film thickness and as the plasmon exciton separation is controlled by the MgO film thickness. In order to differentiate charge-transfer mechanisms from near-field effects, samples with and without MgO thin films were fabricated. The large spectral separation between the ZnO exciton and Au SPPs suggests that band-edge enhancement due to Au SPPs should not be

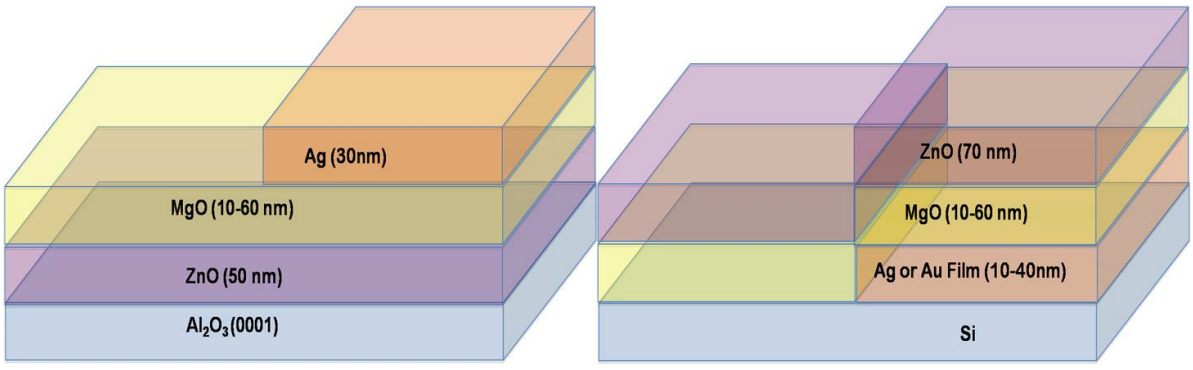

Figure 16: Multilayer heterostructure schematics for Al_2O_3 (left) and Si (right) substrates.

possible, and other authors have reported just that,[69] but we do see small interactions between the Au SPP and the ZnO band-edge exciton which mirror the exciton-Ag SPP interactions.

3.1 Heterostructure design

The results in References 109-111 center on the multilayers grown on Si illustrated in the right of Figure 16. Half of each substrate was masked off before Au and Ag films were deposited with thicknesses of 10 nm to 40 nm in increments of 5 nm. Following the metal deposition, the masks were removed, and MgO films were deposited with thicknesses of 10 nm to 60 nm in increments of 10 nm. The multilayered structures

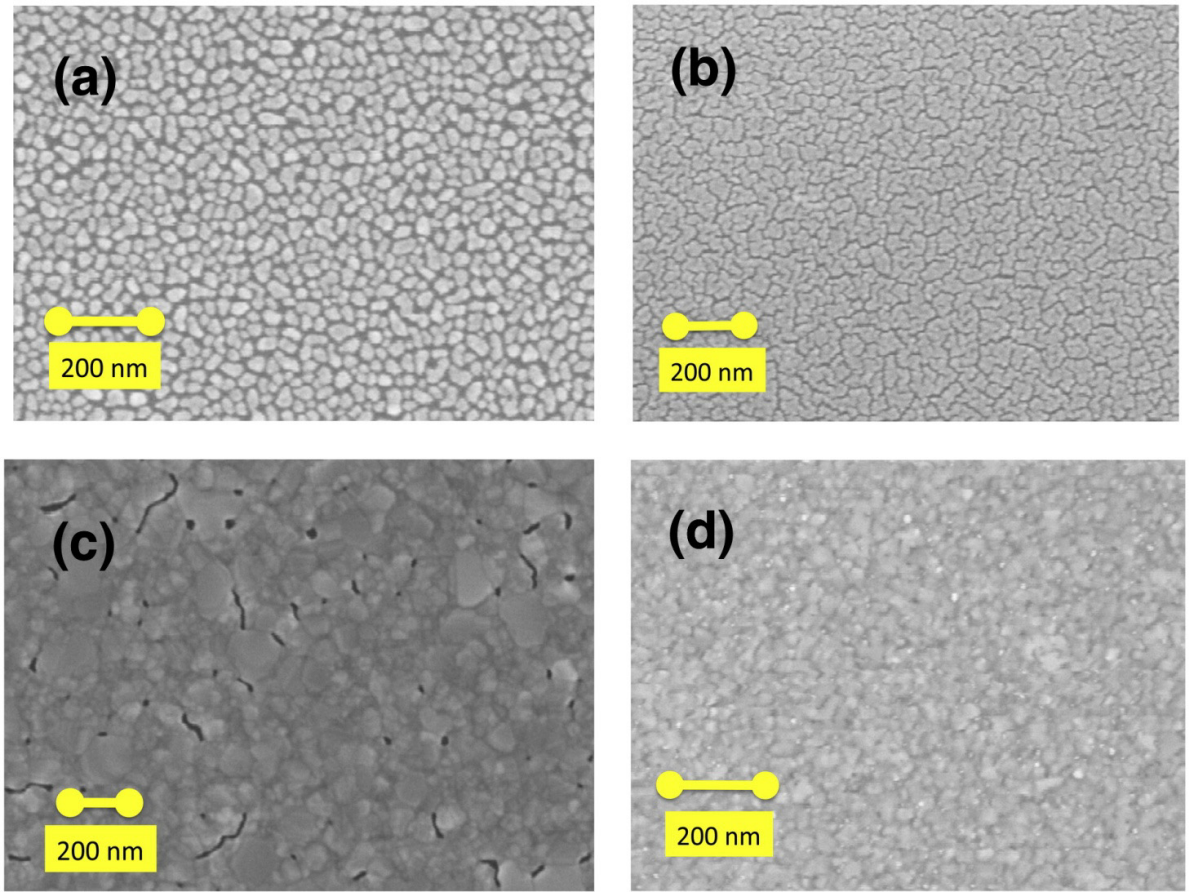

Figure 17: SEM images of a (a) 10nm Ag film, (b) 10nm Au film, (c) 30nm Ag film, (d) 30nm Au film.

were then capped with a 70 nm ZnO film.

Scanning electron microscopy - shown in Figure 17 - demonstrates that the 10 nm metal films are primarily island-like while the 30 nm metal films are quasi-continuous. The island-like nature of the 10 nm films prevents the propagation of SPPs, and the results which are presented in this chapter demonstrate no evidence of SPP interactions for 10 nm metal films. SPPs can be excited on the thicker films both because of the momentum mismatch offered by the rough metal surface, and because of the Otto configuration defined by the sample geometry. On the other hand, LSPs are easily supported on the islands of the 10 nm films and on the local asperities seen in the thicker films. Mie scattering calculations performed using commercial Mie scattering software (MQMie2.4) for nanoparticles with a uniform size distribution 50-150 nm in diameter

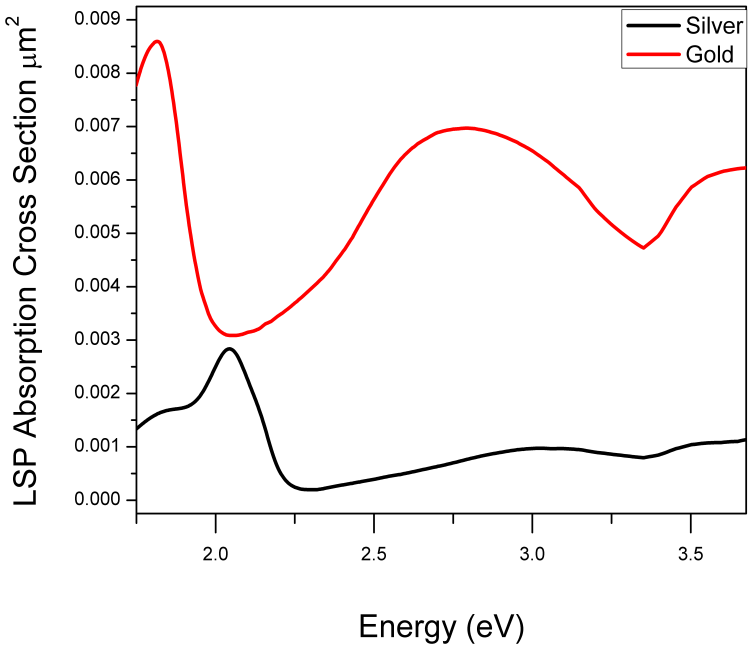

Figure 18: Mie scattering calculation for Ag and Au nanoparticles

demonstrate that the Au LSP resonance is roughly 1.8 eV and the Ag LSP resonance is roughly 2.0 eV. The calculation relied on a simple effective-medium approach which treated the surrounding dielectric as the geometric mean of the Si and MgO dielectric functions. Figure 18 illustrates these results.

MgO has a bandgap of 7.6 eV, which – in concert with the results presented in Figure 11 – indicates that it provides a sufficient barrier to prevent electron transfer between the metal and ZnO films. MgO is a commonly used buffer layer for ZnO growth that reduces the interfacial strain and therefore improves the ZnO optical quality. [117] As a result of this, and because of the slight changes in film quality in each deposition, direct comparison of the photoluminescence spectra between multilayers with different MgO thickness is impossible. Instead, each spectrum may only be compared directly with spectra from multilayers grown under identical parameters. The stoichiometry of the ZnO films was confirmed by Rutherford backscattering spectroscopy (RBS), and the quality of the films is also demonstrated by the ratio of the band-edge emission to the impurity emission in the room temperature PL spectrum presented in Figure 9.

3.2 Varying metal thickness

The peak band-edge emission is enhanced by a factor 2, and the peak DAP emission by a factor 1.5 for Ag and Au films 10 nm in thickness in contact with a 70 nm ZnO film—seen in Figure 19. Multilayers of 10 nm metal, 10 nm MgO, and 70 nm ZnO demonstrate similar enhancement of the DAP emission, but no enhancement of the band-edge emission. Indeed, the MgO heterostructures demonstrate a 50% quenching of the band-edge emission.

Because the enhancement of the DAP emission is near the LSP resonance for both Ag and Au — notable especially in the red-shifting of the Au-MgO-ZnO multilayer PL

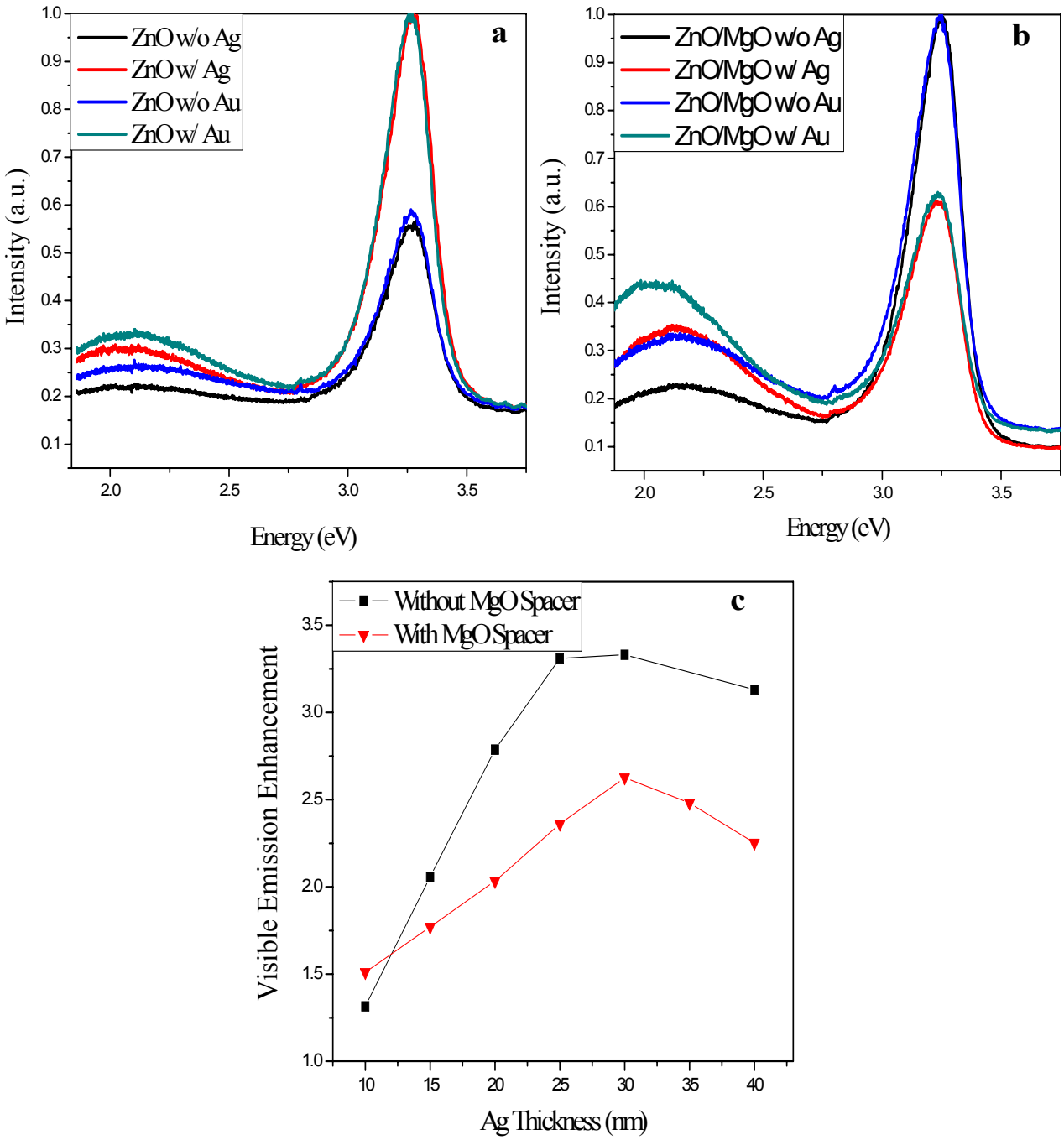

Figure 19: ZnO photoluminescence for 70 nm ZnO thin films in contact (a) with 10 nm metal particulate films, and separated (b) by a 10 nm MgO spacer layer. (c) Ratio of Ag/ZnO visible emission to ZnO visible emission for metal thicknesses of 10 nm to 40 nm.

illustrated in Figure 19b — and because the DAP enhancement exists with and without insulating spacers, the DAP PL enhancement is clearly due to LSP-DAP local field interactions, rather than any charge transfer related effects discussed in section 1.4.1. Furthermore, Figure 11c illustrates that the DAP enhancement is maximized for Ag films 30 nm thick. The same behavior is demonstrated with and without the MgO spacer. This is a clear result of the LSP resonance shifting with increasing Ag thickness: the enhancement should be maximized when the LSP resonance is spectrally nearest the DAP peak. The elimination of the band-edge enhancement upon introduction of the MgO spacer provides clear and significant support to the previously introduced idea of band-edge enhancement by hot-electron transfer from metal nanoparticles to the ZnO conduction band-edge. This is worth emphasizing because the authors of references 54-59 (discussed in section 1.4.1) never isolated the metal nanostructures from the ZnO, making it difficult to separate charge transfer-related mechanisms from near-field mechanisms.

The quenched band-edge PL seen in Figure 19b is a result of decay to the lossy surface waves supported in the Ag and Au Fermi seas described in section 1.4.2. Unfortunately, the rough metal surface which facilitates the excitation of SPPs also provides the necessary momentum mismatch to allow for the decay which would not be seen in exciton-plasmon systems with atomically flat interfaces.[67] The quenching seen in Figure 19b indicates that the PL for heterostructures with no MgO is also damped by excitation of lossy surface waves, but the enhancement resulting from hot electron transfer to the conduction band-edge is sufficiently greater that the damping is not immediately evident. This damping should only be expected for small metal-ZnO

spacing, but it does provide further motivation for the study of the enhancement as a function of separation.

3.3 Varying spacer thickness

In order best to best illustrate the effect of the metal films on the ZnO photoluminescence spectral position and intensity, the ratio of the PL spectra in ZnO/MgO/metal multilayers to the PL spectra in ZnO/MgO multilayers is plotted in Figure 20. 30 nm metal films are used in this section primarily because of the LSP-DAP spectral overlap suggested by Figure 19c. Because the charge transfer interactions are irrelevant for these structures as demonstrated by the absence of enhancement in Figure 19b, all effects described here are a result of exciton and DAP interactions with the SPP evanescent fields and the LSP dipole fields. Figure 20 presents two distinct phenomena. First, the peak enhancement of the DAP emission is seen to occur not at the DAP peak of 2.2-2.3 eV, but at the LSP resonance near 1.8-2.0 eV for Au and Ag respectively. The enhancement of the DAP emission decays monotonically with increasing MgO thickness. Of greater interest here is the behavior of the band-edge photoluminescence. We note that – for both Ag and Au – the band-edge enhancement increases as the MgO thickness increases from 10 nm to 20 nm before quickly diminishing with increasing MgO thickness and demonstrating significant quenching for thicknesses greater than 30 nm. As the band-edge enhancement decays, the peak enhancement red-shifts dramatically to the metal-ZnO SPP resonance for both Ag and Au. Bare metal films 30 nm in thickness, and metal films coated with MgO show no such emission.

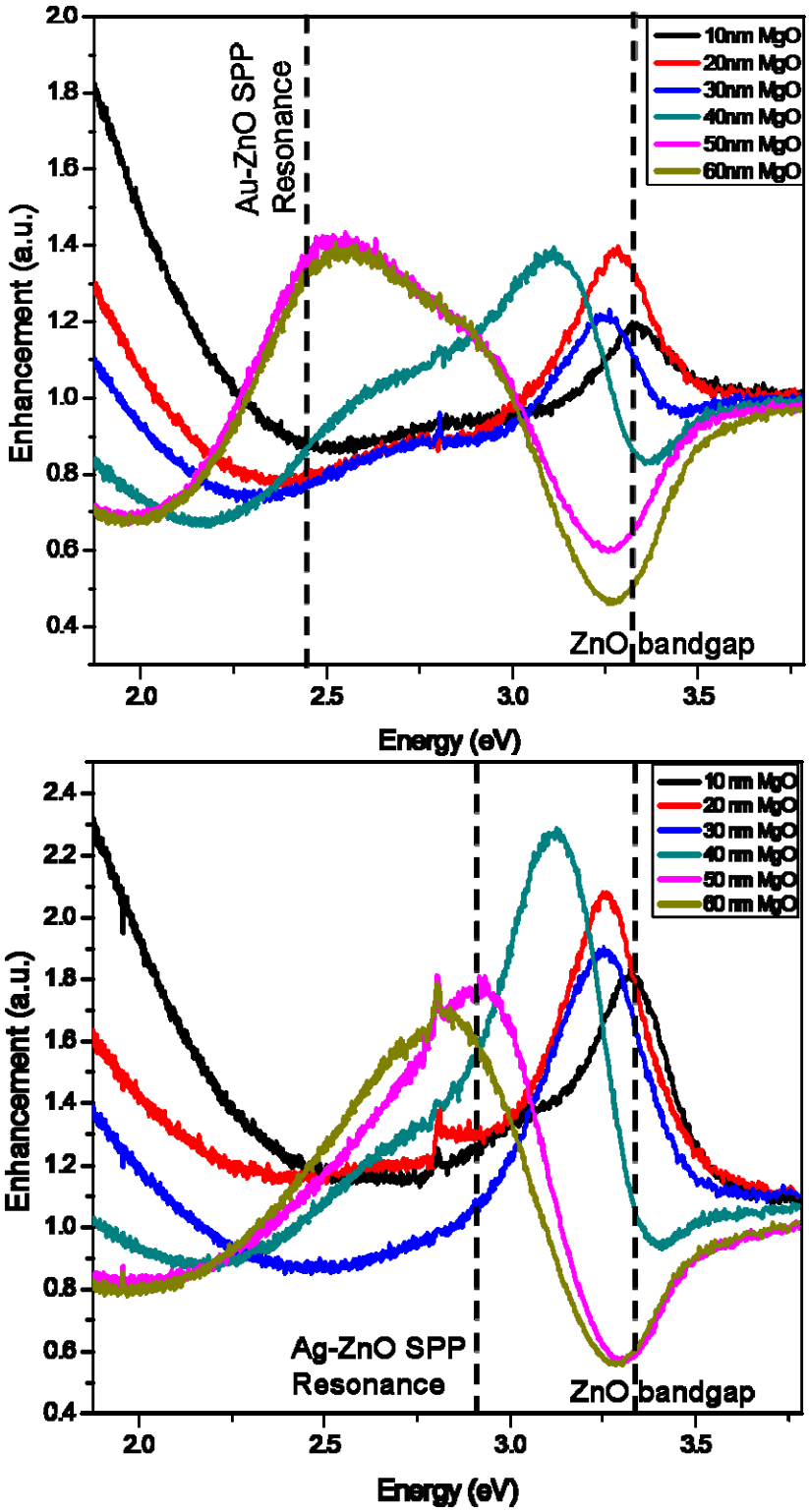

Figure 20: ZnO PL enhancement factor for 70 nm ZnO thin films separated from 30 nm films of Au (a) and Ag (b) by MgO spacers 10 nm to 60 nm in thickness.

The enhancement of the band-edge emission in metal-ZnO bilayer structures has frequently been attributed to Purcell enhancement of the exciton recombination rate, but this is the first report to use MgO spacer layers to analyze the different interaction regimes: namely the theoretically predicted damping by lossy surface waves for spacers of 10 nm or less, Purcell enhancement for spacers of less than or equal to the SPP decay length, and a separate SPP-exciton coupling mechanism for spacers greater than the SPP evanescent decay length. The fact that the enhancement decays to significantly less than unity, coupled with the observed outcoupling at the SPP resonance indicates that Purcell enhancement alone cannot explain the band-edge behavior.

3.3.1 Band-edge enhancement of the ZnO band-edge PL

Equation 1.23 demonstrates that the Purcell enhancement factor should fall off as the square of the evanescent field intensity, so that by combining all other factors into a normalization factor 'A,' we should be able to describe the band-edge emission

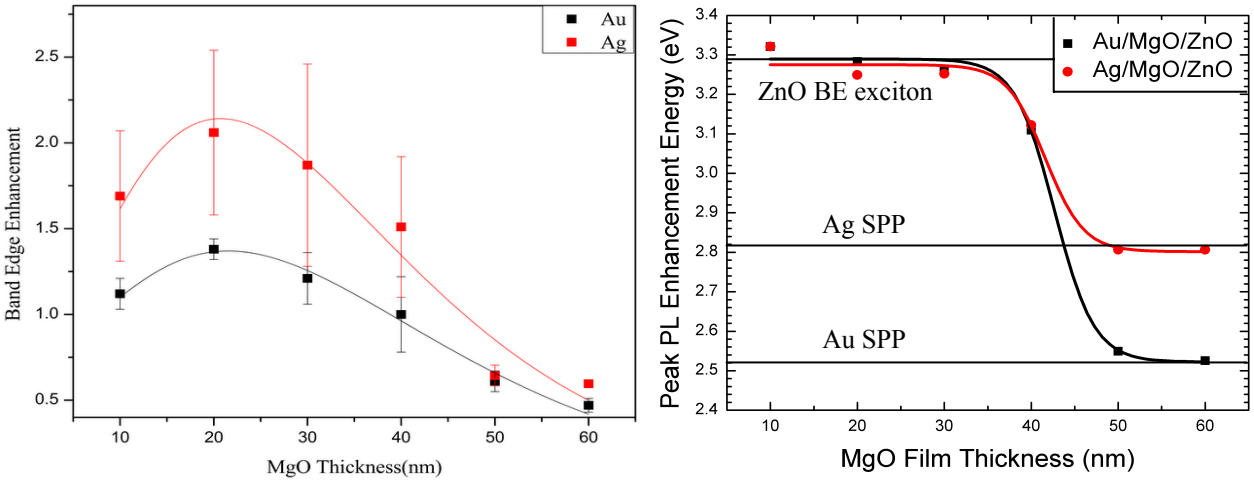

Figure 21: (a) Band-edge enhancement as a function of insulating spacer thickness and (b) the peak band-edge enhancement energy as a function of insulating spacer thickness.

enhancement as $1+Aexp(-2z/\hat{z})$ if these interactions could be described solely as a Purcell effect. However, Figure 20 demonstrates that there is a competing mechanism which quenches the emission for small exciton-plasmon separation. Numerical calculations modeling the decay rate of a dipole near an infinite Ag surface have described the decay to lossy surface waves as increasing quadratically with exciton-plasmon separation, so that for small separation, this damping can quench any Purcell effects.[65] Indeed, the best fit for the band-edge enhancement in Figure 21(a) — which plots the enhancement factor at 3.3 eV for MgO thicknesses of 10-60 nm — is of the form $z^2/A^2e^{-2z/B}+C$. The constant C must be used instead of unity because the outcoupling

	Band Edge Enhancement $E=z^2/A^2e^{-2z/B}+C$		**Visible Enhancement $E=A+B/z$**	
	Au	Ag	Au	Ag
A	8.2±0.3	5.8±0.4	0.59±0.05	0.7±0.1
B	24.6±0.6	22±1	9.8±1	12.5±2
C	.28±.12	.32±.07		
R^2	0.99	0.95	0.96	0.89
Chi^2/DOF	0.002	0.02	0.005	0.02

Table 2: Fit parameters for band-edge and DAP enhancement

into plasmonic modes seen in Figure 20 results in quenching of the band-edge emission for spacers much thicker than the evanescent decay length. This fitting function results in the experimental decay constants shown in table 3.1 which are consistent with the SPP evanescent decay lengths calculated in section 1.3.1, thereby confirming the existence of the Purcell enhancement of ZnO band-edge emission by both Ag and Au SPPs. Figure 21b illustrates the transition of the peak PL enhancement from the ZnO band-edge to the metal-ZnO SPP resonance with a sigmoidal fit to guide the eye. This outcoupling at the

SPP resonance will be discussed in greater detail in the context of the substrate dependence discussed in section 3.4.

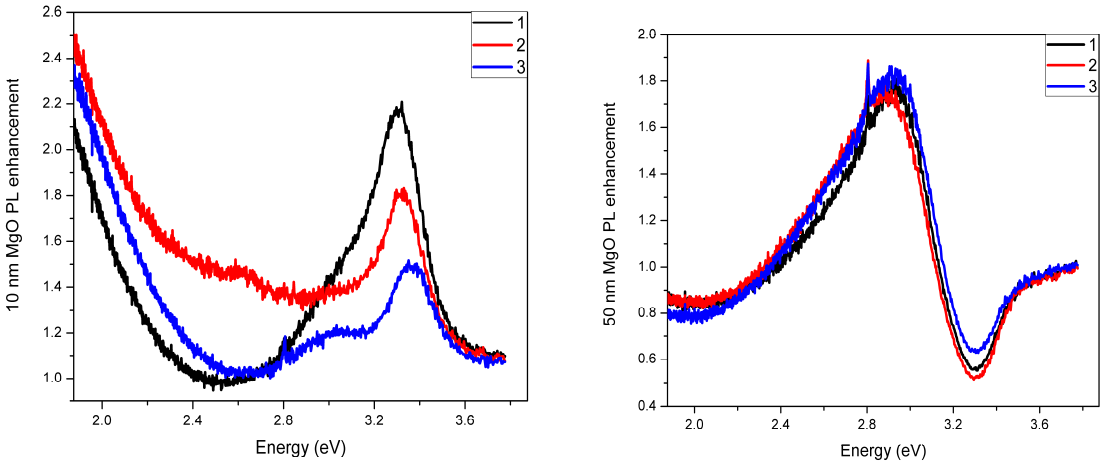

Figure 22: Individual PL enhancement spectra for 10 nm MgO (left) and 50 nm MgO (right): representing the greatest and least variation

While the decay constants in table 3.1 are consistent with the metal evanescent decay lengths, it is disconcerting that the error bars in Figure 21 — calculated from the standard deviation of three identically prepared samples — are as large as they are, especially for the Ag heterostructures. The origin of the error bars is clarified slightly by analysis of the individual spectra. The three spectra that were averaged for the 10 nm MgO heterostructures and the 50 nm MgO heterostructures (the spectra with the greatest and least variation, respectively) are shown in Figure 22. For small MgO spacer layers, there are multiple competing interactions for the band-edge emission: Purcell enhancement by the SPP evanescent waves, quenching into lossy surface waves, and outcoupling into the Ag SPP. The outcoupling into the Ag SPP is relatively small for the 10 nm films, but for the 50 nm films, the MgO is sufficiently thick that the Purcell enhancement and the lossy surface waves are negligible. Because the thicker films do not

suffer from competing interactions, the variation between samples is minimized. On the other hand, because the ability to couple into lossy surface waves is highly dependent on the metal roughness, and because of the multiple possible interactions, the variation in the PL enhancement for the 10 nm MgO heterostructures is much greater. Because absorption by lossy surface waves does not affect the exciton recombination rate, the exciton lifetime studies presented in section 4.1 will provide additional context regarding the Purcell enhancement for small spacer layers.

3.3.2 LSP-DAP dipole-dipole scattering

The peak visible emission enhancement is plotted in Figure 23 as a function of MgO thickness. If the visible emission enhancement were a result of Purcell enhancement of the DAP PL, the enhancement factor would be expected to decay as the square of the LSP dipole field, or as $1/z^6$. On the other hand, if the visible enhancement were a result of LSP-DAP dipole-dipole scattering, then the enhancement factor would be expected to decay as $1/z^{3}$.[118] However, the best fit to the observed visible PL enhancement decay is of the form $A+B/z$. Unsurprisingly, the factor of z^2 which described the decay to lossy surface waves for the band-edge enhancement also describes the damping of the visible enhancement, and the DAP PL enhancement can be understood to be the result of (lossy) LSP-DAP dipole-dipole scattering.

The visible emission is a result of the superposition of the emission from the recombination of conduction band electrons with holes on oxygen interstitials and zinc anti-site vacancies. Therefore, it is difficult to deconvolute the LSP coupling with each state in order to develop a more complete understanding of the LSP-DAP coupling. However, it is worth noting the spike in the PL spectra for the 50 nm MgO

heterostructure in Figure 22. This was originally assumed to be an artifact from the spectrometer, but may in fact be a result of SPP near-field interactions with the DAP composed of the negatively charged zinc interstitial defect and a near valence band-edge hole. This interaction is probed in more detail in Chapter 4.

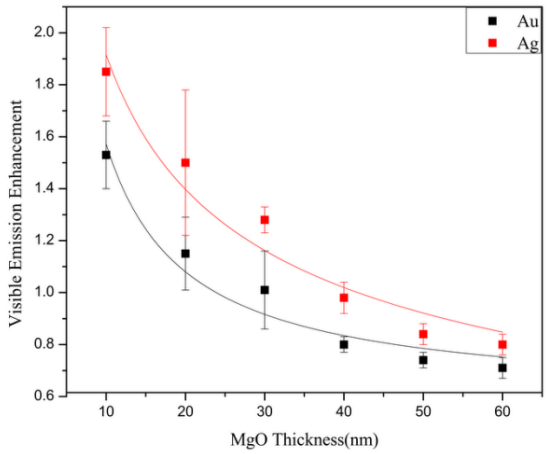

Figure 23: Peak 'green PL' enhancement as a function of MgO thickness.

3.4 Substrate dependence

In order make possible differential transmission pump-probe spectroscopy, and in order to eliminate any concerns about the effect of the metal and MgO layers on the ZnO growth process, the samples illustrated in the left of Figure 16 were grown on (0001) Al_2O_3 substrates. In addition, it was assumed that using the Al_2O_3 substrates would allow us to avoid any substrate dependent quenching which may have been seen in the silicon substrates. Otherwise, it was expected that the PL enhancement for these samples would be similar to that seen in Figure 20 for the heterostructures on Si, so it was a surprise that the spectrally resolved PL enhancement seen in Figure 24 demonstrated no outcoupling at the SPP resonance.

The enhancement demonstrates coupling into lossy surface waves for the 10 nm MgO spacer layer as before, but the peak enhancement for the 20 nm MgO layer is roughly 150% greater than the peak enhancement on a Si substrate, lending support to the belief that the imaginary component of the Si dielectric function is responsible for increased quenching of the ZnO PL.

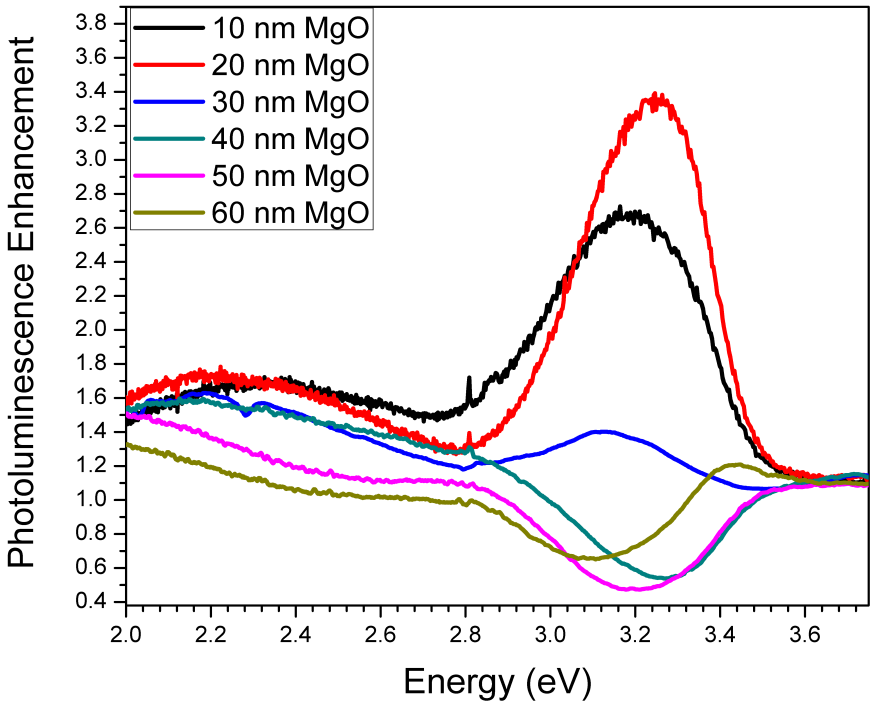

Figure 24: Spectrally resolved PL enhancement for variable MgO thickness on Al_2O_3 substrate

FDTD simulations of Ag/ZnO bilayer structures have demonstrated a significantly reduced enhancement of the ZnO PL for heterostructures on Si substrates compared with those on SiO_2 and Al_2O_3 substrates. The results of the modeling indicate that it is a result of non-radiative coupling into a Si waveguide mode, though no discussion of outcoupling was presented.[71] We therefore conclude that the enhanced emission at the Ag and Au SPP resonances seen in Figure 20 is a result of SPP coupling

into the Si waveguide mode, followed by scattering at the Si/metal interface. The same quenching of the PL seen in the Si-based structures is seen in the Al_2O_3-based structures because the energy-transfer process to the SPP from the exciton, due to strong field localization near the metal interface, is the same. However, while the SPP modes are leaky, the absence of an efficient outcoupling path such as the Si waveguide mode results in the damping of the SPP and no observed emission.

CHAPTER 4: PLASMONIC CONTROL OF ZNO DYNAMICS

Because of the multiple interactions seen in the PL enhancement in chapter 3, it was imperative to examine the exciton dynamics as a complementary tool to describe the exciton-plasmon coupling. Section 4.1 is based on the portions of references 109 and 112 that reported on the coupling dynamics of the Si heterostructures whose energetics were described in section 3.3.[113, 116] The various phenomena seen in the pump–probe spectra of the silicon heterostructures resulted in the decision to fabricate the Al_2O_3 heterostructures discussed in section 3.4 in order to allow for the analysis of both the transient reflection and the transient transmission. The analysis of those spectra, reported in section 4.2, motivated the study of similar Ag/MgO/ZnO heterostructures that utilized ZnO thin films annealed under various conditions. The transmission and reflection pump-probe spectroscopy and photoluminescence spectroscopy performed on the annealed structures, particularly the results which demonstrate the Purcell enhancement of a Zn interstitial DAP state, are reported in section 4.3, and are being prepared for submission to Applied Physics Letters.

4.1 Degenerate pump-probe spectroscopy on silicon substrates

The coupling dynamics were analyzed by degenerate pump-probe spectroscopy using the 150 fs, 365 nm TOPAS output described in section 2.8.3. The pump fluence of roughly 600 $\mu J/cm^2$ produced no signal from the Si and Al_2O_3 substrates, and a barely measureable signal from the Ag thin films deposited on Si characterized by a sub-ps decay with the maximum $\Delta R/R$ nearly two orders of magnitude smaller than that seen in

ZnO. On the other hand, the transient reflectivity of the Au-ZnO heterostructures seemed to exhibit large non-radiative absorption by the Au films which precluded useful analysis of the Au heterostructures by this approach.

The pump-probe spectra for the Ag heterostructures on Si that were discussed in section 3.3 are illustrated in Figure 25 for MgO thicknesses of 10 – 60 nm. The short (10 – 20 ps) lifetime for ZnO films grown on 10 - 20 nm MgO films was common to every such MgO/ZnO bilayer just as every 50 – 60 nm MgO thickness heterostructure demonstrated a longer lifetime of 60-70 ps. While the heterostructures with less than 50 nm MgO demonstrated rise-times of 200-500 fs that then decayed with a lifetime of 10s of picoseconds, the 50 nm and 60 nm MgO heterostructures demonstrated a prominent coherence peak at the zero-time-delay with a rise time of roughly 500 fs which then decayed within 300 fs before increasing to the maximum differential reflection within 3-4 ps, as shown in greater detail in Figure 26 for the 50 nm MgO heterostructure. Because the thicker MgO spacer layers provide more effective strain relaxation in the ZnO film, the exciton decoherence time is longer than the overlap of the pump and probe beams, enabling the observation of coherent interactions between the probe and the ZnO exciton.[119-121]

This behavior is not seen in the Ag-heterostructures, probably because of increased scattering from the Ag surface. Notably, the Ag-heterostructures with MgO thicknesses of 40-60 nm demonstrate a long-lifetime component of greater than 200ps that suggests the formation of either deep impurity states in ZnO or an increased fraction of states that undergo radiative recombination(as discussed in chapter 1, both transitions have lifetimes of between several hundred ps and a few ns). Because the defect PL

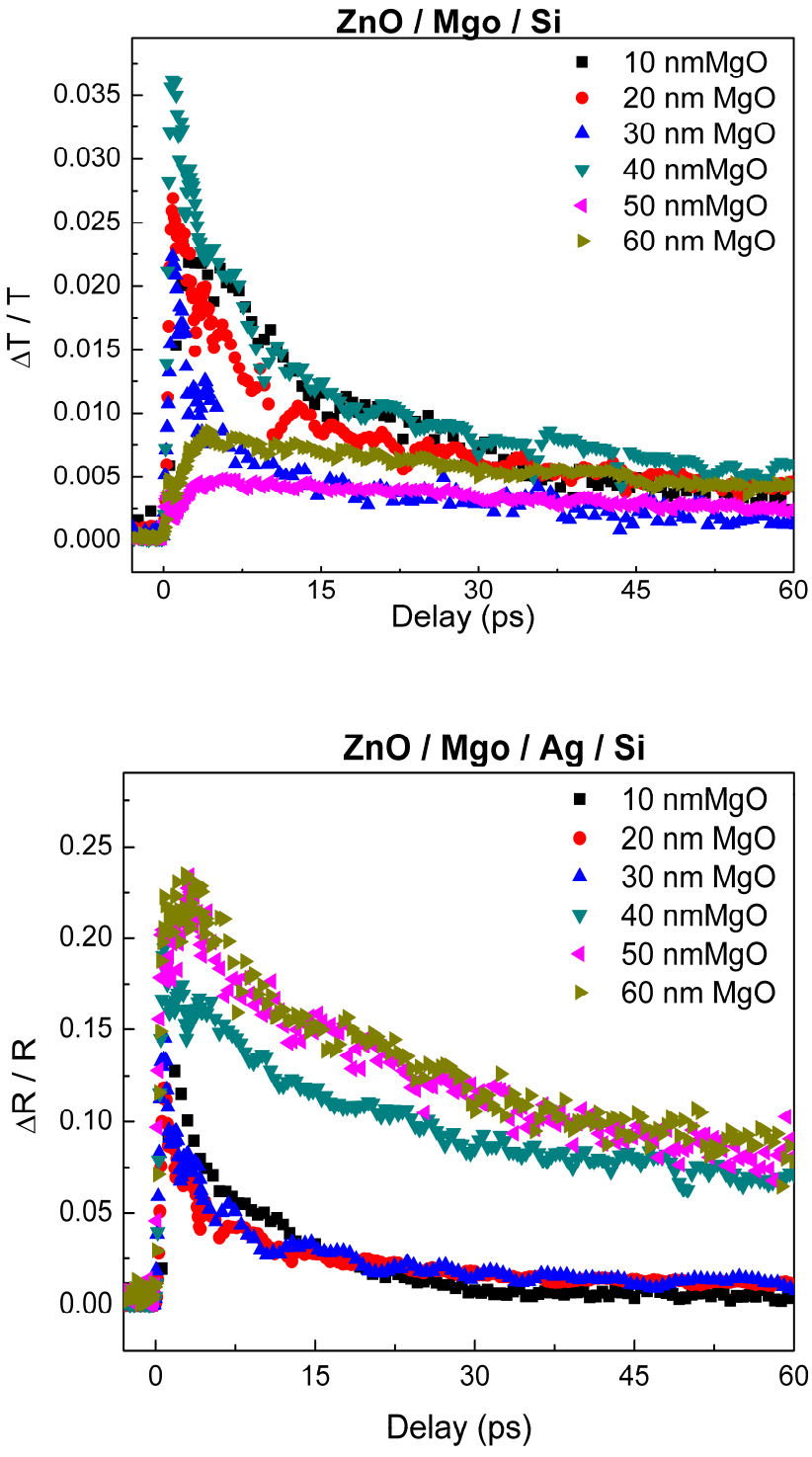

Figure 25: Degenerate 365 nm pump-probe spectra for ZnO/MgO/Si (top) and ZnO/MgO/Ag/Si (bottom) heterostructures for MgO thicknesses of 10 – 60 nm.

intensity is roughly unchanged by the Ag films for these heterostructures, and because the band-edge PL is quenched through SPP excitation, it is difficult to determine what caused the long-lifetime component, but future broadband-pump-probe experiments would be worthwhile to complete this investigation.

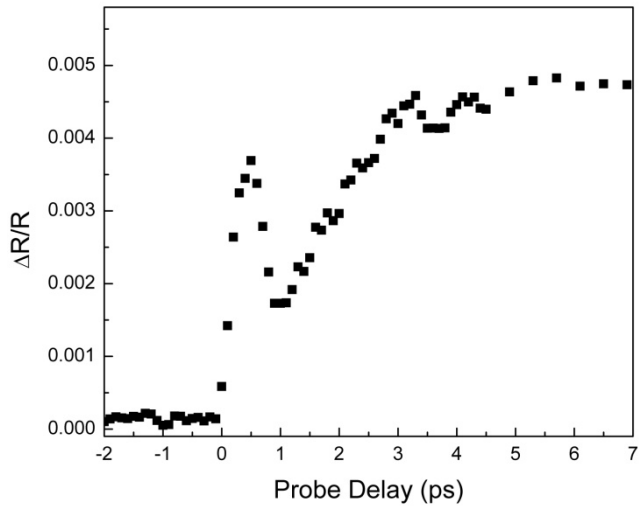

Figure 26: Differential reflection spectrum for heterostructure with 50 nm MgO on Si near the zero-delay

While we have not pursued the dependence of the ZnO dynamics on the MgO thickness any further, the coherence spike and the subsequent long-lifetime results are consistent with the report from Wang *et. al.* which used PL spectroscopy and XRD to demonstrate improved ZnO film quality for films grown with MgO buffer layers on Al_2O_3 substrates.[117] The improved optical quality in that case was attributed to strain reduction by the rough MgO buffer layer. Presumably, the longer recombination time seen in the thicker MgO heterostructures is a result of increased radiative recombination within the ZnO thin film.

The decay dynamics for the heterostructures with and without Ag films were modeled using double exponential decays — as suggested in section 1.1.1 — with effective recombination rates given by $\Gamma_{metal/ZnO} = \Gamma_{mt} + \Gamma_{mr}$ and $\Gamma_{ZnO} = \Gamma_t + \Gamma_r$ respectively where Γ_t and Γ_{mt} describe the exciton thermalization, and Γ_r and Γ_{mr} describe the exciton recombination.[17-19, 122]

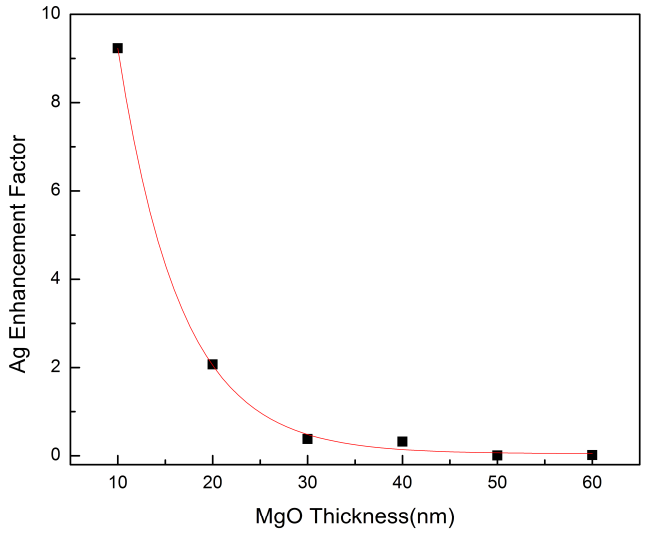

Figure 27: The approximate radiative decay rate enhancement of ZnO films near Ag films as a function of metal-ZnO separation.

We can approximate the ratio of the effective recombination rates as equivalent to the Purcell enhancement factor observed in the band-edge PL in chapter 3.[123] In Figure 27, this enhancement factor is plotted as a function of MgO thickness for the ZnO/MgO/Ag multilayers. The red line is an exponential curve fit with decay constant of 14 nm, which is roughly consistent with the calculated 21.3 nm Ag SPP evanescent decay length. However, the Purcell enhancement should decay to unity as the separation increases past the SPP decay length, while the curve in Figure 15 demonstrates quenching at large MgO thicknesses, similar to the quenching seen in the PL results from chapter 3.

This suggests that the quenching seen for small MgO spacer layers is a result of absorption due to lossy surface waves in Ag, and therefore does not affect the recombination rate. On the other hand, the quenching for large MgO spacers, which we attributed to energy transfer into SPP modes, is not simply a result of SPPs excited by excitonic emission, but is rather a result of a weak coupling between the exciton and the SPP, which in turn reduces the exciton recombination rate.

4.2 Simultaneous reflection and transmission pump-probe spectroscopy on sapphire substrates

The Ag/MgO/ZnO heterostructures described in chapter 3 and illustrated in the left of Figure 16 were designed to allow for pump-probe spectroscopy in both reflection and transmission. Unfortunately, shortly after the samples were prepared, the Nd:YLF pump laser for the Titan (see Figure 14) flooded due to mechanical failure of thin-walled brass fittings on the water coolant system. The repair process took slightly more than 2 months, so the transient transmission and reflection spectra included in this section were acquired using the Ag/MgO/ZnO heterostructures roughly 2.5 months after they were first fabricated. While the PL spectra appear unchanged, it is possible that these samples may have degraded between fabrication and spectroscopy.

In order to ensure that we were examining ZnO dynamics rather than Ag dynamics, the sample was oriented in the back orientation illustrated in the left of Figure 28 so that the pump and probe beams entered through the substrate. Given the 300-400 micron spot size for the probe and pump beams, it is safe to conclude that the differential transmission spectra probed the entire thickness of the film as a result of spatial overlap of the pump and probe throughout the heterostructure. Because of the general lack of

information about the Ag coated ZnO exciton dynamics provided by differential reflection spectra in the front orientation, the spectra discussed in this section were acquired in the back orientation, but the distinction between the dynamics at the MgO/ZnO interface and at the ZnO/ Al_2O_3 interface will become important in the next section.

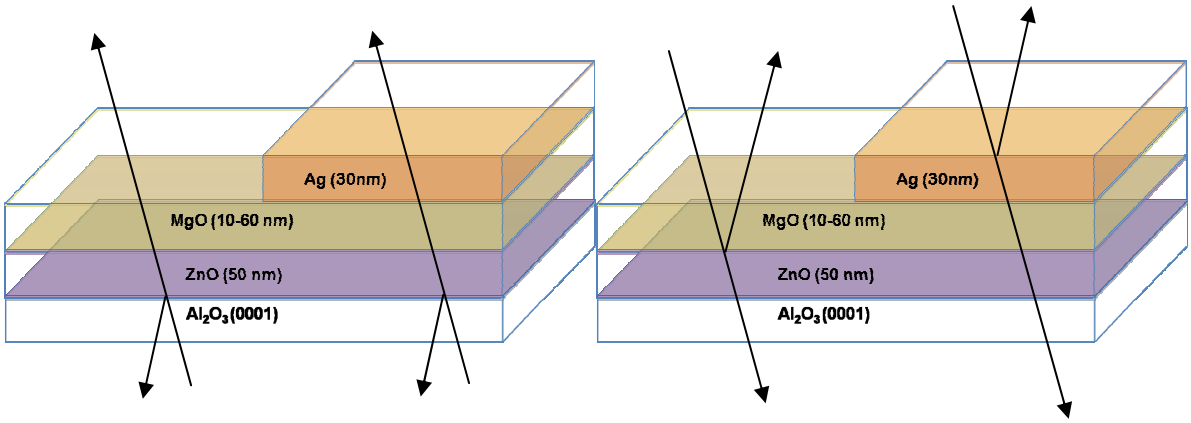

Figure 28: Schematic illustrating the configuration for differential reflection and transmission spectroscopies in a back orientation (left) and a front orientation (right).

Figure 30 illustrates the differential reflection and transmission for the ZnO/MgO bilayers acquired in a back orientation, and Figure 31 illustrates the same spectra for the Ag coated heterostructures. In both the metal-coated and the uncoated heterostructures, the differential transmission spectra look similar to the differential transmission spectra described in section 1.1.1, but the differential *reflection* spectra, particularly the spectra for the uncoated bilayers, look markedly different. Indeed, a comparison of the differential reflection spectra for the uncoated bilayers and the PL spectra for the uncoated bilayers (also acquired in a back orientation) shown in Figure 29 demonstrate a clear correlation between the magnitude of the differential reflection after the initial sub-ps decay, and the magnitude of the PL.

The significant difference between the differential reflection and the differential transmission spectra suggests that the differential reflection spectroscopy is only probing a relatively small volume of the thin film. Further, the fact that the PL intensity mirrors the differential reflectivity so well suggests that the bulk of the PL intensity is due to emission from the near-surface states which contribute to the reflection spectrum.

This understanding of the difference between the differential reflection and transmission spectra provides the necessary context to explain the disparities between the uncoated ZnO differential reflection spectra for the Si and Al_2O_3 substrates. Spectroscopy performed on the Si substrates was probing the ZnO/air interface, while the spectra in these measurements are derived from the ZnO/Al_2O_3 interface. Although the dynamics of the excitons supported near the ZnO/air interface on the Si substrates are as

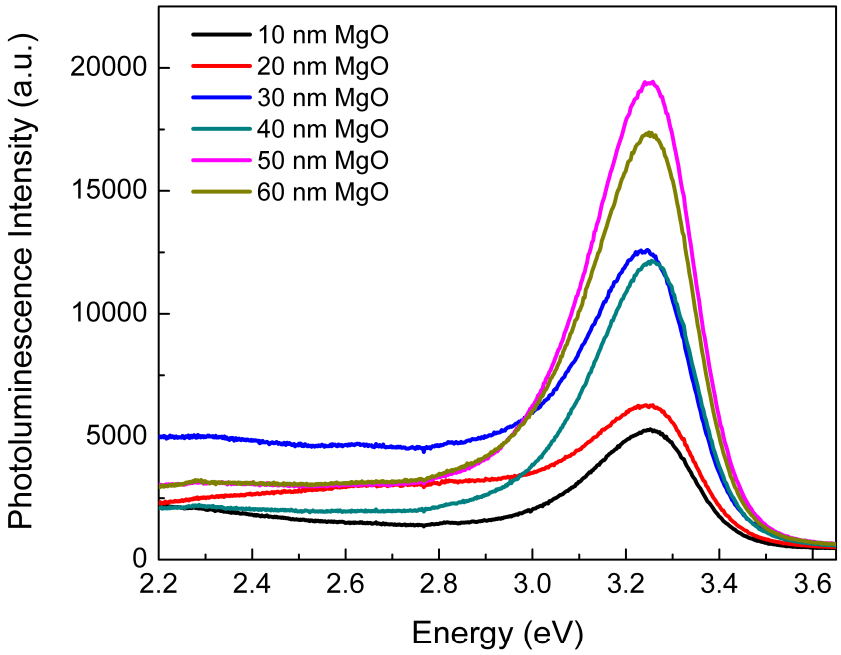

Figure 29: PL of Al2O3/ZnO/MgO multilayers as a function of MgO thickness

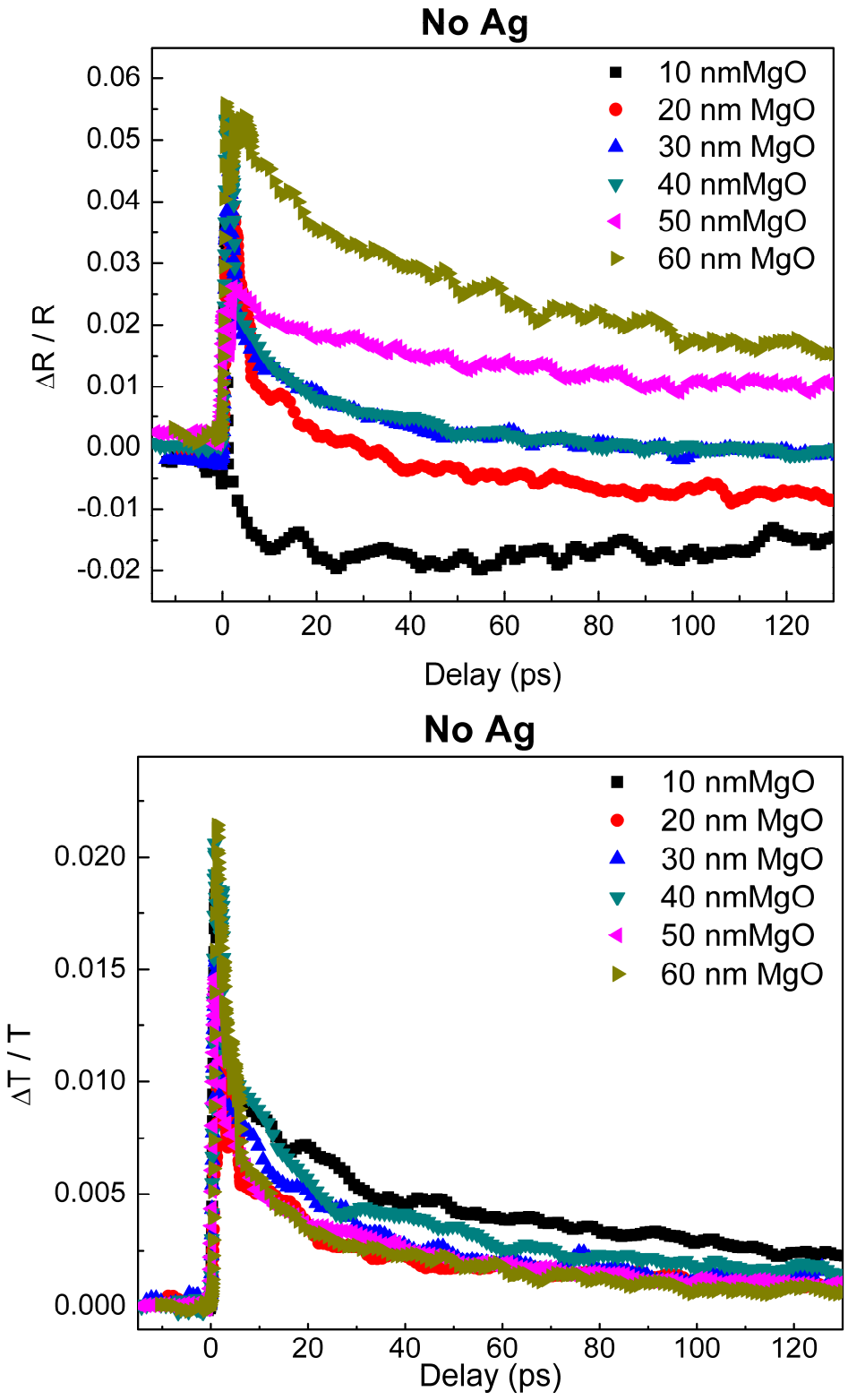

Figure 30: Differential reflection (top) and transmission(bottom) for ZnO/MgO with variable MgO thickness.

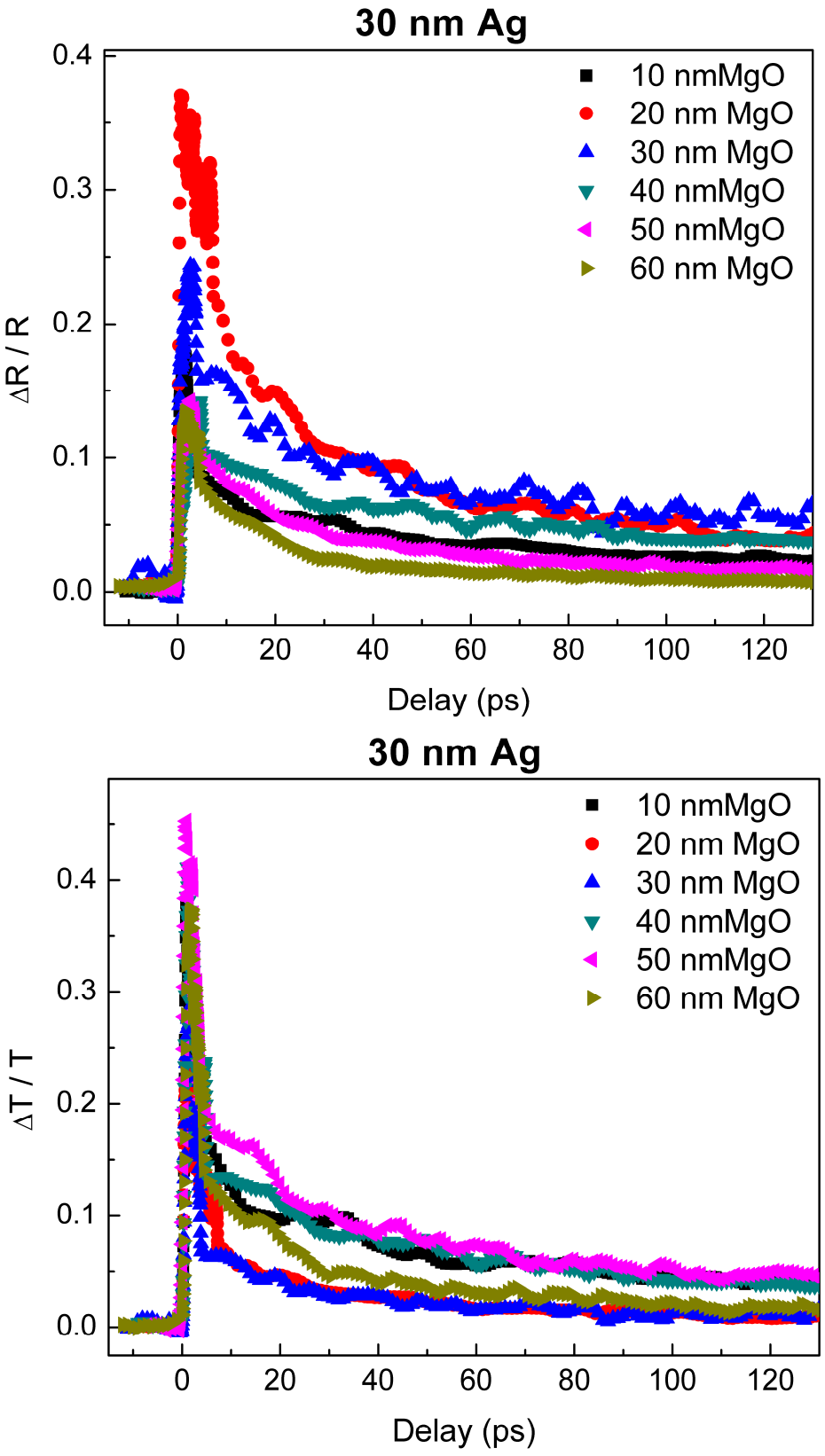

Figure 31: Differential reflection and transmission for ZnO/MgO/Ag with variable MgO thickness.

described in the literature, excitons supported near the ZnO/Al_2O_3 interface demonstrate markedly different behavior. This can be attributed mostly to the significant strain at the ZnO/Al_2O_3 interface due to the 19% lattice mismatch discussed in section 2.1.

The analysis presented thus far does not explain the variation in the differential reflectivity as a function of MgO thickness. Presuming that the gross majority of the differential reflection signal originates at the ZnO/Al_2O_3 interface (as must be the case given the difference between differential reflection and differential transmission spectra), one would not expect to see a dependence on the MgO thickness. However, in this case, the dependence on film thickness may have less to do with the MgO thickness than with the deposition procedure. After all of the ZnO films were deposited simultaneously, the MgO films were deposited beginning with the 10 nm MgO heterostructure, and concluding with the 60 nm MgO structure.

Therefore, while the 10 nm MgO structures were placed immediately back in the evaporator after the ZnO deposition, the 60 nm MgO structures were at atmosphere for roughly 2 days before MgO deposition. Moreover, because the evaporator chamber was unused for more than a month prior to these depositions, the base vacuum in the chamber dropped from $5*10^{-6}$ Torr to $8*10^{-7}$ Torr between the first deposition and the last. The differences in the dynamics are therefore likely a result of the several variable conditions each sample was exposed to during fabrication.

However, the significance of these results lies in the difference between the differential reflection spectra for metal-coated and uncoated heterostructures. The 600 fs decay constant seen in the 10 nm MgO heterostructure suggests a radiative decay of conduction band electrons to deep electron acceptors, followed by a slow recombination

process. In contrast, the much slower decay process seen in the 50 nm and 60 nm films suggests that the number of excitons undergoing radiative recombination relative to those undergoing non-radiative recombination has increased dramatically—given the much longer lifetimes expected from the literature for radiative decay. [17-21] However, the Ag coated heterostructures demonstrated no such distinctions. Indeed, the Ag structures can be fit well by double exponentials with appropriate decay constants as was done previously. This suggests that while Purcell enhancement increases the radiative recombination rate in all of the structures as expected, the increased recombination rate is sufficient that the 10 nm MgO structures demonstrate none of the decay to impurity states seen in the uncoated structures. Unfortunately, as seen in chapter 3, the significant leakage to lossy surface waves prevents a large PL enhancement from being observed despite the dramatic change in exciton dynamics.

A final observation of note regards the difference in the magnitude of the differential reflectivity for the Ag coated heterostructures compared with the uncoated heterostructures. The Ag coated samples demonstrate increased peak differential reflectivity by a factor of between 2.5 and 9, and increased peak differential transmission by a factor of up to 25. This can easily be attributed to increased absorption of the pump pulse due to plasmonic near-field localization as discussed in section 1.4.3. The increased absorption results in a greater band-edge electron population and therefore a greater peak differential reflection and transmission.

4.3 Impurity dynamics

In an effort to develop a better understanding of the various decay dynamics in ZnO thin films, and to investigate the possible control of these defect-states by LSPs or

SPPs, ZnO thin films were annealed in O_2 and in atmosphere prior to Ag deposition. Rather than focusing on the distance dependence of the plasmon-exciton interactions, this section probes the dependence on annealing conditions, in an attempt to control the impurity populations.

4.3.1 Annealing procedure

Because of the concerns mentioned in the previous section regarding the possibility of sample degradation prior to MgO deposition, two possible Al_2O_3/ZnO/MgO/Ag heterostructures were investigated: those where the ZnO was annealed and then coated with 10 nm MgO and 30 nm Ag, and those where the ZnO/MgO was fabricated by e-beam evaporation and then annealed prior to Ag deposition. In addition, in an attempt to control the defect-state population, the annealing was performed in either an O_2 flow of 9.8 ccm or in atmosphere. Annealing at temperatures of 200-800°C prevented the possibility of depositing all three layers prior to annealing, as the 30 nm Ag films would quickly form islands and therefore prevent the propagation of SPPs.

The PL spectra for a representative subset of the annealed ZnO/MgO bilayers are shown in Figure 32. In each case, the ZnO films that were annealed prior to MgO deposition were placed in a portable desiccator immediately after annealing and transported directly to Fisk University for electron-beam evaporation of the 10 nm MgO film. The bilayers in which the MgO was deposited prior to annealing were placed in a desiccator immediately after annealing, and all samples were then partially coated with 30 nm Ag.

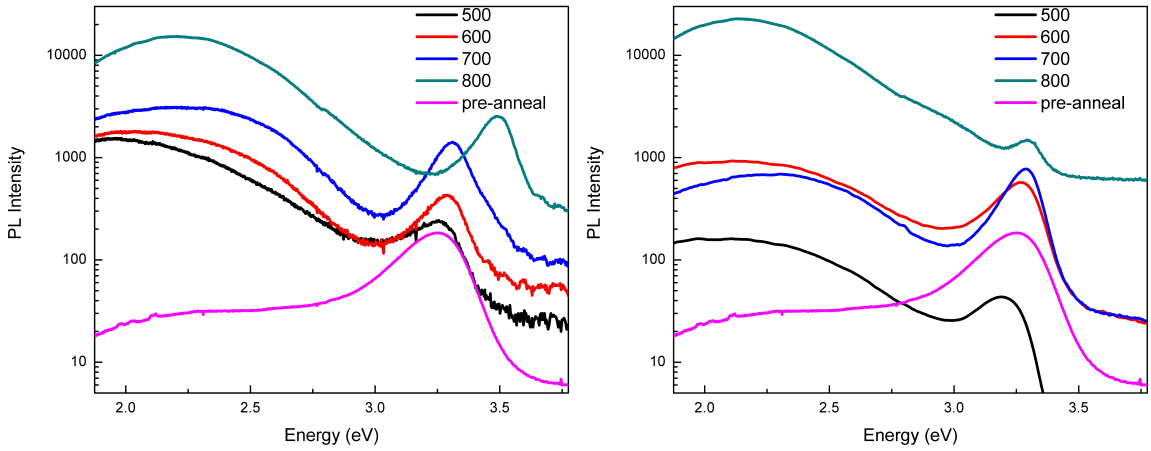

Figure 32: PL for ZnO/MgO bilayers annealed prior to (right) or after (left) MgO deposition at temperatures of 500-800°C

The PL spectra for both sets of annealed samples demonstrate two to three orders of magnitude greater impurity PL intensity in addition to a less dramatic increase in the band-edge PL intensity (or a decrease in the band-edge PL in the case of the sample annealed at 500°C). The most notable result in Figure 32 is the blue-shifted band-edge emission for the ZnO/MgO bilayer annealed at 800°C, which is clearly a result of the formation of $Zn_{1-x}Mg_xO$. Because these PL spectra were all taken in a back orientation, and because of the previously developed conclusion that the PL is probing only the near-interface states, it is reasonable to assume that the 800°C anneal resulted in the formation of the [Zn,Mg]O alloy throughout the entire thin film. While the 3.49 eV bandgap suggests 5.3% Mg composition near the substrate, the Mg composition may be greater closer to the MgO interface. It is also worth noting that the 700°C anneal resulted in slight blue-shift of 60meV, suggesting ~1% Mg content near the Al_2O_3 interface.

4.3.2 Ultrafast results on annealed samples

Examination of the differential reflection spectra in Figures 33 and 34 obtained in backward and forward orientations for the heterostructures where the MgO was deposited

after the ZnO was annealed demonstrates a readily apparent difference. While the backward orientation demonstrates a clear dependence on annealing temperature, no such dependence is apparent in the forward orientation. This is very likely because — despite every care being taken to keep the surface clean and despite depositing MgO as soon as possible — any metastable impurity sites on the ZnO surface which was exposed to air reacted with the air prior to the MgO deposition.

The valence-band offset and conduction-band offset for ZnO/MgO heterojunctions are well characterized experimentally[124] and theoretically[125, 126]: the valence band offset is given experimentally by 0.87 ± 0.2 eV, and the conduction band offset is roughly -3.59 ± 0.2 eV. Therefore, we can safely conclude that the 365 nm pump and probe beams were insufficient to result in significant charge transfer at the ZnO/MgO interface.

The samples annealed at 400°C and 500°C demonstrate a dramatically smaller peak differential reflectance in the back orientation than the samples annealed at higher temperatures (though as the inset demonstrates, they still demonstrate the formation of a clearly defined long-lived state). The weak band-edge PL intensity for these samples suggests that they are forming long-lived defect-states rather than decaying by enhanced radiative recombination, though without access to techniques such as electron paramagnetic resonance spectroscopy, it is difficult to identify the nature of these defect-states.

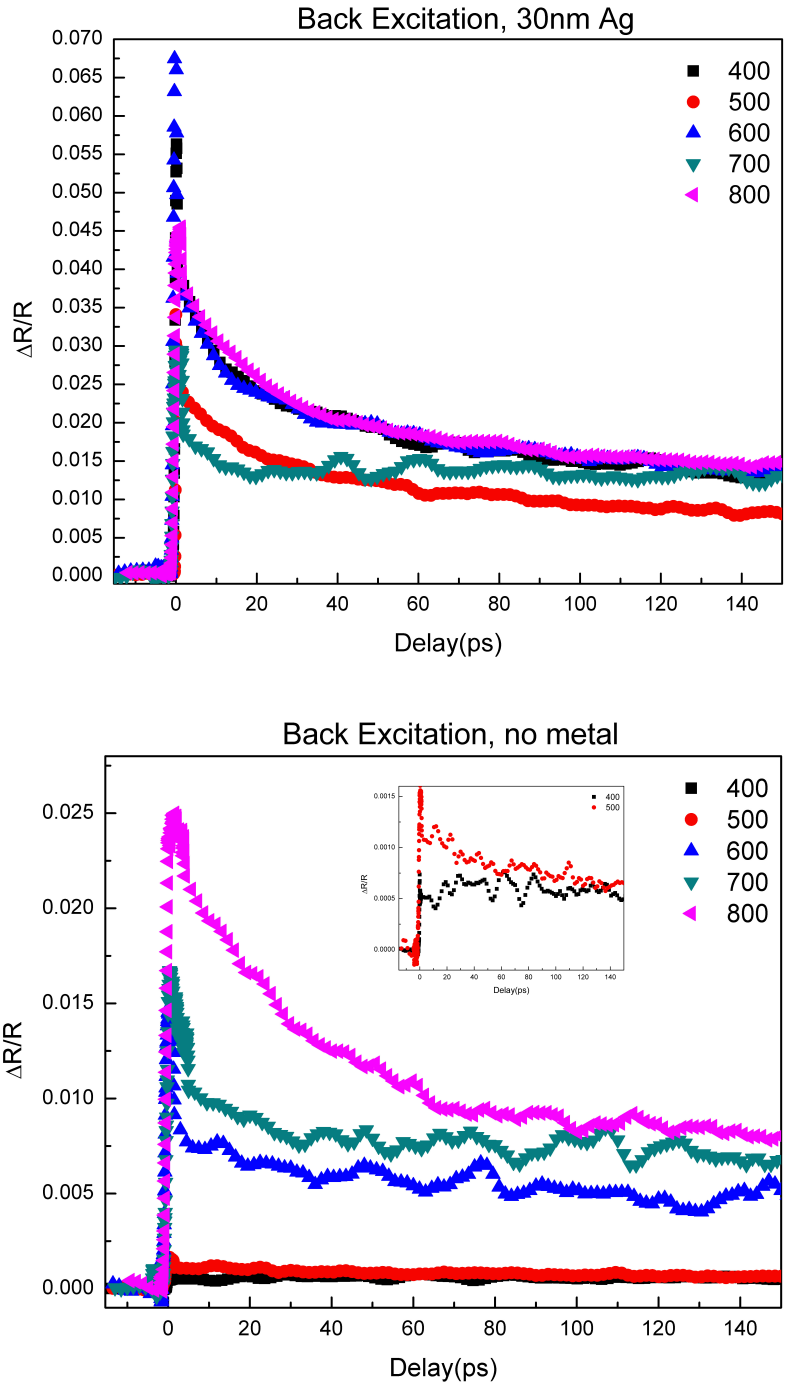

Figure 33: Differential reflection spectra acquired in a back-orientation for Ag coated and uncoated heterostructures annealed prior to MgO deposition at temperatures of 400-800C. The spectra for 400 and 500C are blown up in the inset for clarity.

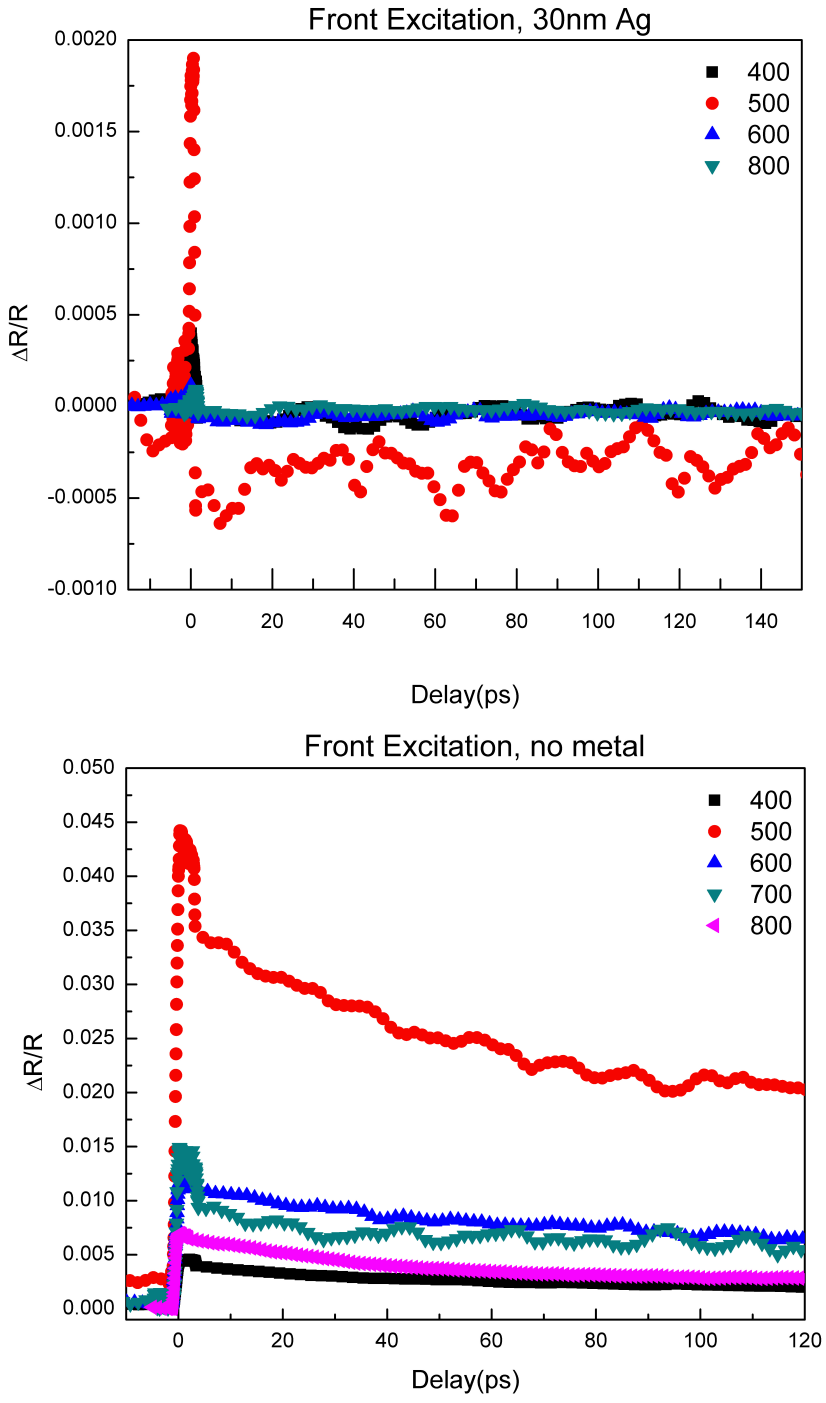

Figure 34: Differential reflection spectra acquired in a forward-orientation for Ag coated and uncoated heterostructures annealed prior to MgO deposition at temperatures of 400-800C

A particularly notable result for these heterostructures is the enhancement of the peak differential reflection in the backward orientation for the Ag coated samples annealed at 400°C and 500°C. In particular, the peak differential reflection for the sample annealed at 400°C is 80 times greater for the Ag coated structure. As mentioned in the previous section, this is a clear example of increased absorption due to scattering by the Ag film.

While not much can be said about the differential spectra taken in the forward orientation because of the previously mentioned sample-atmosphere interactions prior to the MgO deposition, it is worth noting that most differential reflection measurements taken in the forward orientation of the Ag coated structures resembled the spectra for the samples annealed at 400°C, 600°C, and 800°C. In other words, most pump-probe spectra exhibited a weakly resolved sub-ps spike at the zero delay, with no long-term relaxation. The (noisy) long-term behavior for the sample annealed at 500°C suggests that a different defect-state exists for this structure that results in quenching of the conduction band population. This will be discussed in more detail in the next section.

The temperature dependence of the structures annealed after MgO deposition is shown in Figures 35 and 36. As suggested by the PL spectra for the annealed ZnO/MgO bilayers, no resolvable signal was detected for the samples that were annealed at 800°C due to the formation of $Zn_{0.95}Mg_{0.05}O$, and while a clearly resolved signal was observed for the sample annealed at 700°C in the backward orientation, no signal was measured in the forward orientation. This provides further confirmation for the idea the differential reflection is probing the interfacial states, and suggests that the Mg content in the ZnO near the MgO interface is somewhat greater than the Mg content near the Al_2O_3 interface.

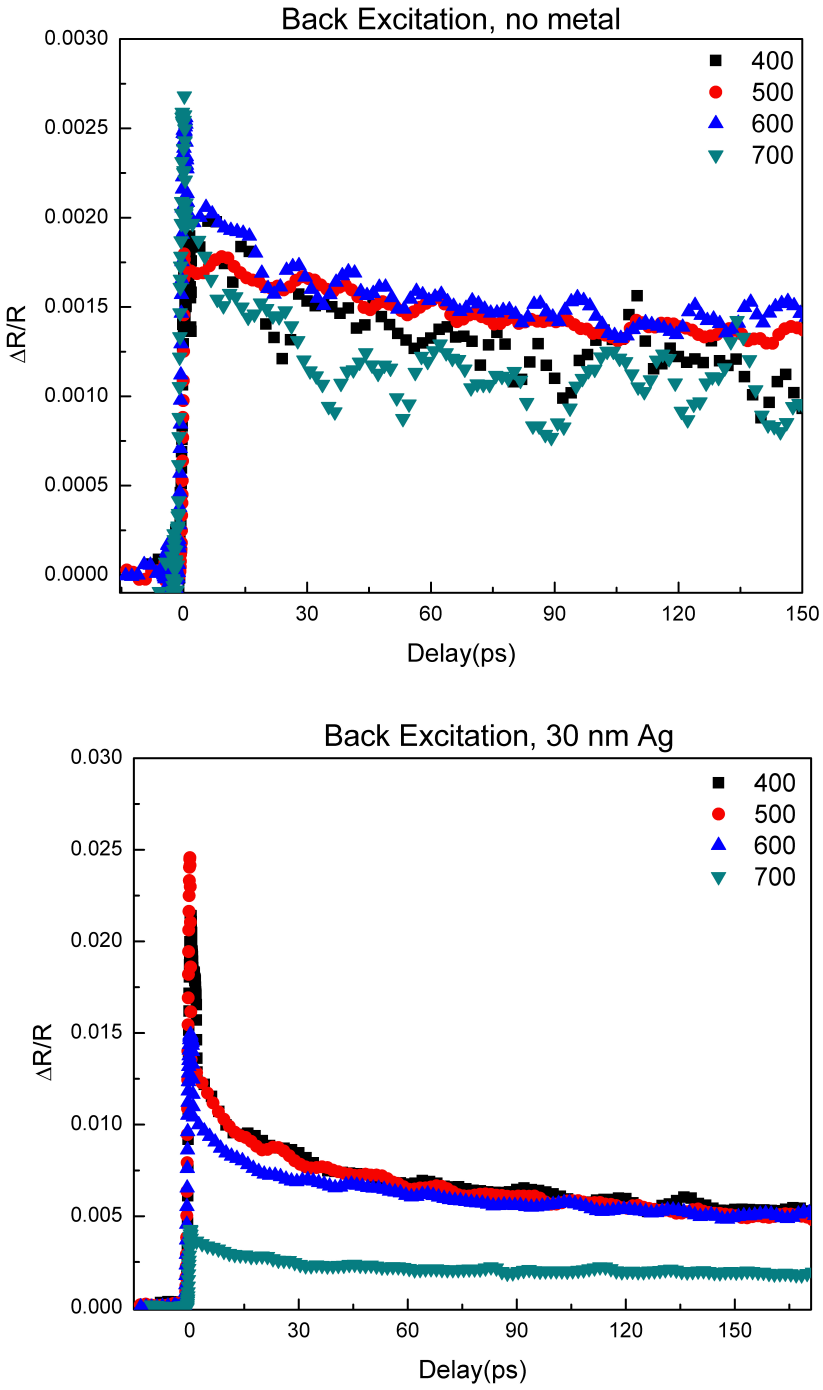

Figure 35: Differential reflection spectra acquired in a back-orientation for Ag coated and uncoated heterostructures annealed after MgO deposition at temperatures of 400-700C.

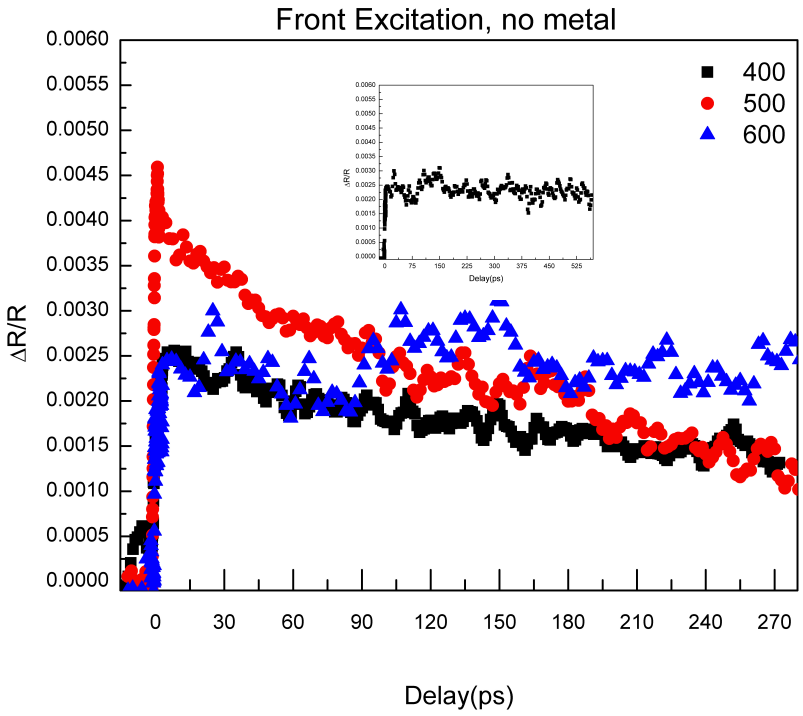

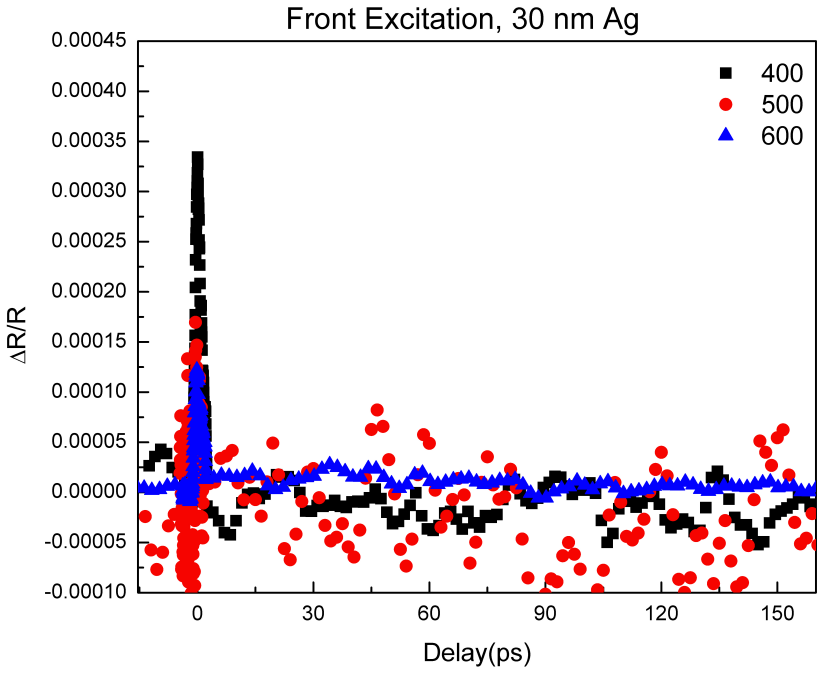

Figure 36: Differential reflection spectra acquired in a front-orientation for Ag coated and uncoated heterostructures annealed after MgO deposition at temperatures of 400-600C. The spectrum for the sample annealed at 600C is blown up in the inset for clarity.

Perhaps the most notable feature of Figure 35 is the consistency of the spectra at each temperature. Unlike the samples annealed before MgO deposition, the differential reflection for the uncoated samples is nearly identical for each annealing temperature. The lone outlier in the Ag coated samples is the sample annealed at 700°C, but given the Mg content in that sample, it would be surprising if the dynamics were the same as the sample annealed at cooler temperatures. Yet again, we see a factor of ten increase in the peak differential reflection, and we see the emergence of a 20 ps decay not present in the uncoated samples. As before, the enhancement of the peak differential reflection is a result of the increased absorption in the ZnO, and the 20 ps decay term is a result of Purcell enhancement that increases the radiative recombination rate.

The temperature dependence of the differential reflectivity in the forward orientation illustrated in Figure 36 is somewhat less consistent than the dependence in the backward orientation seen in Figure 35, primarily because the sample annealed at 600°C demonstrates no decay over a period of greater than 550 ps. Presumably, this is a result of preliminary alloy formation creating long-lived defect-states near the ZnO/MgO interface, but without more experiments, it is difficult to come to a satisfying conclusion regarding these spectra. While the front excitation spectrum for the Ag coated sample annealed at 500°C is noisier than the other two spectra, it does not demonstrate the persistent, negative differential reflection seen in the sample annealed prior to MgO deposition. This will be discussed further in the next section.

4.3.3 PL enhancement at 2.81 eV

Figure 37 illustrates the PL for the metal coated and the non-metal coated heterostructure annealed at 500°C in O_2 prior to the deposition of MgO and Ag (the

differential reflection spectra for the front and back orientation on and off of the Ag were plotted in Figure 33 and 34). This sample was the only heterostructure of all of the previously described annealed structures to demonstrate the sharp emission enhancement centered at 2.81 eV seen in the PL of the Ag coated heterostructure, but — as noted in Chapter 3 — the same peak did appear to a lesser degree for the original 10 nm and 20 nm MgO heterostructures on Al_2O_3. In order to identify this peak, a similar series of experiments was performed. ZnO thin films were annealed at temperatures of 400°C to 800°C in increments of 100°C. In addition to the same 1 L/min O_2 flow used previously, samples were also annealed in ambient atmosphere with no gas flow.

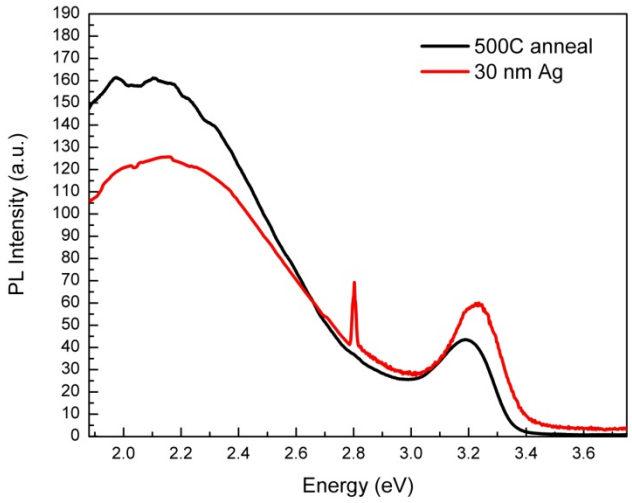

Figure 37: PL spectra for ZnO thin film annealed at 500°C in O_2 prior to deposition of MgO and Ag

The differential reflection and PL spectra for the samples annealed in O_2 reproduced the previous results very well, and the samples annealed in air were fairly consistent with the samples annealed in O_2 except that the differential reflection spectrum obtained in the front orientation for the sample annealed in air at 500°C demonstrated a sub-ps decay followed by a negative differential reflection signal which decayed with a

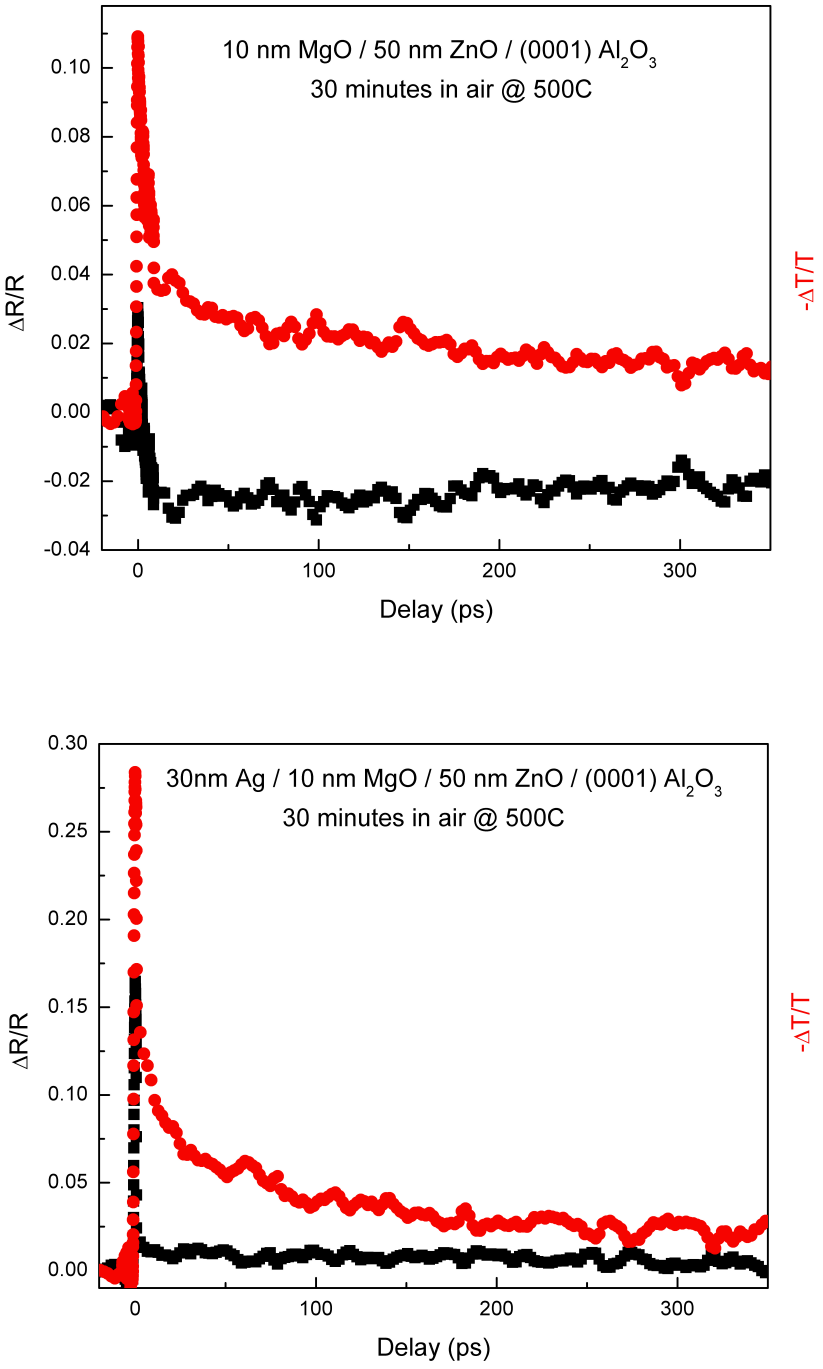

Figure 38: Differential reflection and transmission spectra for Ag coated (bottom) and uncoated heterostructures.

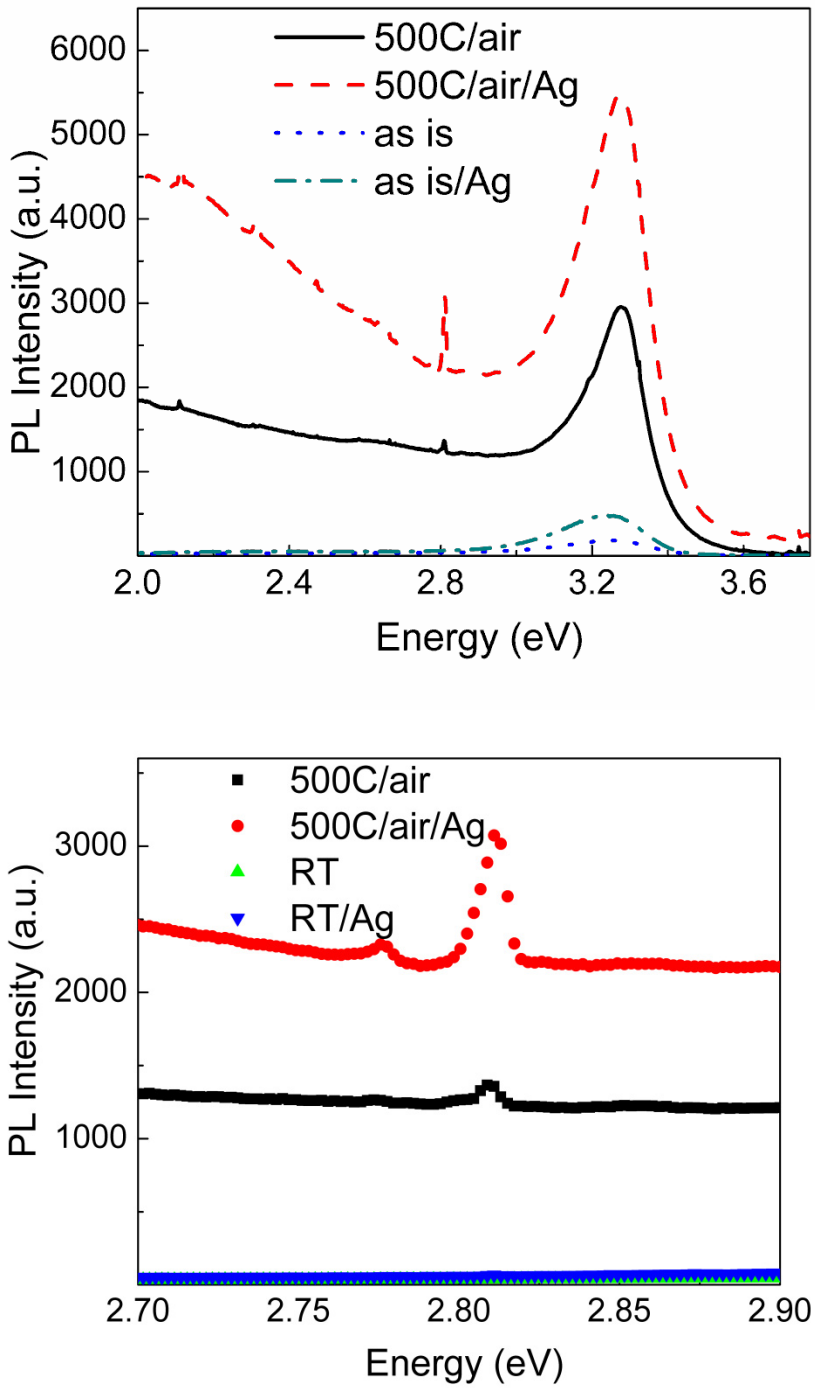

Figure 39: PL spectra of Al_2O_3 / ZnO / MgO / Ag heterostructure annealed at 500C with and without 30 nm Ag film(top) and spectra near 2.81 eV (bottom)

lifetime of at least several hundred picoseconds as seen in Figure 38. In addition, while the PL spectrum of the Ag coated heterostructure annealed at 500°C in air demonstrated a sharp peak centered at 2.81 eV very similar to the one seen in Figure 36 for the Ag coated structure annealed in O_2, the PL of the ZnO/MgO heterostructure in Figure 39 also demonstrated evidence of a much weaker emission at 2.81 eV. In order to demonstrate that this peak is real, and not simply a rogue element on the CCD, the bottom graph in Figure 39 shows the PL spectra for the unannealed ZnO, the annealed ZnO, and the Ag coated heterostructure blown up around 2.81 eV. Finally, this sample was reproduced using the same procedure and the differential reflection and the PL at 2.81 eV demonstrated nearly identical behavior, thus providing additional confirmation that this is a repeatable result.

At this point it is worth recollecting which samples have shown this peak in the PL of the Ag coated heterostructure. In total, it has been seen in the samples annealed at 500°C in O_2 and in air, as well as the unannealed samples with 10 nm and 20 nm MgO film thicknesses discussed in section 3.4. The pump-probe results for these samples are by no means identical, but there are some remarkable similarities. The uncoated sample annealed in air demonstrated a sub-ps decay to a negative differential reflection which decayed over several hundreds of picoseconds in the front orientation. The heterostructure from section 3.4 and 4.2 with the 10 nm MgO film demonstrated nearly identical behavior in the back orientation. The 20 nm MgO heterostructure from the same sections demonstrated a similar sub-ps decay, but also included a ~10 ps decay term before decaying to a negative differential reflection whose recovery was not observed in the 130 ps scan duration. The sample annealed at 500°C in O_2 did not demonstrate the

same negative differential reflection in the uncoated heterostructure, but the Ag coated heterostructure was the only sample among those annealed at 500°C in O_2 to demonstrate a negative long-term differential reflection. While there were notable differences in the pump-probe spectra for each of these samples, there were also significant differences in the preparation of each. Nevertheless, every Ag coated heterostructure described here which demonstrated enhancement in the ZnO PL at 2.81 eV also demonstrated a sub-ps decay combined with a subsequent negative differential reflection in one of the acquired differential reflection spectra. Further, the duplicate of the sample annealed at 500°C in air exhibited the identical differential reflection spectrum and the enhanced PL of the first sample, indicating that, for identical preparations, this is a reproducible phenomenon.

The discussion of plasmonics and impurity states from chapter 1 provides significant context to these results. Figure 1 presented the known impurity states in ZnO as calculated by the full-potential linear muffin-tin orbital method. In particular it noted a Zn interstitial site located 2.9 eV above the ZnO valence band maximum.[13] Figure 4 presented the calculated SPP dispersion relationship for Ag and Au films and demonstrated an asymptote of the Ag-ZnO SPP dispersion relationship and a correspondingly large SPP density of states near 2.9 eV.

It therefore seems quite likely that the enhanced emission at 2.81 eV is a result of a large Purcell enhancement of the recombination rate of the Zn interstitial/near-valence-band-edge-hole impurity state. The enhanced emission at 2.775 eV can therefore easily be understood as an electronic decay from the Zn interstitial site to a separate near valence band impurity state. There is currently only one report of Zn interstitial defect emission in ZnO heterostructures, but the FWHM of the Zn interstitial emission in that

report is nearly 0.7 eV.[127] While we did observe enhanced emission at 2.81 for some un-annealed structures, the consistent observation of the enhanced emission for the structures annealed at 500°C, coupled with the consistent observation of the negative differential reflection in the front orientation for the same structures suggests that annealing at 500°C creates a large population of Zn interstitial states near the ZnO/air interface. The samples coated with MgO prior to annealing lacked a ZnO/air interface, and as a result, the oxygen atoms near the surface could not escape the surface during the annealing process. The sub-ps decay seen in the differential reflection measurements can only be understood in the context of a radiative decay of the conduction band electrons to the Zn interstitial sites, followed by a long time constant (several hundred picoseconds) decay of the electron bound to the Zn interstitial site to the valence band-edge. While this process was not generally observed in the PL — likely due to a combination of the large background spectrum and non-radiative decay routes — the large Purcell enhancement of the radiative decay rate resulting from the significant SPP density of states allows for observation of this state in films with a large Zn interstitial population. The PL spectrum of the ZnO thin film annealed in air demonstrated a weak emission at 2.81 eV and the strongest evidence of decay to the Zn interstitial state in the pump probe spectrum because of the greater population of Zn interstitial states expected due to the low oxygen partial pressure during the annealing process, but the Purcell enhancement in each case allows for the observation of defect states that are poorly resolved – or not resolved – without the presence of plasmonic elements.

CHAPTER 5: STRONG-COUPLING IN ZNO QUANTUM WELL - AL NANODISC HETEROSTRUCTURES

All of the coupling energetics and dynamics presented thus far can be described as being within the weak coupling regime because of a combination of minimal plasmon-exciton spectral overlap and scattering due to large surface roughness that prevented coherent energy exchange. In order to bridge the gap to the strong coupling regime, ZnO quantum wells were fabricated and capped with Al nanodisc arrays. These structures provided both excellent surface roughness and the flexibility of tunable plasmon resonances (by varying the Al nanodisc diameter) and tunable QW emission (by varying the QW well width).

It proved difficult to achieve true resonance between the Al LSP and the quantum confined exciton because of the LSP red-shift caused by the large $Zn_{0.85}Mg_{0.15}O$ dielectric function and because of the nanodisc size limitations imposed by the lithographic process, but by varying the disc size and the grating constant for the nanodisc arrays, a series of arrays was found that demonstrated the formation of a hybrid LSP quadrupole/QW exciton state. The Fano-like resonance formed between the quadrupole 'plexciton' state and either the LSP dipole or the QW exciton is also unreported in the literature for any material system. This is the first evidence of a strongly coupled plasmon-exciton system in the near-UV, and is therefore of significant importance

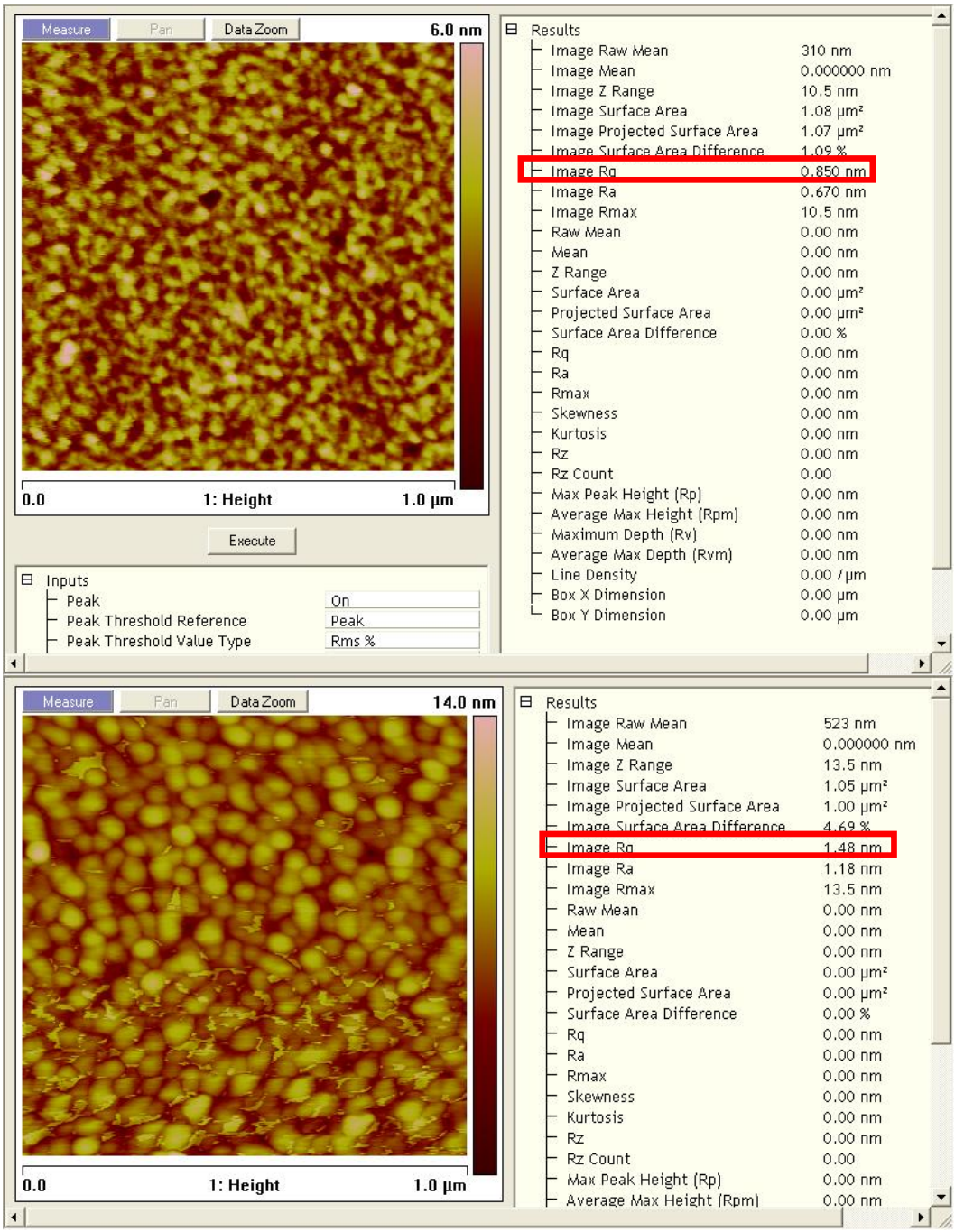

Figure 40: Atomic-force microscope images for $Zn_{1-x}Mg_xO$ thin films grown with x=0.05 target (top) and x=0.10 target (bottom) at 700C in 1mTorr O_2 background.

fundamentally as well as for applications as diverse as designed dielectric systems[81, 128] and correlated photon sources.[129]

5.1 QW design and optical characterization

ZnO quantum wells are frequently grown on ZnO substrates[27] or on thick ZnO buffer layers[43] in order to avoid the large sapphire-ZnO lattice mismatch seen in Table 1. In order to minimize the number of emitter wavelengths observable in photoluminescence experiments, the quantum wells grown for this project were deposited directly on (0001) sapphire with no ZnO buffer. Minimizing surface roughness was therefore a significant initial concern.

In order to maximize the barrier potential without suffering from the MgO segregation within the $Zn_{1-x}Mg_xO$ that occurs around 30% Mg,[130] targets with 5% Mg and 10% Mg were considered for the fabrication of the $Zn_{1-x}Mg_xO$ barrier layers. As described in Chapter 2, the ZnO and $Zn_{1-x}Mg_xO$ layers were grown at temperatures of 500 - 800ºC and background pressures of 1.0 – 10.0 mTorr O_2. Atomic force microscopy (shown for samples deposited at 700ºC in 1 mTorr O_2 in Figure 39) demonstrated that samples grown at 700 ºC in a background of 1 mTorr O_2, the minimum maintainable stable pressure for the mass flow controller used with this PLD chamber, had a significantly lower RMS surface roughness than those grown at any other temperature. While the 1.48 nm RMS surface roughness for the films grown with the 10% Mg target was respectable, the 5% Mg target was chosen for its 0.85 nm RMS surface roughness, and all quantum wells for this project were ultimately fabricated using the 5% Mg target. Figure 41 shows an energy dispersive x-ray spectrum for one of the films deposited using

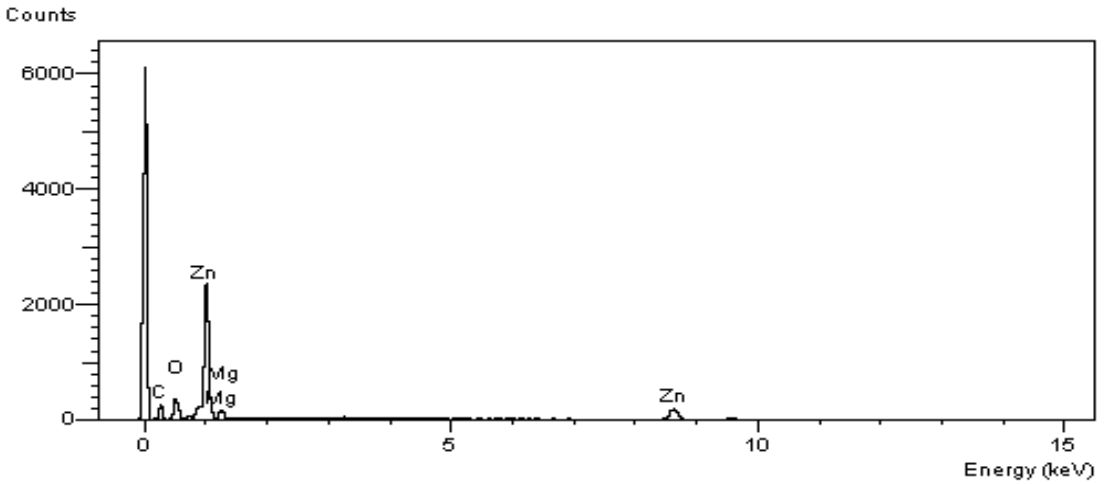

Figure 41: EDX spectrum for $Zn_{1-x}Mg_xO$ film deposited using 5% Mg target under 1 mTorr O_2 at 700°C

the 5% Mg target. Ten such scans across two representative films yielded x=0.154 ± 0.013, compared with x=0.22.4 ± 0.026 for the films fabricated with the 10% Mg target; the disparity between the target stoichiometry and the film stoichiometry is a result of the difference between the Zn and Mg vapor pressures.[26] Examination of SEM images of the film at the position at which each EDX spectrum was acquired demonstrates clearly that the higher standard deviation was a result of the relatively low Mg content in grains with characteristic dimensions of 50-100 nm that appeared frequently on the x=0.224 surface but only sporadically on the *x*=0.154 surface. Transmission electron microscope (TEM) images of the cross-section of ZnO and $Zn_{0.85}Mg_{0.15}O$ thin films grown with an laser repetition rate of 1 Hz for 15 minutes were used to show that — for the deposition parameters described in Chapter 2 — the ZnO deposition rate was 3.0 nm/minute, and the $Zn_{0.85}Mg_{0.15}O$ deposition rate was 2.6 nm/minute.

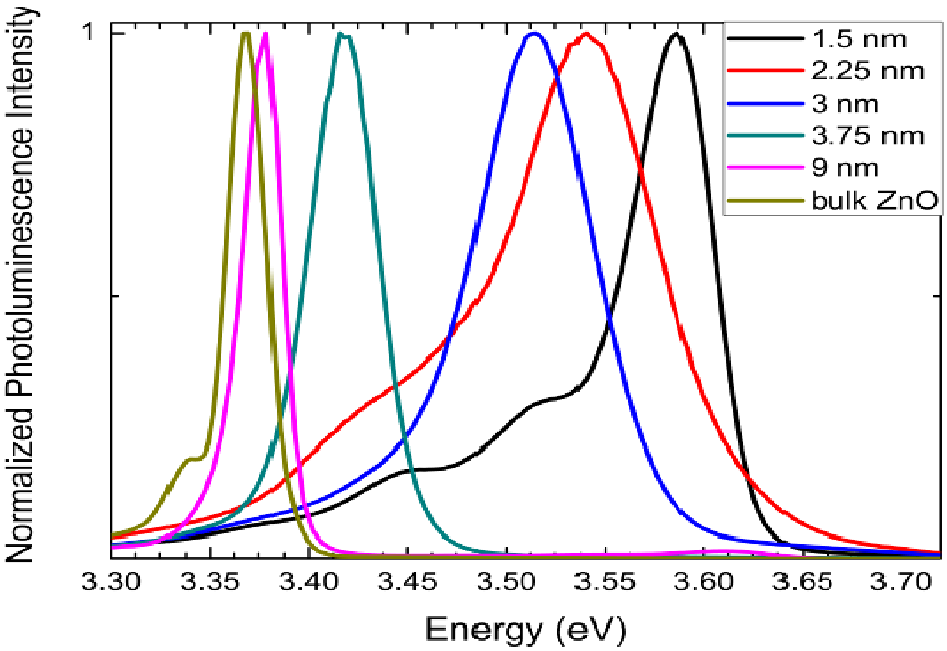

Figure 42: Low temperature (15K) PL for QWs of the form sapphire/ 40 nm $Zn_{0.85}Mg_{0.15}O$/ x nm ZnO/ 15 nm ZnO

The initial QWs grown for this project were of the form (0001) sapphire/40 nm $Zn_{0.85}Mg_{0.15}O$/*x* nm ZnO/15 nm $Zn_{0.85}Mg_{0.15}O$, with the well-width *x* varying from 1.5 to 3.75 nm in increments of 0.75 nm. The normalized low-temperature (15K) PL spectra of these wells are shown in Figure 42 along with a 9 nm-thick well included to demonstrate the large well width limit. The LO phonon energy for ZnO is ~70meV,[24] so the shoulders observable on the 1.5 nm well can be attributed to the recombination of excitons bound to neutral donors (D^0X) and the first order LO replica of D^0X.

As with the multilayer film structures discussed in Chapters 3 and 4, varying the plasmon-exciton separation could potentially help elucidate the energetics and dynamics of the coupled states. Figure 43 shows the 15K PL of QWs of the form sapphire/40 nm $Zn_{0.85}Mg_{0.15}O$/ 4.5 nm ZnO/x nm $Zn_{0.85}Mg_{0.15}O$ with x varying from 10 to 60 nm in increments of 10 nm. These spectra have a localized exciton peak from 3.38 to 3.41 eV with the 30 meV blue-shift occurring with increasing top barrier thickness. This blue-shift is most likely a result of the increased barrier layer performance — which yields stronger confinement — with increasing barrier thickness, but it may also simply be a superposition of the QW emission with the tail of the barrier emission. The D^0X and D^0X LO replicas seen in Figure 42 are clearly visible, as is the barrier emission near 3.61 eV. The barrier emission increases with increasing top barrier thickness, though even in the case of the 60 nm barrier, the separate peaks are easily resolved.

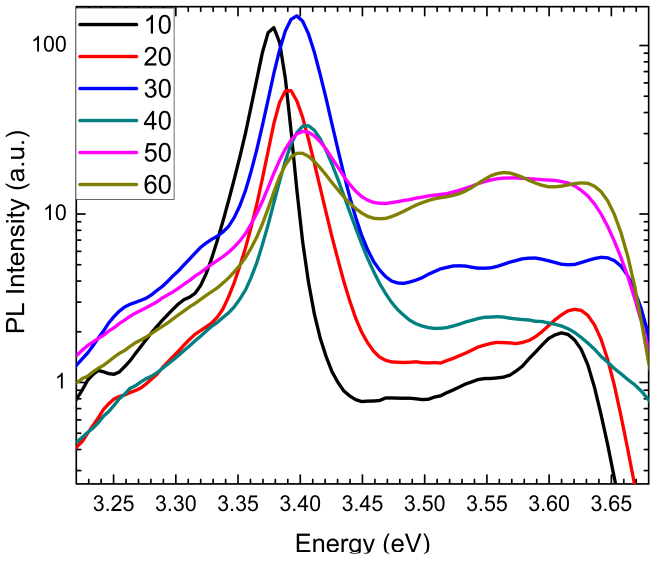

Figure 43: 15K PL of QWs of the form sapphire / 40 nm $Zn_{0.85}Mg_{0.15}O$ / 4.5 nm ZnO / x nm $Zn_{0.85}Mg_{0.15}O$ with x varying from 10 to 60 nm in increments of 10 nm.

5.2 Aluminum nanodisc growth on QWs

Even in the small-particle limit, Ag and Au LSP resonances do not extend to the near-UV, so Al nanodisc arrays were fabricated on the QWs in an attempt to maximize the spectral overlap of plasmon and exciton. While metal-nanoparticle arrays were easily fabricated by electron beam lithography on ZnO and MgO substrates and on ITO coated glass, successful lithography on the QWs proved somewhat more difficult. This was largely a result of the high surface roughness (5-10 nm RMS) of the initial films grown at the University of Florida, which provided further motivation for the fabrication of the ~1 nm RMS quantum wells that were ultimately used.

The sheet resistance of the quantum wells was measured using a multimeter in a two-point probe configuration. Because the QWs had a sheet resistance of roughly 1 MΩ/square compared with roughly 500 Ω/square for the ITO coated glass substrates, and because this large resistance was clearly manifested by charging during SEM imaging at magnifications greater than 1kX, the initial lithographic attempts were facilitated by the sputtering deposition of a 2 nm Au film after PMMA spin coating but before patterning. This Au layer was laid down with a 120s deposition using the Au sputtering chamber located in the VINSE electron-optics lab, and after exposure of the pattern, etched using a *Transene* type TFA Au etchant. Use of the Au layer eliminated the charging problem, but the increased electron scattering caused by the Au thin film made it impossible to achieve the nanoparticle diameters smaller than 80 nm necessary to obtain even minimal LSP-exciton spectral overlap. Because of this problem, further attempts were made to perform electron beam lithography without the Au conduction layer, and it was determined that — even though charging still impeded the imaging of

the QW surface, making write-field alignment extremely difficult — successful electron beam lithography could be performed without the Au film.

The SEM images of Al nanoparticle arrays fabricated on ITO coated glass by electron beam lithography with dot-doses of 5-40 fC are shown in Figure 44. Because of the formation of a self-limiting oxide layer on the nanoparticle surface, it was difficult to achieve a significant contrast between the nanoparticles and the substrate, so the contrast was enhanced using *ImageJ* image processing software after image acquisition with a setting of 0.2% saturation. The doughnut appearance is therefore not a true representation of the particle geometry; rather it is a realization of the greatest scattering occurring at the disc edges, resulting in the appearance of a hollow core, especially after contrast enhancement.

The discs in Figure 44 were fabricated with a 300 nm grating constant, and dot doses of 5-40 femtoCoulombs (increasing from left to right and top to bottom). The particle size is clearly dependent on dose size, and the average particle diameter in each SEM image is plotted in the left of Figure 45 for both 225 nm and 300 nm gratings. The graph on the right of Figure 45 compares the average particle size for arrays with 225 nm grating constants that were deposited on ITO coated glass with arrays deposited under identical conditions on a QW with a 9 nm well width and a 50 nm top barrier layer (arrays deposited with dot doses of less than 20 fC could not be resolved by SEM on the QW). Because of the charging problem seen in the QW structures, the nanodiscs on the QW were imaged by sputtering 2 nm of Au on top of the nanodiscs after all optical measurements had been acquired. The increased particle size seen in the arrays with the 225 nm grating is the result of a proximity effect due to electron scattering. In principle

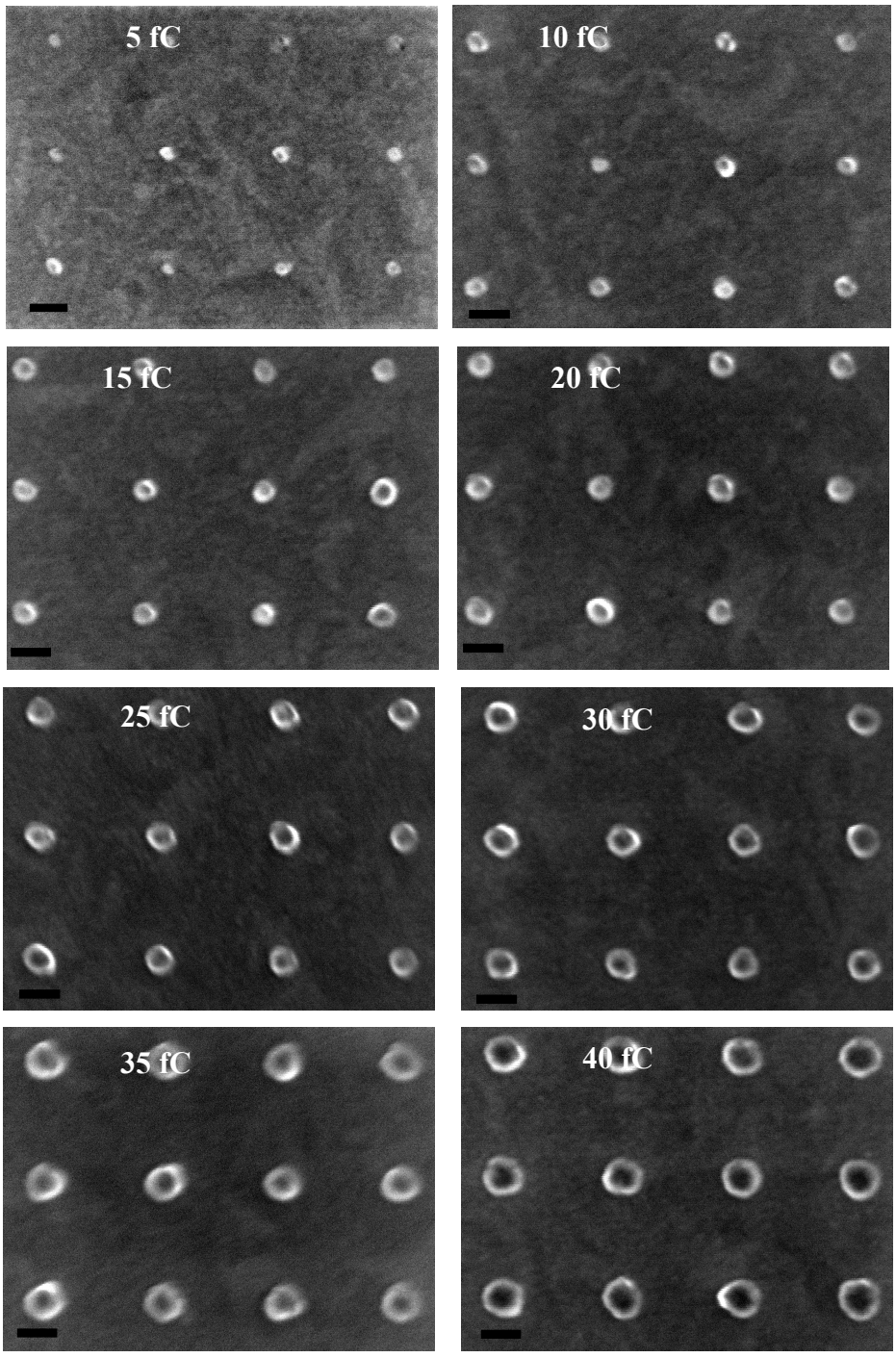

Figure 44: SEM images of Al nanoparticle arrays deposited on ITO coated glass with a 300 nm grating constant and dot doses of 5-40 femtoCoulombs.

it is possible to counter these effects with designed area doses over the patterned area, but such approaches take significantly longer to pattern, and ultimately would not be beneficial to this project, as it is simple enough to characterize the disc size after lithography.[131] The smaller particle sizes seen in high doses on QWs are a result of charging; the increased scattering results in a smaller realized dose at the nanodisc location. This error results in poor precision, and can be avoided somewhat by using a smaller working distance,[132] but because the patterns used for this project all have circular symmetry, it is not as significant an issue as it would be for the fabrication of less symmetric metamaterials such as split-ring resonators.

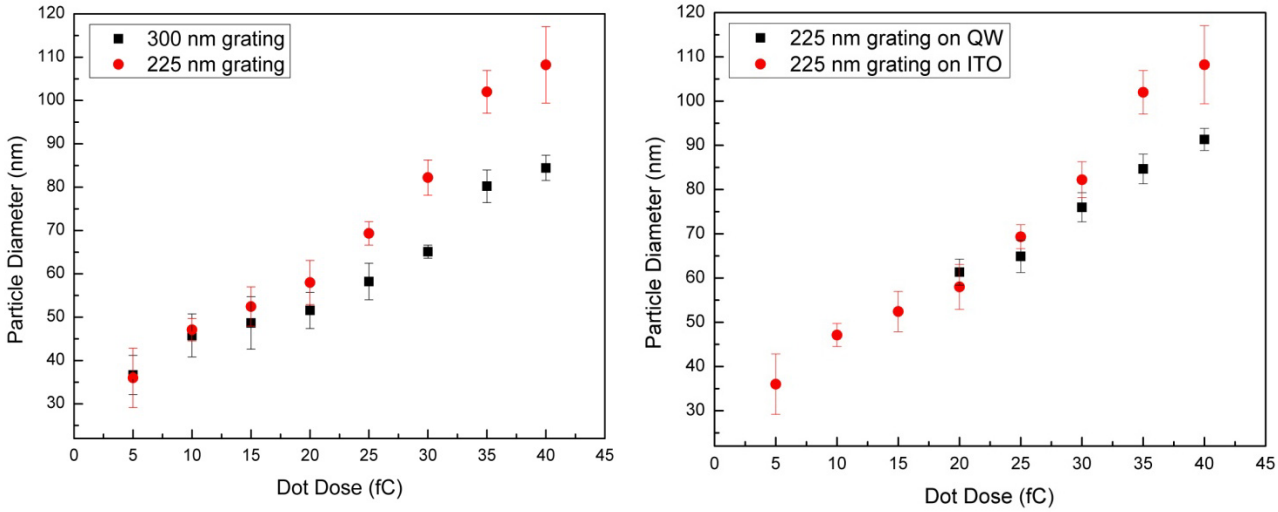

Figure 45: Average particle diameters for Al nanoparticle arrays on ITO coated glass with grating constants of 225 nm and 300 nm (left), and average particle diameters for arrays with 225 nm grating constant on ITO coated glass or 9 nm well width QW (right).

5.3 Finite Difference Time Domain simulations

In order to calculate the nanodisc array absorbance spectra and the spatial distribution of the electric field intensity in the vicinity of each nanodisc, finite difference time domain (FDTD) simulations were performed using Lumerical FDTD solutions 7.5, a commercial optical design software. FDTD simulations discretize the volume of interest

and solve Maxwell's equations at each spatial position within the time domain, before using fourier analysis to obtain the electric and magnetic fields within the frequency domain.

The simulations presented in this section were performed using a high precision non-uniform mesh with a 1 nm overlay mesh surrounding the nanodisc. Periodic boundary conditions were utilized in order to simulate disc grating constants of 225 nm and 300 nm for nanodiscs with diameters of 40 – 100 nm and thickness of 20 nm. The aluminum nanodiscs were described using the Palik Al dielectric function, [47, 48] and the quantum wells were described with a 500 nm bottom barrier layer, a 9 nm ZnO well layer, and a top barrier layer of 10 nm. The $Zn_{0.85}Mg_{0.15}O$ barrier layers were described by the $Zn_{1-x}Mg_xO$ dielectric function presented by Schmidt *et al.*[133] and the ZnO well was described by the Palik ZnO dielectric function.[47, 48] This model neglects strain effects on the ZnO dielectric function, but it provides a good approximation because the large well thickness minimizes strain effects.

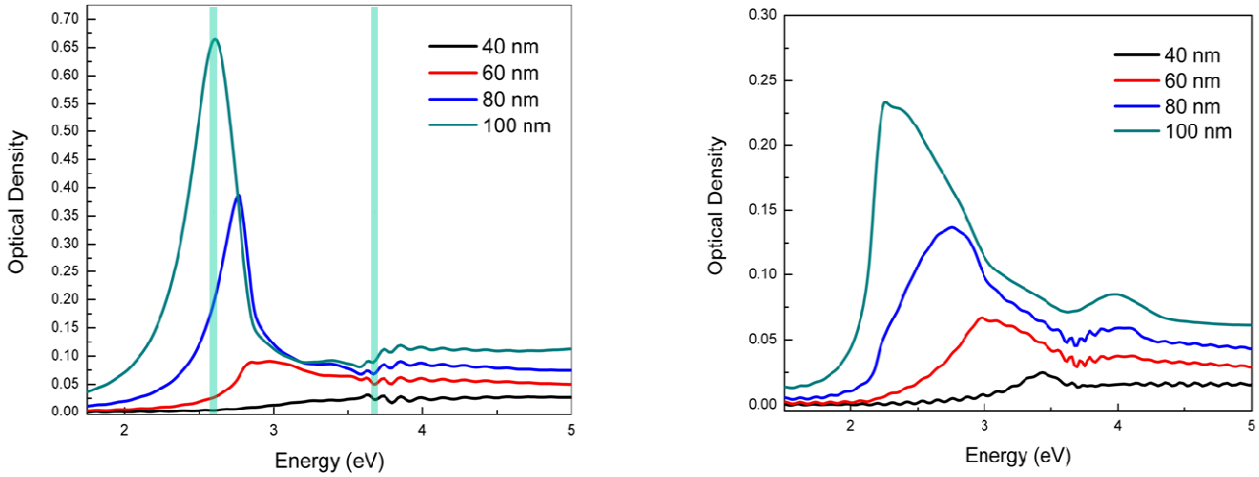

Figure 46: Absorbance spectra calculated by FDTD simulations for nanodiscs 40 - 100 nm in diameter with a grating constant of 225 nm (left) and 300 nm (right).

Figure 46 presents the absorbance spectra for the nanodisc arrays described in the previous paragraph. The peak LSP absorbance red-shifts dramatically with increasing disc diameter for both the 225 nm grating constant and the 300 nm grating constant, though the absorbance of the 40 nm diameter discs is very poorly resolved. The noise between 3.5 and 4.5 eV is spectrally coincident with the onset of the imaginary component of the $Zn_{0.85}Mg_{0.15}O$ dielectric function. It is therefore reasonable to conclude that the noise is a result of the fit chosen for the $Zn_{0.85}Mg_{0.15}O$ dielectric function, though there is no reason to conclude that this noise suggests any additional problems with the simulation.

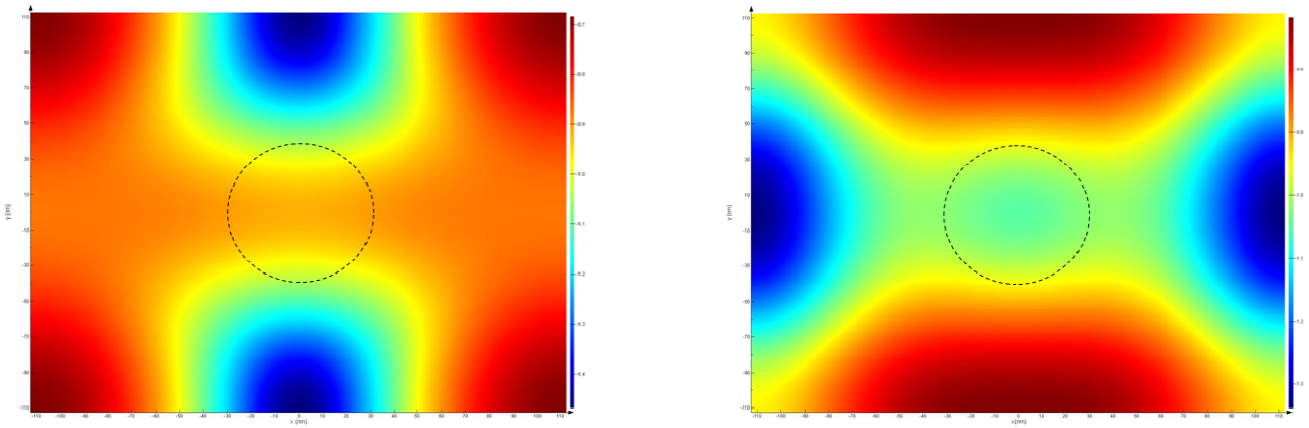

Figure 47: Electric field intensity profile 100 nm below Al nanodisc calculated by FDTD for 100 nm diameter particle at 3.65 eV (left) and 2.61 eV (right). Dashed lines outline the position of the nanodisc

A small dip in the absorbance spectra near 3.65 eV is present for both the 225 nm grating constant and the 300 nm grating constant, consistent with the quadrupole modes observed in the literature for larger colloid-mask-prepared random Al nanodisc arrays.[134] The far-field electric-field intensity – measured 100 nm below the 100 nm diameter disc at 3.65 eV and 2.61 eV – is shown in Figure 47 as clear evidence of the quadrupolar nature of the peak near 3.65 eV and the dipolar nature of the peak near 2.61 eV. These

field intensity profiles were consistent across all disc diameters and for both grating constants.

The electric field intensity profile normal to the quantum well surface is shown in Figure 48. The dipole mode demonstrates the expected field enhancement within the $Zn_{0.85}Mg_{0.15}O$ due to the large dielectric function, but the quadrupole mode demonstrates a field enhancement within the ZnO well layer denoted by the dashed lines.

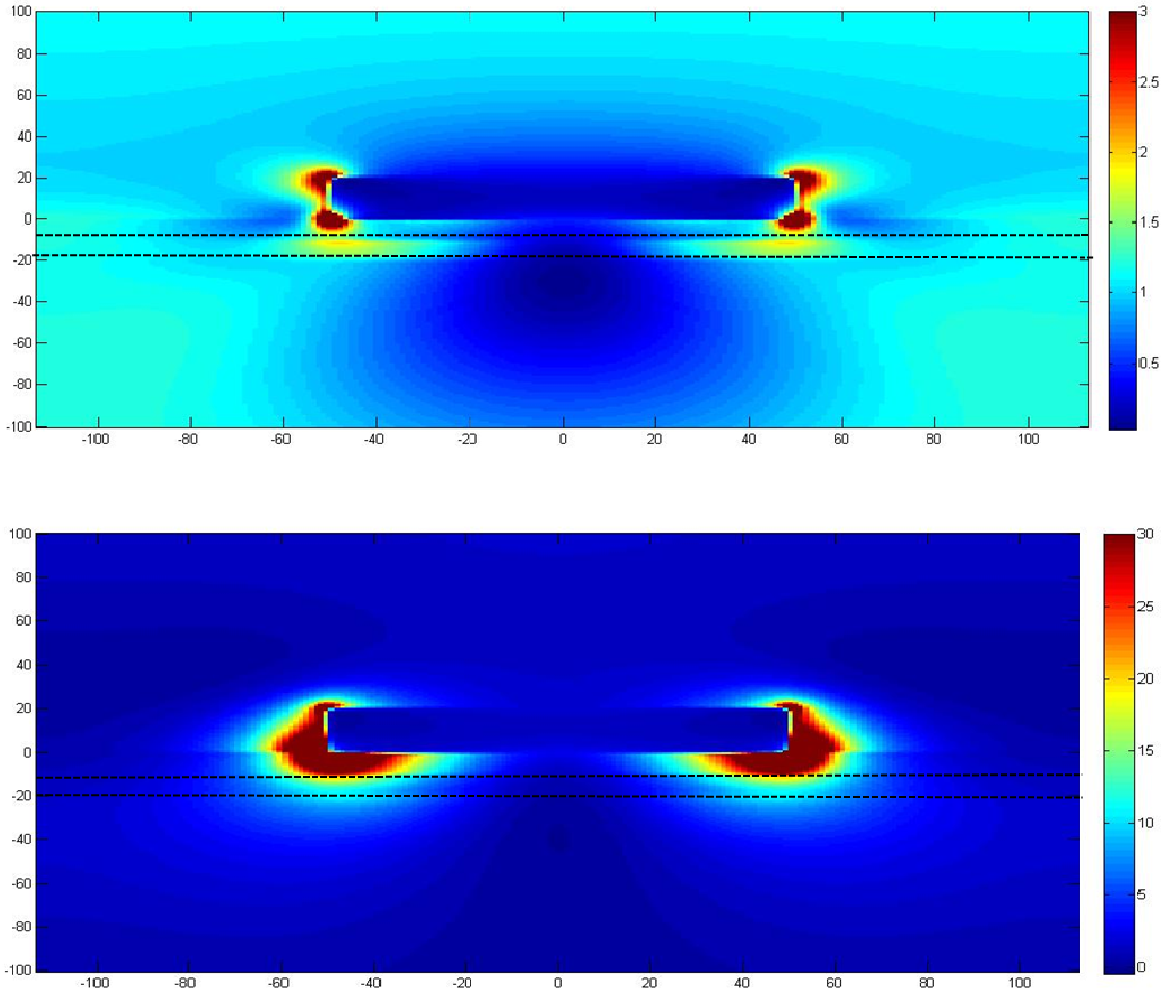

Figure 48: Electric field intensity profile normal to quantum well surface calculated by FDTD simulations. Dashed lines indicate ZnO well layer.

It is important to note that the FDTD simulations only modeled the nanodisc plasmonic response within the classical regime described by Maxwell's equations. No excitonic phenomena were described by this model, and no quantum mechanical behavior was described. The plasmon response was determined in part by the quantum well dielectric function, but these results did not describe any coupling effects.

5.4 Confocal extinction measurements

Aluminum nanoparticle arrays fabricated with dot doses of 5 - 40 fC and grating constants of 150 nm, 225 nm, and 300 nm, and dot doses of 40 - 70 fC with a grating constant of 450 nm were fabricated on ZnO / $Zn_{0.85}Mg_{0.15}O$ quantum wells with a 40 nm bottom barrier layer, a 9 nm well width, and a top barrier layer which varied between 10 nm and 60 nm in 10 nm increments. The absorbance of these nanodisc-QW heterostructures were calculated as described in equation 2.1, where I_{tr} and I_0 are the transmitted intensities through the nanodisc arrays and through the QW near the arrays respectively, and I_d is the 'dark' background spectrum acquired with the light source blocked. Initially, multiple measurements of I_0 were taken in order to ensure a consistent reference intensity, but it became clear that — for the ~80 micron white light spot size — the relative variation in transmitted intensity at every position within ~500 microns of the array was less than 10^{-4}. Because of the relatively weak UV intensity of the tungsten lamp, and because of absorption by the beamsplitter and the objectives used in the microscope, each spectrum presented in this section represents the average of 10^5 individual spectra acquired with a 2 ms integration time.

The absorbance spectra for nanodisc arrays with dot doses of 40-70 fC with a 450 nm grating constant are shown in Figure 49. Because of the large grating constant, and

the already minimal contrast, reliable measurements of the particle size were difficult to acquire. Despite nominal spectral overlap between the LSP absorbance spectra and the QW photoluminescence, the LSP spectra demonstrate no additional resonances characteristic of the stroung coupling regime. The lineshapes are roughly the form of typical Lorentzian dipole local surface plasmon absorbance spectra, the increased optical density observed with increasing dot dose (and corresponding increasing nanodisc diameter) is expected due to increased scattering cross-sections, but the red-shift caused by size-dependent damping predicted by FDTD simulations is very minimal. This suggests that weak coupling between the Al nanodisc LSP and the QW exciton may result in altered lineshapes with enhanced absorbance near the QW exciton. The monotonic increase in optical density with increasing disc diameter in the UV results

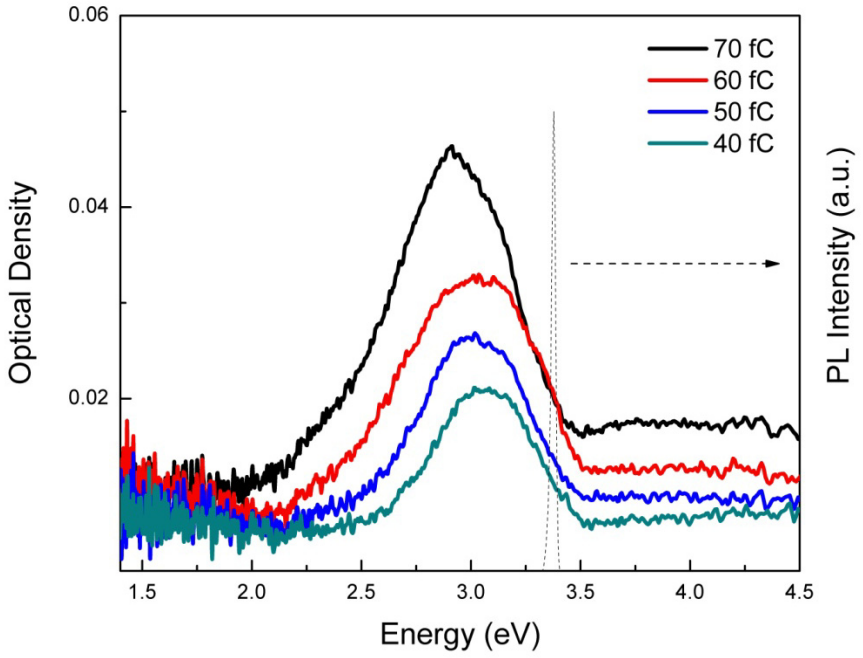

Figure 49: Room temperature absorbance spectra for Al nanodisc arrays with dot doses of 40-70 fC and grating constant of 450 nm on a 9 nm well width QW with 20 nm top barrier, and the PL intensity of the QW at 15K.

from the emergence of the aluminum LSP quadrupole moment due to the increased ratio of particle diameter to grating constant.[134]

The absorbance spectra for Al nanodisc arrays fabricated on the same 9 nm QW with doses of 5-40 fC and grating constants of 300 nm (left) and 150 nm (right) are shown in Figure 50. No arrays could be found by confocal imaging or SEM for the 5, 10, and 15 fC doses with the 300 nm grating constant arrays, but the larger-diameter disc arrays demonstrated the same dipole and quadrupole plasmon absorbance characteristics seen in Figure 49. All of the arrays with the 150 nm grating constant were overdosed, resulting in failed liftoff, except for the 5, 10, and 15 fC arrays. Of those, the 5 fC arrays were under-dosed, also resulting in no nanodiscs visible by SEM or confocal microscopy, but the 10 and 15 fC doses resulted in clearly defined arrays. As with the other arrays, the larger dose results in larger diameter discs, and a correspondingly larger optical density, and a slightly red-shifted resonance. However, the quadrupole peak is not clearly resolved for these spectra, likely as a result of reduced interparticle coupling. An important point to recall is that – primarily because of the large sheet resistance of the QWs — doses of 5 fC or less result in underdosing which yields no discs, and doses of 10 to 15 fC only result in nanodiscs for arrays with a sufficiently small grating constant. As a result, it is difficult to achieve disc diameters of less than 50 nm on the QWs by electron beam lithography. While all of the nanodisc extinction spectra shown thus far are near resonance with the QW, because of the relatively large $Zn_{0.85}Mg_{0.15}O$ dielectric function (ε_1=4.56 at 365 nm) and because of the limitation on particle diameter presented by the current technique, it appears impossible to fabricate nanodisc arrays that achieve true resonance between the nanodisc dipole LSP and the QW exciton.

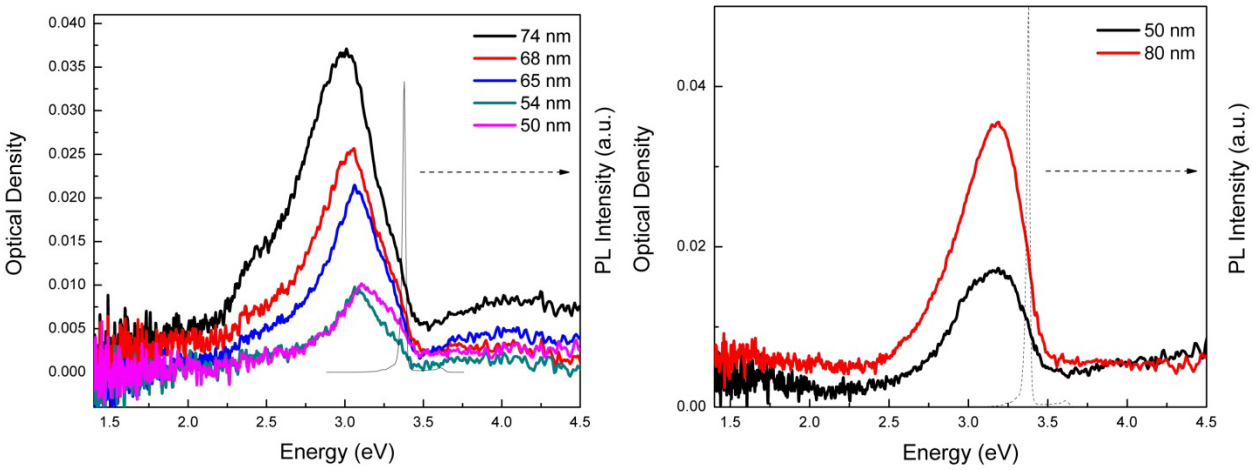

Figure 50: Room temperature absorbance spectra for Al nanodisc arrays with dot doses of 20-40 fC (50-74 nm) (left), and 10 and 15 fC (50 and 80 nm) (right) with 300 nm and 150 nm grating constants respectively deposited on a 9 nm well width QW with a 20 nm top barrier layer, and the QW PL intensity at 15K.

Despite the difficulty of achieving maximal exciton-plasmon resonant coupling, the nanodisc arrays fabricated with a 225 nm grating constant presented dramatically different absorbance spectra than those seen previously. Like the 300 nm arrays, discs fabricated with doses of 20 fC through 40 fC were easily imaged by SEM and characterized by confocal absorbance microscopy, but as Figure 51 shows, sharp Fano-resonance-like peaks not seen in Figures 49 and 50 are clearly resolved in these absorbance spectra.

Note that the 225 nm grating constant resulted in significantly larger disc diameters than those seen in the larger grating constant arrays for the same dot doses. While these spectra demonstrate the same features seen in the other arrays – namely a proportional relationship between disc diameter and optical density, and the red-shift of the plasmon resonance and emergence of the quadrupole moment with increasing disc

diameter – they also demonstrate sharp resonances near 3.03 eV and 3.09 eV. Table 3 summarizes the results of each QW/nanodisc array heterostructure.

Because the original intent was to study the coupling as a function of plasmon-exciton separation, identical arrays were fabricated on 9 nm well width QWs with top barrier layers that varied in thickness from 10 nm to 60 nm. The absorbance spectra for the arrays with top barrier thicknesses of 30-60 nm appeared very similar to the spectra in Figure 51, but the absorbance spectra for the 10 nm barrier layer QW, shown in Figure 52, were markedly different.

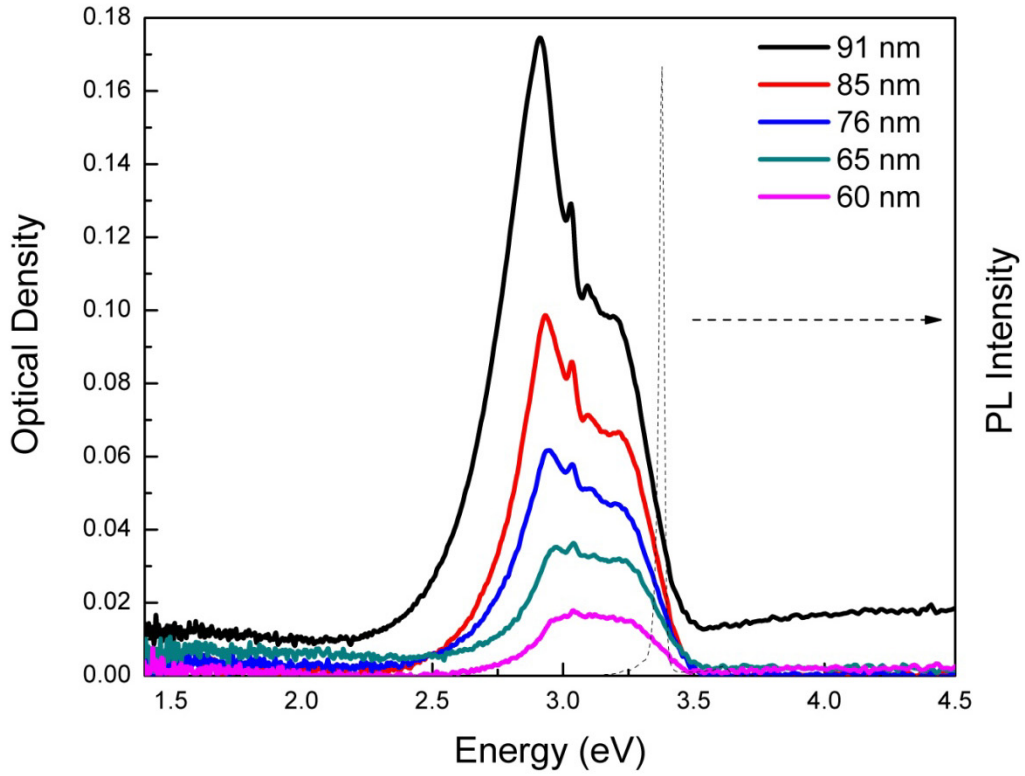

Figure 51: Room temperature absorbance spectra for Al nanodisc arrays with dot doses of 20-40 fC (60-91 nm) with 225 nm grating constant deposited on a 9 nm well width QW with a 20 nm top barrier layer, and the QW PL intensity at 15K.

Grating constant	Dot doses produced	Disc Diameter	Nanodisc absorbance behavior	Figure number
450 nm	40-70 fC	Unknown	Dipole absorbance peak 3.06-2.90 eV Broad UV quadrupole absorbance	46
300 nm	20-40 fC	50-74nm	Dipole absorbance peak 3.11-2.99 eV Nominal UV quadrupole absorbance	47left
225 nm	15-40 fC	60-91 nm	Dipole-like absorbance peak 2.99-2.96 eV Fano-like peaks at 3.03 and 3.09 eV Absorbance shoulder at 3.2 eV No quadrupole except for 40 fC	48
150 nm	10,15 fC	50-80 nm	Dipole absorbance peak 3.18-3.19 eV Nominal UV quadrupole absorbance	47right

Table 3: Summary of absorbance spectra features for nanodisc arrays with grating constants of 150-450 nm.

Upon further investigation, it became clear that the distinction between the six wells was that the 10nm barrier layer well was of extremely poor optical quality — no ZnO emission was observed in its room-temperature PL spectrum — whereas the other five samples demonstrated strong band-edge photoluminescence. While the original intention had been to probe the coupling strength as a function of exciton-plasmon separation, the similarity in the absorbance spectra for barrier layers 20-60 nm thick make it clear that the Al LSP decay length is significantly longer than the decay length for Ag and Au LSPs; QWs with significantly thicker barrier layers would have to be fabricated to facilitate such a study.

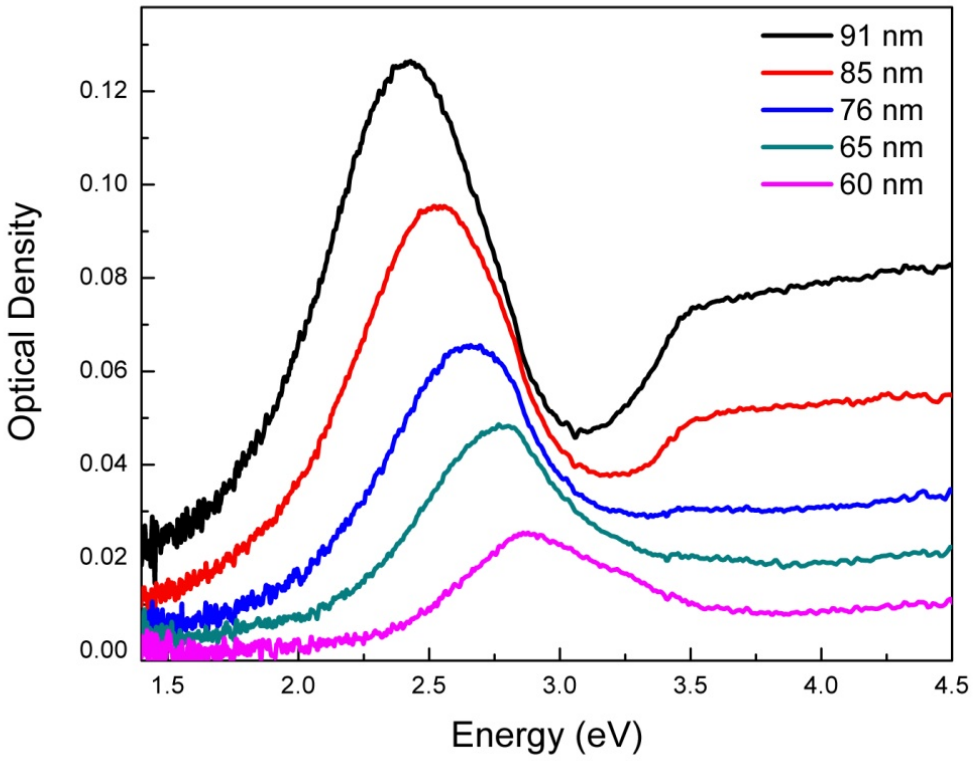

Figure 52: Room temperature absorbance spectra for Al nanodisc arrays with dot doses of 20-40 fC with 225 nm grating constant deposited on a poor optical quality 9 nm well width QW with a 10 nm top barrier layer.

Two features immediately stand out in Figure 52: the dramatically broader and red-shifted dipole resonance, and the dominant quadrupole moment which emerges in the mid-UV. The lack of a Fano-like resonance near 3 eV is also notable. Two identical sets of arrays were fabricated on each QW, and in each case—excluding the occasional overdose at 40 fC or the occasional under-dose at 20 fC — the second array was consistent with the first. Because of an initial concern about the number of arrays that were not surviving liftoff due to what is now understood to be overdosing or under-dosing, an identical set of arrays was fabricated on an identically prepared set of QWs. This second set of arrays reproduced the behavior of the first set except that the 30 nm

barrier thickness well also manifested very low PL intensity and the Al nanodisc arrays deposited on it exhibited similar absorbance spectra to those shown in Figure 52, providing further corroboration that the distinction between Figures 51 and 52 is the presence of a high optical quality ZnO quantum well.

In order to better understand the interactions that caused the peaks in the nanodisc absorbance spectra on high optical quality quantum wells, the absorbance spectra of only the 225 nm grating constant arrays were re-acquired at several temperatures between 77K and 332K. The absorbance spectra at 77K and 332K shown in Figure 53 illustrate the two distinct regimes. Below room temperature, the three previously described peaks remain, though the peak at 3.03 eV is more clearly defined, and the shoulder that appeared in the room temperature spectra appears as a clearly defined fourth peak. Above room temperature, these peaks have formed a large shoulder on otherwise normal dipole LSP absorbance spectra. The 20 fC dose arrays were excluded from these graphs because of the lack of features originating in coherent interactions and because of the difficulty in keeping the cryostat at a constant temperature, combined with the long spectral acquisition time for each array. The transition between these two regimes near 300K is a result of the QW exciton binding energy. The 9 nm well-width wells were chosen for this experiment because of their high PL intensity and their relatively small barrier PL intensity. However, partly because of the large electron-hole separation, and partly because of the quantum confined Stark effect, the QW exciton binding energy should be somewhat less than the 60 meV bulk ZnO exciton binding energy. Therefore, the transition near room temperature is likely a result of reduced exciton-plasmon interaction as the temperature increases above the exciton binding energy.

While the attempts to model these absorbance spectra are ongoing, there are several key points which should be discussed here. Keeping in mind that all of the absorbance spectra presented thus far have been normalized against the transmission through the QW, and given the consistent QW absorbance spectra within several hundred microns of each nanodisc array, the departures from typical LSP dipole and quadrupole absorbance in Figures 51 and 53 can only be understood through the context of strongly coupled systems. The largest deviation from typical LSP absorbance spectra is seen for the array of 91 nm diameter (40 fC dot dose) nanodiscs. Because these nanodiscs demonstrate the largest red-shift in the LSP dipole absorbance, it is extremely unlikely that the phenomena seen in Figures 51 and 53 can be described as strong coupling between the LSP dipole and the QW exciton. Instead, especially given the intensity of the quadrupole absorbance for the 91 nm nanodiscs seen in Figure 49, and given the local enhancement of the quadrupolar electric field intensity seen in the FDTD simulations, it seems very likely that the peaks seen in Figures 51 and 53 result from interactions between the LSP quadrupole and the QW exciton. However, the significant quenching of the quadrupole absorbance in Figures 51 and 53 compared with Figure 52 indicates that this is not simply a result of a Fano resonance between the QW and the LSP quadrupole; such an interaction would result in a Fano peak in the quadrupole absorbance, not attenuation of the LSP quadrupole.

Therefore, since this interaction cannot be the result of interactions between the LSP-dipole and the QW exciton, and it is clearly not the direct result of a Fano resonance between the LSP-quadrupole and the QW exciton, it seems probable that the LSP quadrupole forms a hybridized plasmon-exciton state with the QW exciton. This state

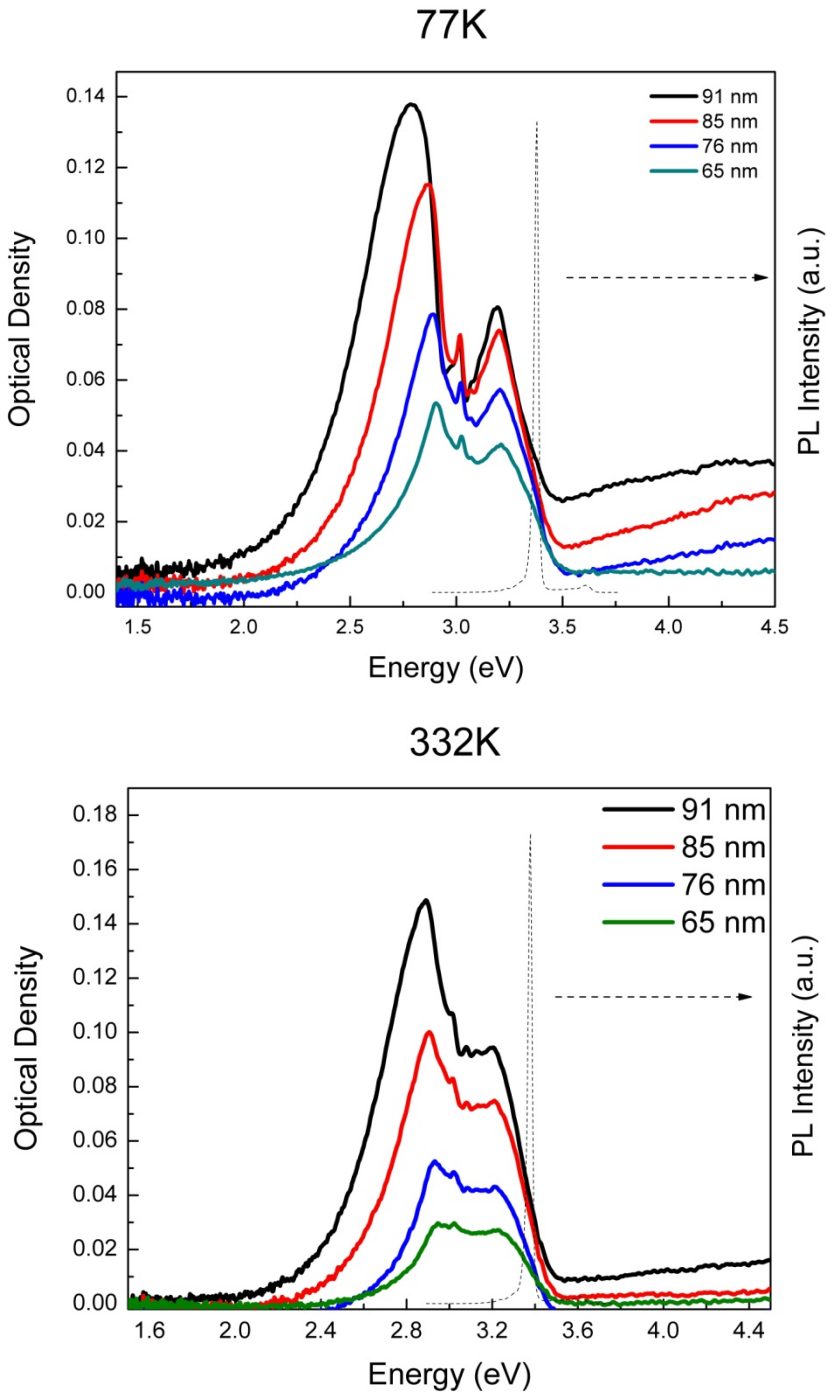

Figure 53: Absorbance spectra for Al nanodisc arrays with dot doses of 25-40 fC (65-91 nm) with 225 nm grating constant deposited on a 9 nm well width QW with a 20 nm top barrier layer, and the QW PL intensity at 15 K. Absorbance spectra acquired at 77K (top) and 332K (bottom)

could then form a Fano resonance with either the ZnO QW exciton or the LSP dipole. Such a system could in principle explain the absorbance spectra seen in Figures 51 and 53. This interaction could be modeled analytically following the theoretical descriptions of hybridized states and Fano resonances in the literature[81, 128, 135-138], but because a second-order interaction of this sort has not yet been reported in the literature, a complete analytical model remains to be constructed.

CHAPTER 6: CONCLUSIONS AND OUTLOOK

Interest in exciton-plasmon coupling is at an all-time high. This dissertation began by using multilayered heterostructures that employed variable thickness MgO spacer-layers as a model system for the analysis of exciton plasmon coupling within the weak coupling regime in ZnO/metal heterostructures. The analysis of the spectrally resolved enhancement as a function of plasmon-exciton separation allowed for the clear identification and differentiation of charge-transfer related enhancement of the band-edge emission, Purcell enhancement of the band edge emission, and enhancement of the impurity 'green PL' by dipole-dipole scattering. The issue of competition between lossy surface waves and Purcell enhancement was clarified by a comparison of the PL enhancement and the exciton lifetime enhancement for heterostructures that employed thin spacer layers. In addition, we presented the first evidence of plasmonic outcoupling in multilayered semiconductor/metal systems with large spacer layers.

The ultrafast results presented in chapter 4 demonstrated the versatility of band-edge degenerate pump probe spectroscopy in conjunction with photoluminescence spectroscopy as a tool for the study of both band-edge and impurity state dynamics. The resonant enhancement of the Zn interstitial defect emission by Ag SPPs allowed for the analysis of the dynamics and energetics of a defect state which had been theoretically predicted but was unreported experimentally. More importantly, it presented dramatic

evidence for Purcell enhancement as a tool for defining the composition of emitters within a broad background.

This dissertation presented the first work studying the enhancement of the ZnO impurity PL by Ag and Au LSPs and by Ag SPPs, and in doing so, it also motivated the pursuit of a variety of research paths regarding plasmon coupling with ZnO defect states. In particular, because the 'green PL' is the result of at least two defect states, band-edge pump probe spectroscopy was insufficient to study the full green PL dynamics. The spectral position of the various impurity PL centers in ZnO are easily accessible by Ag, Au, and Al LSPs of appropriate sizes, and given the dramatic enhancement of the Zn interstitial impurity emission by Ag SPPs, several experiments immediately present themselves:

- The selective PL enhancement of the constituents of the 'green PL' — either the oxygen interstitial emission or the zinc anti-site impurity emission — by resonant LSPs supported on Al, Ag, or Au nanoparticles would emphasize the importance of plasmon-exciton coupling as a technique for extracting the spectral origins of the emitters which compose a broad superposition of states.
- While the selective enhancement of individual impurity emitters would be worthwhile on its own, heterostructures of this type, fabricated with PLD or MBE deposited ZnO, would allow for analysis of strong coupling between ZnO impurity sites and metal LSPs. While the surface roughness of the heterostructures examined in chapters 3 and 4 precluded the coherent energy transfer necessary to enter the strong coupling regime, continued collaborations with the University of Florida or optimized pulsed electron beam deposition techniques would allow for the growth of epitaxial ZnO to facilitate this project.
- In addition, a broadband pump-probe spectroscopy experiment utilizing a band-edge pump and a supercontinuum probe that spanned the visible and near-UV would allow for the simultaneous analysis of the ZnO band-edge dynamics and the dynamics of each defect state in the presence of the designed plasmonic elements.

- A series of pump-probe experiments which utilize two pump beams would also be of significant interest. For example, an experiment which analyzed the Al_2O_3 based heterostructures of chapter 4 with a band-edge pump followed picoseconds later by a pump resonant with the Ag SPP or LSP would allow a supercontinuum or tunable single color probe to analyze the band-edge and impurity dynamics with and without the presence of a pumped plasmonic state.

The presentation of a hybridized quadrupole LSP-exciton state in chapter 5 is unprecedented in the literature, and the Fano resonance created by that state is even more exciting. Though this portion of the dissertation is still relatively undeveloped, the existing work presents a wealth of opportunities for future study:

- While we were unable to demonstrate strong coupling directly between the LSP dipole state and the QW exciton, it is quite possible that Al nanoparticles much smaller than the discs used here could be dropcast onto the QW surface in order to attain a near-UV LSP dipole state with sufficient spectral overlap to allow for a hybridized dipole LSP-exciton state. An investigation into the energetics of the dipole-exciton state in contrast to the quadrupole-exciton state would add significant breadth to the current understanding of the formation of the coupled system.
- Time resolved photoluminescence (TRPL) spectroscopy experiments were ultimately not included in this dissertation because of the difficulty of acquisition of the TRPL spectra. However, if samples with improved optical quality and damage threshold could be prepared, and if the collection efficiency of the TRPL experiment could be improved, time resolved spectra would provide significant additional clarity to the understanding of the quadrupole-exciton or dipole-exciton states.

Finally, the breadth of fundamental physics covered by this dissertation provide for a variety of possible applications. Several projects worth investigating include:

- The fabrication of a ZnO nanowire spaser. Because of the large ZnO gain coefficient, it should in principle be possible to create a metal-coated ZnO nanowire that allows for the amplification of the 1D surface plasmon along the length of the wire.

- Demonstration of electromagnetically induced transparency. The coherent interactions between the ZnO exciton and the LSP dipole or quadrupole states should allow for a designed system which exhibits electromagnetically induced transparency. EIT has otherwise not been reported in ZnO heterostructures. Au and Ag nanodiscs could potentially used in conjunction with ZnO deep impurity states to demonstrate EIT throughout the visible spectrum.
- Theoretical predictions of squeezed photon sources and entangled photon sources produced by excitons coupled strongly to microcavity modes motivate an investigation into metal/ZnO heterostructures as an alternative squeezed photon source. Such a system would require a Rabi splitting energy comparable to the exciton energy, which would prove to be a significant challenge, but by moving out of the strong coupling regime non-adiabatically it should be possible to convert a non-radiative squeezed photon source into a radiative mode. A hybrid system which incorporated a VO_2 layer to move the plasmon off-resonance may be capable of producing just such a transition.

References

1. Beck, F.J., A. Polman, and K.R. Catchpole, *Tunable light trapping for solar cells using localized surface plasmons.* Journal of Applied Physics, 2009. **105**(11): p. -.

2. Morfa, A.J., et al., *Plasmon-enhanced solar energy conversion in organic bulk heterojunction photovoltaics.* Applied Physics Letters, 2008. **92**(1): p. -.

3. Stockman, M.I., *The spaser as a nanoscale quantum generator and ultrafast amplifier.* Journal of Optics, 2010. **12**(2): p. -.

4. Noginov, M.A., et al., *Demonstration of a spaser-based nanolaser.* Nature, 2009. **460**(7259): p. 1110-U68.

5. Ozgur, U., et al., *A comprehensive review of ZnO materials and devices.* Journal of Applied Physics, 2005. **98**(4): p. 103.

6. Pearton, S.J., et al., *Recent progress in processing and properties of ZnO.* Progress in Materials Science, 2005. **50**(3): p. 293-340.

7. Zhang, Y.F., R.E. Russo, and S.S. Mao, *Quantum efficiency of ZnO nanowire nanolasers.* Applied Physics Letters, 2005. **87**(4).

8. Zhou, H., et al., *Ordered, uniform-sized ZnO nanolaser arrays.* Applied Physics Letters, 2007. **91**.

9. Zhang, S.B., S.H. Wei, and A. Zunger, *A phenomenological model for systematization and prediction of doping limits in II-VI and I-III-VI2 compounds.* Journal of Applied Physics, 1998. **83**(6): p. 3192-3196.

10. Kim, K.K., et al., *Realization of p-type ZnO thin films via phosphorus doping and thermal activation of the dopant.* Applied Physics Letters, 2003. **83**(1): p. 63-65.

11. Look, D.C., *Recent advances in ZnO materials and devices.* Materials Science and Engineering: B, 2001. **80**(1-3): p. 383-387.

12. Desgreniers, S., *High-density phases of ZnO: Structural and compressive parameters.* Physical Review B, 1998. **58**(21): p. 14102.

13. Lin, B.X., Z.X. Fu, and Y.B. Jia, *Green luminescent center in undoped zinc oxide films deposited on silicon substrates.* Applied Physics Letters, 2001. **79**(7): p. 943-945.

14. Thonke, K., et al., *Donor-acceptor pair transitions in ZnO substrate material.* Physica B: Condensed Matter, 2001. **308-310**: p. 945-948.

15. Vanheusden, K., et al., *Mechanisms behind green photoluminescence in ZnO phosphor powders.* Journal of Applied Physics, 1996. **79**(10): p. 7983-7990.

16. Bylander, E.G., *Surface effects on the low-energy cathodoluminescence of zinc oxide.* Journal of Applied Physics, 1978. **49**(3): p. 1188-1195.

17. Wang, H.C., et al., *Ultrafast Exciton Dynamics in a ZnO Thin Film.* Japanese Journal of Applied Physics, 2009. **48**(2).

18. Yamamoto, A., et al., *Dynamics of photoexcited carriers in ZnO epitaxial thin films.* Applied Physics Letters, 1999. **75**(4): p. 469-471.

19. Bauer, C., et al., *Ultrafast relaxation dynamics of charge carriers relaxation in ZnO nanocrystalline thin films.* Chemical Physics Letters, 2004. **387**(1-3): p. 176-181.

20. Koida, T., et al., *Correlation between the photoluminescence lifetime and defect density in bulk and epitaxial ZnO.* Applied Physics Letters, 2003. **82**(4): p. 532-534.

21. Teke, A., et al., *Excitonic fine structure and recombination dynamics in single-crystalline ZnO.* Physical Review B, 2004. **70**(19): p. 195207.

22. Chauveau, J.M., et al. *(Zn, Mg)O/ZnO-based heterostructures grown by molecular beam epitaxy on sapphire: Polar vs. non-polar*. 2009: Elsevier Sci Ltd.

23. Chia, C.H., et al., *Confinement-enhanced biexciton binding energy in ZnO/ZnMgO multiple quantum wells.* Applied Physics Letters, 2003. **82**(12): p. 1848-1850.

24. Coli, G. and K.K. Bajaj, *Excitonic transitions in ZnO/MgZnO quantum well heterostructures.* Applied Physics Letters, 2001. **78**(19): p. 2861-2863.

25. Davis, J.A., et al., *Suppression of the internal electric field effects in ZnO/Zn0.7Mg0.3O quantum wells by ion-implantation induced intermixing.* Nanotechnology, 2008. **19**(5): p. 4.

26. Gu, X.Q., et al., *Dependence of photoluminescence of ZnO/Zn0.85Mg0.15O multi-quantum wells on barrier width.* Physics Letters A, 2009. **373**(36): p. 3281-3284.

27. Lusson, A., et al. *Optical study of ZnO/ZnMgO quantum wells grown by metal organic vapor phase epitaxy on ZnO substrates*. 2009: A V S Amer Inst Physics.

28. Yang, W.F., et al., *Pulsed laser deposition of high-quality ZnCdO epilayers and ZnCdO/ZnO single quantum well on sapphire substrate.* Applied Physics Letters, 2010. **97**(6): p. -.

29. Cheng, C.W., et al., *ZnCdO/ZnO Coaxial Multiple Quantum Well Nanowire Heterostructures and Optical Properties.* Journal of Physical Chemistry C, 2010. **114**(9): p. 3863-3868.

30. Buyanova, I.A., et al., *Effects of hydrogen on the optical properties of ZnCdO/ZnO quantum wells grown by molecular beam epitaxy.* Applied Physics Letters, 2008. **92**(26): p. -.

31. Lim, W., et al., *Migration and luminescence enhancement effects of deuterium in ZnO/ZnCdO quantum wells.* Applied Physics Letters, 2008. **92**(3): p. -.

32. Sadofev, S., et al., *Visible-wavelength laser action of ZnCdO/(Zn, Mg)O multiple quantum well structures.* Applied Physics Letters, 2007. **91**(23): p. -.

33. Vegard, L., *Die Konstitution der Mischkristalle und die Raumfüllung der Atome.* Zeitschrift für Physik A Hadrons and Nuclei, 1921. **5**(1): p. 17-26.

34. Denton, A.R. and N.W. Ashcroft, *Vegard's law.* Physical Review A, 1991. **43**(6): p. 3161.

35. Bernard, J.E. and A. Zunger, *Electronic-structure of ZnS, ZnSe, ZnTe, and their pseudobinary alloys.* Physical Review B, 1987. **36**(6): p. 3199-3228.

36. Ohtomo, A., et al., *MgxZn1-xO as a II-VI widegap semiconductor alloy*. Vol. 72. 1998: AIP. 2466-2468.

37. Heitsch, S., et al., *Optical and structural properties of MgZnO/ZnO hetero- and double heterostructures grown by pulsed laser deposition.* Applied Physics a-Materials Science & Processing, 2007. **88**(1): p. 99-104.

38. Cardona, P.Y.Y.a.M., *Fundamentals of Semiconductors: Physics and Materials Properties*. 2001, Berlin: Springer.

39. Park, S.H. and D. Ahn, *Spontaneous and piezoelectric polarization effects in wurtzite ZnO/MgZnO quantum well lasers.* Applied Physics Letters, 2005. **87**.

40. Im, J.S., et al., *Reduction of oscillator strength due to piezoelectric fields in GaN/AlxGa1-xN quantum wells.* Physical Review B, 1998. **57**(16): p. R9435-R9438.

41. Yano, M., et al., *Polarization-induced two-dimensional electron gas at Zn1-xMgxO/ZnO heterointerface.* Journal of Crystal Growth, 2007. **301**: p. 353-357.

42. Zhang, B.P., et al., *Growth of ZnO/MgZnO quantum wells on sapphire substrates and observation of the two-dimensional confinement effect.* Applied Physics Letters, 2005. **86**(3).

43. Morhain, C., et al., *Internal electric field in wurtzite ZnO/Zn0.78Mg0.22O quantum wells.* Physical Review B, 2005. **72**.

44. Davis, J.A., et al., *Observation of coherent biexcitons in ZnO/ZnMgO multiple quantum wells at room temperature.* Applied Physics Letters, 2006. **89**(18): p. 182109-3.

45. Kreller, F., J. Puls, and F. Henneberger, *Temperature-dependent study of optical gain in (Zn,Cd)Se/ZnSe multiple-quantum-well structures.* Applied Physics Letters, 1996. **69**(16): p. 2406-2408.

46. Maier, S.A., *Plasmonics: Fundametals and Applications*. 2007, NY: Springer Science + Business Media.

47. Palik, E.D., *Handbook of optical constants of solids II*. 1991, Boston: Academic Press. xviii, 1096 p.

48. Palik, E.D. and G. Ghosh, *Handbook of optical constants of solids*. 1998, San Diego: Academic Press.

49. Kretschm.E and H. Raether, *Radiative decay of non radiative surface plasmons excited by light.* Zeitschrift Fur Naturforschung Part a-Astrophysik Physik Und Physikalische Chemie, 1968. **A 23**(12): p. 2135.

50. Otto, A., *Excitation of nonradiative surface plasma waves in silver by method of frustrated total reflection.* Zeitschrift Fur Physik, 1968. **216**(4): p. 398.

51. Lee, K.-S. and M.A. El-Sayed, *Gold and Silver Nanoparticles in Sensing and Imaging: Sensitivity of Plasmon Response to Size, Shape, and Metal Composition.* The Journal of Physical Chemistry B, 2006. **110**(39): p. 19220-19225.

52. Link, S., Z.L. Wang, and M.A. El-Sayed, *Alloy Formation of Gold−Silver Nanoparticles and the Dependence of the Plasmon Absorption on Their Composition.* The Journal of Physical Chemistry B, 1999. **103**(18): p. 3529-3533.

53. Bohren, C.F.a.H., D.R. , *Absorption and Scattering of light by small particles*. 1983, New York, NY: John Wiley & Sons, Inc.

54. Kreibig, U.a.V., M., *Optical Properties of Metal Clusters*. 1995, Berline: Springer.

55. Chan, G.H., et al., *Localized surface plasmon resonance spectroscopy of triangular aluminum nanoparticles.* Journal of Physical Chemistry C, 2008. **112**(36): p. 13958-13963.

56. Achermann, M., *Exciton−Plasmon Interactions in Metal−Semiconductor Nanostructures.* The Journal of Physical Chemistry Letters, 2010. **1**(19): p. 2837-2843.

57. Lin, H.Y., et al., *Enhancement of band gap emission stimulated by defect loss.* Optics Express, 2006. **14**(6): p. 2372-2379.

58. Lee, M.K., et al., *Surface plasmon resonance (SPR) electron and energy transfer in noble metal-zinc oxide composite nanocrystals.* Journal of Physical Chemistry C, 2008. **112**(27): p. 10079-10082.

59. Zhang, W.Q., et al., *Controlled Synthesis and Biocompatibility of Water-Soluble ZnO Nanorods/Au Nanocomposites with Tunable UV and Visible Emission Intensity.* Journal of Physical Chemistry C, 2008. **112**(50): p. 19872-19877.

60. Wood, A., M. Giersig, and P. Mulvaney, *Fermi level equilibration in quantum dot-metal nanojunctions.* Journal of Physical Chemistry B, 2001. **105**(37): p. 8810-8815.

61. Subramanian, V., E.E. Wolf, and P.V. Kamat, *Green emission to probe photoinduced charging events in ZnO-Au nanoparticles. Charge distribution and fermi-level equilibration.* Journal of Physical Chemistry B, 2003. **107**(30): p. 7479-7485.

62. Bai, X.D., et al., *Measuring the work function at a nanobelt tip and at a nanoparticle surface.* Nano Letters, 2003. **3**(8): p. 1147-1150.

63. Purcell, E.M., *Spontaneous Emission Probabilities at Radio Frequencies.* Physical Review, 1946. **69**(11-12).

64. Kleppner, D., *Inhibited Spontaneous Emission.* Physical Review Letters, 1981. **47**(4): p. 233-236.

65. Ford, G.W. and W.H. Weber, *Electromagnetic-interactions of molecules with metal-surfaces.* Physics Reports-Review Section of Physics Letters, 1984. **113**(4): p. 195-287.

66. Worthing, P.T., R.M. Amos, and W.L. Barnes, *Modification of the spontaneous emission rate of Eu^{3+} ions embedded within a dielectric layer above a silver mirror.* Physical Review A, 1999. **59**(1): p. 865.

67. Gontijo, I., et al., *Coupling of InGaN quantum-well photoluminescence to silver surface plasmons.* Physical Review B, 1999. **60**(16): p. 11564-11567.

68. Neogi, A., et al., *Enhancement of spontaneous recombination rate in a quantum well by resonant surface plasmon coupling.* Physical Review B, 2002. **66**(15): p. -.

69. Lai, C.W., J. An, and H.C. Ong, *Surface-plasmon-mediated emission from metal-capped ZnO thin films.* Applied Physics Letters, 2005. **86**(25).

70. Li, J. and H.C. Ong, *Temperature dependence of surface plasmon mediated emission from metal-capped ZnO films.* Applied Physics Letters, 2008. **92**(12).

71. Cheng, P.H., D.S. Li, and D. Yang, *Influence of substrates in ZnO devices on the surface plasmon enhanced light emission.* Optics Express, 2008. **16**(12): p. 8896-8901.

72. Khurgin, J.B. and G. Sun, *Enhancement of optical properties of nanoscaled objects by metal nanoparticles.* Journal of the Optical Society of America B-Optical Physics, 2009. **26**(12): p. B83-B95.

73. Ferry, V.E., J.N. Munday, and H.A. Atwater, *Design Considerations for Plasmonic Photovoltaics.* Advanced Materials, 2010. **22**(43): p. 4794-4808.

74. Pillai, S., et al., *Surface plasmon enhanced silicon solar cells.* Journal of Applied Physics, 2007. **101**(9): p. -.

75. Ferry, V.E., et al., *Light trapping in ultrathin plasmonic solar cells.* Optics Express, 2010. **18**(13): p. A237-A245.

76. Westphalen, M., et al., *Metal cluster enhanced organic solar cells.* Solar Energy Materials and Solar Cells, 2000. **61**(1): p. 97-105.

77. Catchpole, K.R. and A. Polman, *Design principles for particle plasmon enhanced solar cells.* Applied Physics Letters, 2008. **93**(19): p. -.

78. Yablonovitch, E. and G.D. Cody, *Intensity Enhancement in Textured Optical Sheets for Solar-Cells.* Ieee Transactions on Electron Devices, 1982. **29**(2): p. 300-305.

79. Catchpole, K.R. and S. Pillai, *Surface plasmons for enhanced silicon light-emitting diodes and solar cells.* Journal of Luminescence, 2006. **121**(2): p. 315-318.

80. Catchpole, K.R. and A. Polman, *Plasmonic solar cells.* Optics Express, 2008. **16**(26): p. 21793-21800.

81. Fofang, N.T., et al., *Plexcitonic Nanoparticles: Plasmon-Exciton Coupling in Nanoshell-J-Aggregate Complexes.* Nano Letters, 2008. **8**(10): p. 3481-3487.

82. Kaliteevski, M., et al., *Hybrid states of Tamm plasmons and exciton polaritons.* Applied Physics Letters, 2009. **95**(25): p. 3.

83. Bellessa, J., et al., *Giant Rabi splitting between localized mixed plasmon-exciton states in a two-dimensional array of nanosize metallic disks in an organic semiconductor.* Physical Review B, 2009. **80**(3).

84. Symonds, C., et al., *Particularities of surface plasmon-exciton strong coupling with large Rabi splitting.* New Journal of Physics, 2008. **10**.

85. Haroche, S. and J.M. Raimond, *Radiative Properties of Rydberg States in Resonant Cavities.* Advances in Atomic and Molecular Physics, 1985. **20**: p. 347-411.

86. Rempe, G., H. Walther, and N. Klein, *Observation of quantum collapse and revival in a one-atom maser.* Physical Review Letters, 1987. **58**(4): p. 353.

87. Khitrova, G., et al., *Vacuum Rabi splitting in semiconductors.* Nature Physics, 2006. **2**(2): p. 81-90.

88. Andreani, L.C., G. Panzarini, and J.M. Gerard, *Strong-coupling regime for quantum boxes in pillar microcavities: Theory.* Physical Review B, 1999. **60**(19): p. 13276-13279.

89. Hideo Iwase, D.E., Jelena Vuckovic, *Analysis of the Purcell effect in photonic and plasmonic crystals with losses.* Optics Express, 2010. **18**(16): p. 16546-16560.

90. Bellessa, J., et al., *Giant Rabi splitting in metal/semiconductor nanohybrids.* Superlattices and Microstructures, 2011. **49**(3): p. 209-216.

91. Miroshnichenko, A.E., S. Flach, and Y.S. Kivshar, *Fano resonances in nanoscale structures.* Reviews of Modern Physics, 2010. **82**(3): p. 2257.

92. Zhang, W., A.O. Govorov, and G.W. Bryant, *Semiconductor-metal nanoparticle molecules: Hybrid excitons and the nonlinear Fano effect.* Physical Review Letters, 2006. **97**(14).

93. [cited 2010 January 28]; Available from: http://www.thermionics.com/Legacy/Handling/pld-typical.aspx.

94. Chrisey, D.B. and G.K. Hubler, *Pulsed laser deposition of thin films*. 1994, New York: J. Wiley. xxviii, 613 p.

95. Ohtomo, A., et al., *Single crystalline ZnO films grown on lattice-matched ScAlMgO4(0001) substrates.* Applied Physics Letters, 1999. **75**(17): p. 2635-2637.

96. Tamura, K., et al., *Epitaxial growth of ZnO films on lattice-matched ScAlMgO4(0001) substrates.* Journal of Crystal Growth, 2000. **214**: p. 59-62.

97. Srikant, V. and D.R. Clarke, *Optical absorption edge of ZnO thin films: The effect of substrate.* Journal of Applied Physics, 1997. **81**(9): p. 6357-6364.

98. Smith, T.P., et al., *Growth and characterization of ZnO thin films on GaN epilayers.* Journal of Electronic Materials, 2004. **33**(7): p. 826-832.

99. Fu, Z.X., et al., *The effect of Zn buffer layer on growth and luminescence of ZnO films deposited on Si substrates.* Journal of Crystal Growth, 1998. **193**(3): p. 316-321.

100. Studenikin, S.A. and M. Cocivera, *Time-resolved luminescence and photoconductivity of polycrystalline ZnO films.* Journal of Applied Physics, 2002. **91**(8): p. 5060-5065.

101. Ferrara, D.W., *Plasmonic interactions in gold::vanadium dioxide hybrid nanostructures*, in *Physics*. 2011, Vanderbilt University.

102. Ensley, T.R., et al., *Energy and spectral enhancement of femtosecond supercontinuum in a noble gas using a weak seed.* Opt. Express, 2011. **19**(2): p. 757-763.

103. *Operator's Manual: The Coherent Mira Model 900 Laser*, C. Inc., Editor. 1996: Santa Clara, CA.

104. Strickland, D. and G. Mourou, *Compression of amplified chirped optical pulses.* Optics Communications, 1985. **56**(3): p. 219-221.

105. *TOPAS-800*. 05/08/2011]; Available from: www.lightcon.com/products/product.php?ID=162.

106. *Titan Femtosecond/Picosecond Pulse Regenerative+Multipass Ti:sapphire Amplifier User's Manual*, Quantronix, Editor: East Setauket, NY.

107. Alfano, R.R. and S.L. Shapiro, *EMISSION IN REGION 4000 TO 7000 A VIA 4-PHOTON COUPLING IN GLASS.* Physical Review Letters, 1970. **24**(11): p. 584-&.

108. Brodeur, A. and S.L. Chin, *Ultrafast white-light continuum generation and self-focusing in transparent condensed media.* Journal of the Optical Society of America B-Optical Physics, 1999. **16**(4): p. 637-650.

109. Corkum, P.B., et al., *GENERATION OF INFRARED SUPERCONTINUUM COVERING 3-14 MU-M IN DIELECTRICS AND SEMICONDUCTORS.* Optics Letters, 1985. **10**(12): p. 624-626.

110. Smith, W.L., P. Liu, and N. Bloembergen, *SUPERBROADENING IN H2O AND D2O BY SELF-FOCUSED PICOSECOND PULSES FROM A YALG=ND LASER.* Physical Review A, 1977. **15**(6): p. 2396-2403.

111. Glownia, J.H., J. Misewich, and P.P. Sorokin, *ULTRAFAST ULTRAVIOLET PUMP PROBE APPARATUS.* Journal of the Optical Society of America B-Optical Physics, 1986. **3**(11): p. 1573-1579.

112. Johnson, P.J.M., V.I. Prokhorenko, and R.J.D. Miller, *Stable UV to IR supercontinuum generation in calcium fluoride with conserved circular polarization states.* Optics Express, 2009. **17**(24): p. 21488-21496.

113. Lawrie, B.J., R. Mu, and R.F. Haglund. *Coupling dynamics between photoluminescent centers in ZnO and surface plasmons*. 2009. San Diego, CA, USA: SPIE.

114. Haglund, R.F., B.J. Lawrie, and R. Mu, *Coupling of photoluminescent centers in ZnO to localized and propagating surface plasmons.* Thin Solid Films, 2010. **518**(16): p. 4637-4643.

115. Lawrie, B.J., R.F. Haglund, and R. Mu, *Enhancement of ZnO photoluminescence by localized and propagating surface plasmons.* Optics Express, 2009. **17**(4): p. 2565-2572.

116. Lawrie, B.J., R. Mu, and R.F. Haglund, *Substrate dependence of Purcell enhancement in ZnO-Ag multilayers.* physica status solidi (c), 2011. **8**(1): p. 159-162.

117. Wang, Y., et al., *Effect of MgO in ZnO films grown on nitrided sapphires.* Journal of Crystal Growth, 2007. **305**(1): p. 74-77.

118. Jackson, J.D., *Classical Electrodynamics*. 3rd ed. 1999: Wiley.

119. Chang, Y.M., *Coherent phonon spectroscopy of GaP Schottky diode.* Applied Physics Letters, 2003. **82**(11): p. 1781-1783.

120. Chachisvilis, M., H. Fidder, and V. Sundström, *Electronic coherence in pseudo two-colour pump-probe spectroscopy.* Chemical Physics Letters, 1995. **234**(1-3): p. 141-150.

121. Engh, R.A., J.W. Petrich, and G.R. Fleming, *Removal of coherent coupling artifact in ground-state recovery experiments: malachite green in water-methanol mixtures.* The Journal of Physical Chemistry, 1985. **89**(4): p. 618-621.

122. Wang, Y.K., et al., *Radiative Rate Enhancements in Ensembles of Hybrid Metal-Semiconductor Nanostructures.* Physical Review Letters, 2009. **102**(16).

123. Barnes, W.L., *Fluorescence near interfaces: the role of photonic mode density.* Journal of Modern Optics, 1998. **45**(4): p. 661-699.

124. Li, Y.F., et al., *Valence-band offset of epitaxial ZnO/MgO (111) heterojunction determined by x-ray photoelectron spectroscopy.* Applied Physics Letters, 2008. **92**(19): p. 192116-3.

125. Schleife, A., et al., *Branch-point energies and band discontinuities of III-nitrides and III-/II-oxides from quasiparticle band-structure calculations.* Applied Physics Letters, 2009. **94**(1): p. 012104-3.

126. Janotti, A. and C.G. Van de Walle, *Absolute deformation potentials and band alignment of wurtzite ZnO, MgO, and CdO.* Physical Review B, 2007. **75**(12): p. 121201.

127. Zeng, H.B., et al., *Blue Luminescence of ZnO Nanoparticles Based on Non-Equilibrium Processes: Defect Origins and Emission Controls.* Advanced Functional Materials, 2010. **20**(4): p. 561-572.

128. Fofang, N.T., et al., *Plexciton Dynamics: Exciton−Plasmon Coupling in a J-Aggregate−Au Nanoshell Complex Provides a Mechanism for Nonlinearity.* Nano Letters, 2011. **11**(4): p. 1556-1560.

129. Ciuti, C., et al., *Quantum vacuum properties of the intersubband cavity polariton field.* Physical Review B, 2005. **72**(11): p. 115303.

130. Ohtomo, A., et al., *$Mg_xZn_{1-x}O$ as a II-VI widegap semiconductor alloy. Appl. Phys. Lett.* 1998. **72**(19): p. 2466.

131. Kratschmer, E., *Verification of a proximity effect correction program in electron-beam lithography.* Journal of Vacuum Science & Technology, 1981. **19**(4): p. 1264-1268.

132. Ingino, J., et al., *Workpiece charging in electron beam lithography.* Journal of Vacuum Science & Technology B: Microelectronics and Nanometer Structures, 1994. **12**(3): p. 1367-1371.

133. Schmidt, R., et al., *Dielectric functions (1 to 5 eV) of wurtzite MgxZn1-xO (x <= 0.29) thin films.* Applied Physics Letters, 2003. **82**(14): p. 2260-2262.

134. Langhammer, C., et al., *Localized Surface Plasmon Resonances in Aluminum Nanodisks.* Nano Letters, 2008. **8**(5): p. 1461-1471.

135. Manjavacas, A., F.J.G.a.d. Abajo, and P. Nordlander, *Quantum Plexcitonics: Strongly Interacting Plasmons and Excitons.* Nano Letters, 2011. **11**(6): p. 2318-2323.

136. Ming, T., et al., *Experimental Evidence of Plasmophores: Plasmon-Directed Polarized Emission from Gold Nanorod–Fluorophore Hybrid Nanostructures.* Nano Letters, 2011. **11**(6): p. 2296-2303.

137. Gallinet, B.a.M., O.J.F. (2011) *Ab initio theory of Fano resonances in plasmonic nanostructures and metamaterials*. ArXiv e-prints **1105.2503**.

138. Artuso, R.D. and G.W. Bryantt, *Optical response of strongly coupled quantum dot - Metal nanoparticle systems: Double peaked fano structure and bistability.* Nano Letters, 2008. **8**(7): p. 2106-2111.